Interactions of Two-Dimensionally Confined Electrons with an Adjacent Magnetic Monopole

Johnathan Martin

Supervised by Jorge Quintanilla and Sam Carr

Division of Natural Sciences: School of Physics and Astronomy, Physics of Quantum Materials Group

This dissertation is submitted for the degree of Doctor of Philosophy

March 2025

Declaration

I declare that the content of this thesis, titled “Interactions of Two-Dimensionally Confined Electrons with an Adjacent Magnetic Monopole” is entirely my own, and has not been submitted for the purposes of a qualification at any other institution or for any other degree. All data is my own, unless explicitly stated otherwise. All instances where use has been made of other work have been cited.

The work comprising chapters 2 to 8 has been adapted and extended from the paper "Classically Bound and Quantum Quasi-Bound States of an Electron on a Plane Adjacent to a Magnetic Monopole" authored by: J. Martin, A. Baskerville, V.L. Campo, J. Minns, J. Pooley, S. Carr, C. Hooley, G. Moller and J. Quintanilla.

Johnathan Martin

March 2025

Acknowledgments

Starting a PhD is at the best of times a mixture of feeling excited, trepidatious, overwhelmed, and everything in between. These feelings were magnified when starting out on this journey, as the Covid-19 pandemic was in full swing. Nevertheless, I made it to the finish line! I would like to express my deepest gratitude to the individuals who supported and guided me throughout this journey.

Firstly I would like to thank my supervisors Dr Jorge Quintanilla and Dr Sam Carr for there support and expertise in guiding me through my PhD. From the initial stages to the final submission of this thesis, their continued encouragement and excitement for the projects that we have worked on together has been amazing.

I would like to thank my parents, John and Lynda Martin, and also my parents in law, Trevor and Susan Cornish, for their continued support whilst completing this PhD.

Finally I would like to thank my fellow PhDs with whom I share an office: T. Hewitt, J. Chapman, J. Tucker, A. Overton, C. Skingle, T. Watts, E. Chipperfield for the constructive and the not so constructive conversation.

Well that's everyone I can think of to acknowledge...I can't think of another person that would have supported me...but it does feel as though someone is missing!...What is with this feeling of existential dread creeping over me?...Oh well on with the thesis...

A Very Special Acknowledgement

I would like to give a very special thank you to my wife Tamsin. Without your continued support, patience and love I would never have been able to complete this journey. Your encouragement to take the first steps onto an undergraduate physics course is what has led me to where I am today, I can honestly say that I would never have accomplished this by myself.

So, thank you: my beautiful, intelligent, creative, supportive, patient, caring, and ever loving wife, Tamsin.

Abstract

An electron in the presence of a magnetic monopole cannot form a bound state to the monopole in three dimensions. All states formed are scattering and follow a geodesic trajectory on the surface of a cone. In this thesis I show that confining the electron to two dimensions and placing the monopole above or below said plane allows for bound states to be formed. Classically, utilising Lagrangian mechanics, these are fully bound never forming scattering states without an influx of energy. Quantum mechanically (Solutions to Schrödinger time independent equation) and semi-classically (Bohr-Sommerfeld quantisation, WKB approximation), these states are quasi-bound with finite lifetimes before turning into a scattering state. The minimum charge that can bind an electron to a magnetic monopole is approximately the same strength as 16 Dirac monopoles. The lifetimes of these scattering states is dependent on the electron's energy eigenvalue, the strength of the magnetic monopole, and the distance the monopole is from the plane.

Magnetic monopoles can be detected using a SQUID (Superconducting QUantum Interference Device) measuring the quantised jumps in magnetic flux. In this thesis I ask: can they be detected using the Hall effect? With the electrons bound to a plane permeated by the non-uniform magnetic field produced by a magnetic monopole; what will the Hall voltage look like across the plane, and can it be measured? Magnetohydrodynamics is utilised to model the flow of an electron gas by treating it as a fluid that interacts with both magnetic and electrical fields. A single Dirac monopole produces a peak in Hall voltage across the modelled Hall sensor of the order 10^{-6}V. For a monopole found in spin-ice, which is about $1/8000$ the magnetic charge of a single Dirac monopole, this voltage is considerably less.

Contents

Chapter 1

Introduction

This thesis looks at the interactions of magnetic monopoles and electrons over two different projects. The first focuses on finding bound states of an electron about a magnetic monopole with the electron confined to two dimensions. This is explored in classical, semi-classical, and quantum mechanical regimes. The second project concerns the detection of magnetic monopoles using the Hall effect: using magnetohydrodynamics to evaluate the flow of an electron gas. This is currently an area under investigation with measurements being performed by a SQUID [1].

In Chapter 2, I introduce the problem of binding a two dimensionally confined electron to a magnetic monopole through graphical representation of the problem. The problem is rescaled to make it dimensionless. These definitions are presented in this chapter. Moving to Chapter 3 We look at the methods used in this thesis: Lagrangian Mechanics, Bohr-Sommerfeld quantisation, WKB approximation, the finite difference method, and fourth order Runge-Kutta. Chapter 4 shows the classical solutions to the problem of binding an electron to a monopole: introducing a classical potential, find-

ing the orbital trajectory of the electrons, and what defines the type of orbit. In Chapter 5, we take a look at a semi-classical approach to the problem using the classical potential derived previously. Using a simple harmonic oscillator; an estimation of the bound states is acquired. The system is very reminiscent of electrons orbiting about a hydrogen nucleus that was evaluated using the Bohr-Sommerfeld quantisation, and so it works very well here. In Chapter 6, the problem is cast in a quantum mechanical framework where the difference between the classical and quantum potentials is highlighted and the problem is transformed into a one dimensional Schrödinger equation. A WKB approximation and finite difference method are both utilised to solve the Schrödinger equation where quasi-bound states are found. Chapter 7 looks at the lifetimes of the quasi-bound states: a WKB approximation and finite difference methods are once again used to find the half lives of these states, an additional phase shift method also found lifetimes and the energies of the quasi-bound states. In Chapter 8, I bring the first of the projects to a close with the revelation of the results of the previous chapters: comparing and contrasting between the different methods, drawing conclusions, and finding out if it is possible to create a magnetic monopole strong enough to bind an electron constrained to two dimensions.

Chapter 9 marks the beginning of a new project on a similar theme. While previously I looked at the bound electrons, attention now turns to unbound electrons. The problem of modelling 2D electron flows in a magnetic monopole field and measuring the Hall voltage produced is explored. An introduction to magnetohydrodynamics and the Hall effect are presented for background knowledge. The equations of motion are derived for uniform and non-uniform magnetic fields as well as the Hall voltage in magnetohydrodynamic framework. Finally, the equations of motion are transformed into non-dimensional equations to investigate their behaviour. In Chapter

10, the finite difference method in two dimensions is used to simulate the electron gas flow on the Hall sensor: measuring the mass density of electrons, x and y velocities, and the Hall voltage over the sensor plane. This is done for both uniform magnetic fields and also for the magnetic fields of monopoles in various configurations. Lastly, I apply the model to 2D materials and see what type of results could be expected experimentally. Chapter 11 is a discussion and conclusion section for the results seen previously, and I answer the question that this project initially set.

For the remainder of this chapter I will cover the key concepts needed for the reader: what is a magnetic monopole and where are they? Can an electron orbit a magnetic monopole in three dimensions? Finally an Introduction to magnetohydrodynamics and the Hall voltage.

1.1 What is a Magnetic Monopole and Where are They?

In 1931 Paul Dirac imagined a magnetic monopole as a defect by constructing a vector potential that led to a monopolar field everywhere in space, but which was singular on a single line; an infinitely thin undetectable solenoid, commonly referred to as a Dirac string [2]. An electron in the presence of a Dirac monopole would not be able to see the Dirac string. These Dirac monopoles have yet to be found, if they can be found at all; with their existence being a matter of speculation. The Dirac monopole charge is given as

$$Q_D = \frac{2\pi\hbar}{\mu_0 q_e} n, \tag{1.1}$$

where $\mu_0 \approx 1.26 \times 10^{-6}$ is the permeability of free space, $\hbar$ is Planck's reduced constant and q_e is the electrical charge of an electron and n is an integer

value. Placing these values into the equation, with $n = 1$ for the smallest Dirac monopole charge we get $Q_D \approx 3.29 \times 10^{-9}$Am. This led to Dirac stating "that a single magnetic monopole in the Universe would explain the electric charge quantisation" [3].

No Dirac monopoles have been found thus far [4,5] there are several possible hypotheses: magnetic monopoles never existed, used to exist, and exist but are extremely rare. Comparing the forces between two oppositely electrically charged particles (q_{e1} and q_{e2}), $q_{e1} = -q_{e2}$, and oppositely magnetically charged particles (Q_{D1} and Q_{D2}), $Q_{D1} = -Q_{D2}$ using Coulomb's Law and an equivalent for magnetic monopoles we get force equations for static particles as

$$F_e = \frac{q_{e1}q_{e2}}{4\pi\epsilon_0 r^2}\mathbf{r}_{1\to 2}, \qquad (1.2) \qquad F_M = \frac{\mu_0 Q_{D1}Q_{D2}}{4\pi r^2}\mathbf{r}_{1\to 2}, \qquad (1.3)$$

where F_e is the force between electrically charged particles, F_M is the force between magnetically charged particles, and $\epsilon_0 \approx 8.85 \times 10^{12}\text{Fm}^{-1}$ is the permittivity of free space. Placing values into these equations using the single Dirac charge calculated earlier, $q_{e1} \approx 1.602 \times 10^{-19}$C and $r = 1$m we get $F_e = 2.31 \times 10^{-28}$N and $F_M = 1.08 \times 10^{-24}$N which is in agreement with the calculations of [6]. The force between a pair of oppositely charged monopoles is four orders of magnitude greater than that of an electron-positron pair so this would certainly provide an appropriate mechanism for the greater annihilation of magnetic monopole pairs compared to electrically charged particles at the birth of the universe; should magnetic monopoles have ever existed at all.

With our current lack of magnetic monopoles we can turn our attention to monopole-like sources, with behaviour similar to that of a magnetic

monopole but which are not true Dirac monopoles. These monopole-like sources have not got quantised magnetic charge; with the string between the two poles being visible to electrons. Close to the singular poles the electron behaves as if it were a magnetic monopole but the field lines are not radial and do converge on the other pole. Three sources for these are:

- Spin-ice materials: constructed of frustrated magnetic moments creating a magnetic monopole on a lattice site and the opposite polarity magnetic monopole on an adjacent site. These form a superparamagnetic regime, see Fig. 1.1. As the spins on each site flip, the monopoles can be moved away from one another or be recombined so no overall magnetic field is present [7,8].

- Artificial spin-ice: these are constructed using nano scale dipole magnets arranged on a lattice, with one pole sitting on the lattice site and the other on the neighbouring lattice site. Flipping a magnet will produce an overall magnetic charge on one lattice site and an opposing magnetic charge on a neighbouring site. At each of these lattice sites it now appears that a magnetic monopole is present, see Fig. 1.2. As with spin-ice, if we flip magnets adjacent to these sites we can move the monopoles away from one another [9–11].

- Magnetic needle: the latest (and also earliest method, as Birkelands monopole was a less refined version of this experiment) way to create an artificial monopole is via a nano scale ferromagnetic needle, focusing our attention to the tip at one end we can produce a magnetic field that is very similar to a monopole [12].

I will return to these different types of monopole analogues in the discussion section where I will examine what would be required to produce a bound

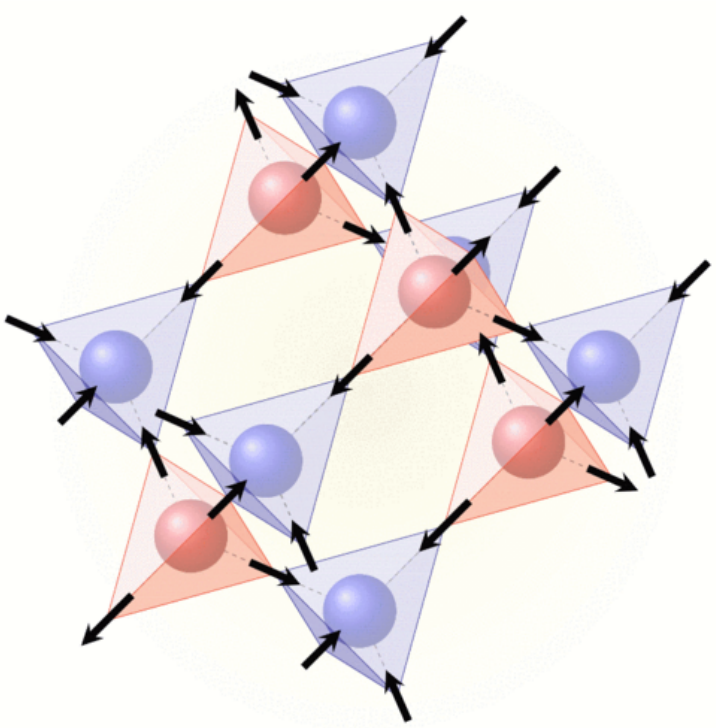

Figure 1.1: The magnetic moments on a tetrahedral lattice magnetically frustrated so as to form an overall magnetic charge on a site. The magnetic charges always come in pairs of opposing polarity but located on different sites, these lattice sites do not have to be next to one another. The string formed between the two monopoles can be seen by an electron so these are not Dirac monopoles, their value of charge depends on the magnitude and the orientation of the magnetic moments at the lattice site. Figure referenced from [13].

state in all three cases.

1.2 Can an Electron Orbit a Magnetic Monopole?

An electron with a velocity of $\mathbf{v} = (v_x, v_y, v_z)$ and an electric charge q_e in a uniform magnetic field, $\mathbf{B} = (B_x, B_y, B_z)$ will feel a force, $\mathbf{F}$, acting upon it in accordance with the Lorentz force

$$\mathbf{F} = q_e(\mathbf{v} \times \mathbf{B}) = q_e \left[\left(v_y B_z - v_z B_y\right) \hat{\mathbf{i}} + \left(v_z B_x - v_x B_z\right) \hat{\mathbf{j}} + \left(v_x B_y - v_y B_x\right) \hat{\mathbf{k}} \right]. \tag{1.4}$$

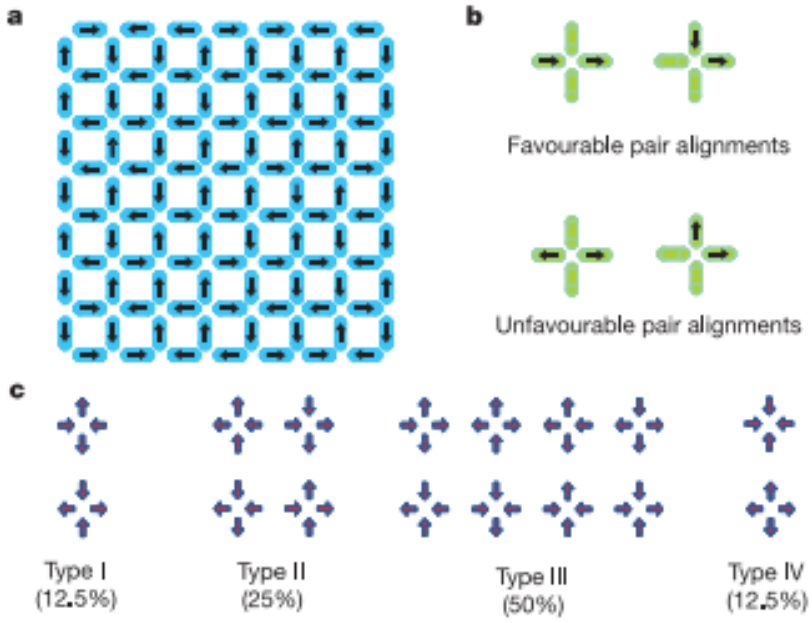

Figure 1.2: Magnetic dipoles arranged on a square array at the point where 4 magnets meet the total charge can take one of several configurations. An imbalance of poles at an intersection will cause an overall magnetic charge to form there. The size of this charge is dependent on the strength of the dipoles, the number of like poles meeting at the intersection and the geometry of the intersection itself with some geometry leading to a permanently frustrated state. Figure referenced form [11].

Figure 1.3: Birkeland's experiment with a cathode ray tube on the right and on the left the pole of a magnet. The cathode rays shown in the tube follow the lines of magnetic field which when only influenced by a single pole of a magnet appear similar to what one would expect from a magnetic monopole. Image taken from [14].

We see that the force is always perpendicular to the velocity and the magnetic field. When the electron is restricted to a plane, $v_z = 0$, the only part of the magnetic field that will affect its motion is B_z. The Lorentz force in this scenario becomes

$$\mathbf{F} = q_e \left[\left(v_y B_z \right) \hat{\mathbf{i}} - \left(v_x B_z \right) \hat{\mathbf{j}} \right], \tag{1.5}$$

causing the electron to take a curved path on the plane.

Birkeland observed that if the pole of an electromagnet is placed at the opposing end of a cathode, the trajectory of the cathode rays (a stream of electrons in) converged on the magnetic pole see Fig. 1.3.

In 1896 Henry Poincaré [15] considered the interaction of cathode rays with a magnet based on the experiments conducted by Kristian Birkeland. Poincaré later noted that motion of the electrons in the cathode tube behaved as if a magnetic monopole were present. Modelling a magnetic field, **B**, so that its

source was point-like

$$\mathbf{B} = \frac{\alpha}{r^3}\mathbf{r}, \tag{1.6}$$

where $\mathbf{r} = (x(t), y(t), z(t))$, $r^2 = x^2 + y^2 + z^2$ and α is a constant. Using the Lorentz force law for a charged particle in a magnetic field

$$\frac{d^2\mathbf{r}}{dt^2} = q_e(\frac{d\mathbf{r}}{dt} \times \mathbf{B}) = \frac{\beta}{r^3}(\frac{d\mathbf{r}}{dt} \times \mathbf{r}), \tag{1.7}$$

β has now absorbed all of the constants into a single value and $q_e = -1.602 \times 10^{-19}$C is the charge of an electron. Poincaré calculated the equations of motion for an electron about a point source magnetic field, these equations of motion can be written as

$$\ddot{\mathbf{r}} = \frac{\beta}{r^3}\mathbf{r} \times \dot{\mathbf{r}}, \tag{1.8}$$

showing that the acceleration of the electron is perpendicular to the position vector $\mathbf{r}$ and the velocity of the electron $\dot{\mathbf{r}}$. The energy of the electron is constant as no work is done by the magnetic field. This gives the relationship

$$|\dot{\mathbf{r}}|^2 = C. \tag{1.9}$$

C is a constant that is equal to $2E/m$, where E is the kinetic energy of the electron and m is the electron mass. Taking the derivative of r^2 with respect to time

$$\frac{d}{dt}r^2 = 2\dot{\mathbf{r}}\mathbf{r}. \tag{1.10}$$

Next taking the second derivative of r^2 with respect to time

$$\frac{d^2}{dt^2}r^2 = 2\,|\dot{\mathbf{r}}|^2 = 2C. \tag{1.11}$$

Performing two successive integrations with respect to time gives

$$r^2 = Ct^2 + Bt + A, \tag{1.12}$$

where A and B are constants of integration. Taking the cross product of $\mathbf{r}$ with the Lorentz force equation , Eq. (1.7), then integrating with respect to t

$$\mathbf{r} \times \dot{\mathbf{r}} = -\frac{\beta}{r}\mathbf{r} + \mathbf{D}, \tag{1.13}$$

where $\mathbf{D} = (a, b, c)$ is a constant vector from the integration. The angular momentum of the electron is not conserved but D is. The constant D is the total angular momentum of the system and $-\frac{\beta}{r}\mathbf{r}$ is the angular momentum of the magnetic field, rearranging we get

$$\mathbf{D} = \mathbf{r} \times \dot{\mathbf{r}} + \frac{\beta}{r}\mathbf{r}, \tag{1.14}$$

showing that the total angular momentum of the system is comprised of the angular momentum of the electron and of the magnetic field. Since the total angular momentum is constant it is then conserved at all points, which means that the angular momentum is conserved between the magnetic field and the monopole as a system. Taking the dot product of $\mathbf{D}$ with $\mathbf{r}$

$$\mathbf{r} \cdot \mathbf{D} = \mathbf{r} \cdot (\mathbf{r} \times \dot{\mathbf{r}}) + \frac{\beta}{r}\mathbf{r} \cdot \mathbf{r} = \beta r, \tag{1.15}$$

and

$$\mathbf{r} \cdot \mathbf{D} = ax + by + cz. \tag{1.16}$$

Setting Eq. (1.15) equal to Eq. (1.16) gives

$$ax + by + cz = \beta r. \tag{1.17}$$

The angle between the total angular momentum **D** and the position vector **r** is constant value. The only way that this angle can remain constant is if the position vector **r** sits on the surface of a cone with the total angular momentum vector **D** forming an axis about which the cone can rotate symmetrically. From Eq. (1.8) we see that the acceleration is perpendicular to the velocity and position vector of the electron so must be pointing normally from the surface of the cone inwards. Since the electron does not leave the surface of the cone that is generated by revolving the vector **r** about **D** then it must take the shortest path between two points which will be a geodesic on the surface of the cone (unfolding the cone would reveal that this path is in fact straight) [14–16], see Fig. 1.4. As such no electron can form a bound orbit about a monopole in three dimensions as the geodesic trajectory on a cone will always scatter the electron.

When the electron is restricted to a plane, as is done in the quantum Hall effect (neglecting edge hopping states), the orbits are all circular. In two dimensions for a uniform magnetic field all classical states are bound this remains true when quantised [18]. For a uniform magnetic field one would expect circular orbits. However would this also hold true for the non uniform magnetic field of a magnetic monopole if the electron was confined to a plane? Would suspending a magnetic monopole beneath or above the plane result in all orbits being circular in a classical regime? Quantum mechanically would there be bound states, quasi-bound states, or no bound states? If there are quasi-bound states, how long do we expect these states to last?

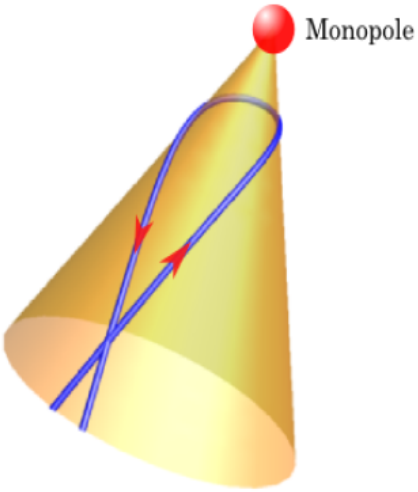

Figure 1.4: An electrons Geodesic trajectory around a magnetic monopole, in three dimensions Poincaré found that no bound states can be formed. Figure referenced from [17].

1.3 Can the Hall effect be Used to Detect Magnetic Monopoles?

The Hall effect produces a voltage in the transverse direction to an applied current in a magnetic field, this voltage is called the Hall voltage. The value of the Hall voltage is dependent on: the current, material properties, the charged particle density, and the strength of the magnetic field applied [19]. When the applied current and the material property are fixed, the Hall voltage is proportional to the magnetic field passing through the material.

In many physical phenomena, a substance known as plasma is being investigated. Some of these phenomena include astrophysical jets [20], sunspots [21] and nuclear fusion [22]. Plasma is a fluid that consists of charged particles. Modelling of fluids is done with the Navier-Stokes equation, a current millennium prize problem [23], but this does not deal with interactions between electric and magnetic fields that a plasma may come into contact with.

To solve this problem a variation of fluid dynamics was required and so the area of Magnetohydrodynamics was developed.

Calculating the Hall voltage from magnetohydrodynamics will allow for measurement of Hall voltage across the plane in addition to how the electron gas moves over the plane and its velocity. The benefit of a magnetohydrodynamic approach is that a non-uniform magnetic field produced by a magnetic monopole can be evaluated in the same manner as a uniform magnetic field over the plane.

We see that Dirac monopoles have yet to be found, but suitable magnetic monopole alternatives are available. In three dimensions an electron cannot orbit a magnetic monopole as it has a geodesic trajectory which maps onto the surface of a cone. If the electron is restricted to two dimensions can bound states be found?

The Hall effect is a technique currently used to measure the strength of magnetic fields. In combination with magnetohydrodynamics, can I measure the Hall voltage of non-uniform magnetic fields?

Starting the investigation with a classical and semi-classical treatment, I address the problem with a Lagrangian solution and also a Bohr-Sommerfeld quantisation. Following this, I address the quantum problem which is solved using a WKB approximation and a numerical finite difference method. I then compare classical, semi-classical, and quantum solutions. Finally, I look at the expected lifetimes of the quasi-bound states found. Before this, however, a detailed introduction to the problem being considered is required.

Chapter 2

An Electron on a Plane Situated Above a Magnetic Monopole

The problem under consideration is: can a bound state be formed by an electron orbiting a single magnetic monopole? In three dimensions, the answer is no; the electron will follow a geodesic trajectory on the surface of a cone. Can restricting the electron to a plane produce bound states? This is the problem that this first project aims to answer. Before answering the problem though, a short bit of background knowledge is introduced to the reader that will be relevant for understanding the electron-monopole problem.

2.1 The Monopole Electron Problem

In this section I will describe the physical problem at hand and offer a semi-classical description of the physics. I consider a spinless electron of effective mass m and electric charge q_e confined to a plane situated a distance D above a magnetic monopole of charge Q_m which is fixed in position relative

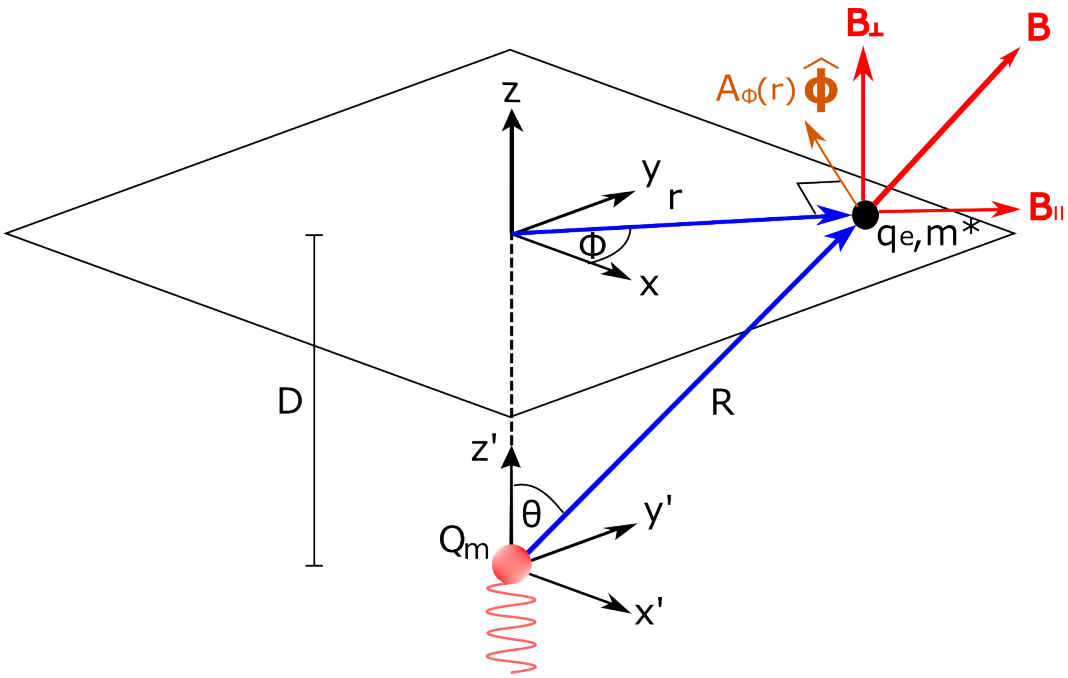

Figure 2.1: Graphical representation of the system under consideration. D is the distance between the plane and the magnetic monopole of charge Q_m. r is radial distance of the spinless electron from the centre of the plane, θ is the rotation on the surface of the plane about the position at which the magnetic monopole is projected onto the plane. The magnetic field, $\mathbf{B}$, is split into constituent magnetic fields; parallel, $B_{\parallel}$ and perpendicular, $B_{\perp}$. The electron has a charge q_e and mass m^*. The vector potential is denoted by $\mathbf{A}_{\phi}(r)$. The red oscillating line beneath the magnetic monopole represents the Dirac string that joins two oppositely charged monopoles.

to the plane, as shown in Fig. 2.1. Assuming that there is a lone magnetic monopole, the relationship between a magnetic field (**B**) and a magnetic vector potential (**A**) is the Maxwell equation rewritten to include magnetic monopoles [24,25]

$$\oint_{\mathbf{S}} \mathbf{B}.d\mathbf{S} = Q_m \mu_0, \tag{2.1}$$

where μ_0 is the magnetic permeability of free space. The magnetic field produced by the monopole is spherically symmetric. The magnetic field for a single magnetic monopole is:

$$\mathbf{B} = \frac{Q_m \mu_0}{4\pi r^2} \hat{r}. \tag{2.2}$$

The only part of the magnetic field that affects the motion of the electron is its perpendicular component ($\mathbf{B}_\perp$), measured on the plane that the electron is restricted to

$$\mathbf{B}_\perp = |\mathbf{B}| \frac{D}{\sqrt{r^2 + D^2}} \hat{z}, \tag{2.3}$$

which is perpendicular to the plane, making the problem analogous to the quantum hall effect. As the electron is confined to the plane a Coulomb gauge has been chosen such that $\nabla \cdot \mathbf{A} = 0$, where $\mathbf{A} = A_\phi(r)\hat{\phi}$ is the vector potential on the surface of the plane, where $\hat{\phi}$ is the unit vector of the polar coordinate on the plane around the point at which the monopole projects onto the plane. The momentums involved in this system are the linear momentum in the radial direction, the angular momentum in the polar direction [26]. The resulting Hamiltonian [27–30] (H) which describes the energy of the system

$$H = \frac{1}{2m} (\boldsymbol{p} + q_e \boldsymbol{A})^2 = \frac{1}{2m} \left(p_r^2 + \left[\frac{1}{r} p_\phi + q_e A_\phi(r) \right]^2 \right), \tag{2.4}$$

where q_e is the electric charge of the electron and $\mathbf{p}$ is its momentum; which can be separated into a linear momentum, p_r, and a canonical momentum, $p_\phi/r + q_e A_\phi(r)$. The angular momentum of the electron on its own is not conserved. However, the angular momentum of the electron and the angular momentum of magnetic field in the direction of ϕ is conserved, this is the canonical momentum [31].

The vector potential for a magnetic monopole can be modelled as two overlapping non-singular potentials. References [2, 32] show that vector potentials can be expressed as

$$\mathbf{A}_\phi = \begin{cases} \frac{\mu_0 Q_m}{4\pi} \frac{(1-\cos\theta)}{R\sin\theta}\hat{\phi}, & \mathbf{A}_r = \mathbf{A}_\theta = 0, \quad \text{for } \theta < \frac{\pi}{2}, \\ \frac{\mu_0 Q_m}{4\pi} \frac{(-1-\cos\theta)}{R\sin\theta}\hat{\phi}, & \mathbf{A}_r = \mathbf{A}_\theta = 0, \quad \text{for } \theta > \frac{\pi}{2}. \end{cases} \tag{2.5}$$

When modelling the system with the plane that confines the electron above the monopole, the required component of $\mathbf{A}_\phi$ is $\theta < \frac{\pi}{2}$ and for an electron below the monopole $\theta > \frac{\pi}{2}$. $\mathbf{A}_\phi$ can be expressed in terms of r using the identities $R = \sqrt{r^2 + D^2}$, $\cos\theta = \frac{D}{\sqrt{r^2+D^2}}$ and $\sin\theta = \frac{r}{\sqrt{r^2+D^2}}$ derived from figure 2.1 giving the term $\mathbf{A}_\phi(r)$

$$\mathbf{A}_\phi(r) = \frac{\mu_0 Q_m}{4\pi r}\left(1 - \frac{D}{\sqrt{r^2+D^2}}\right)\hat{\phi}. \tag{2.6}$$

2.2 Dimensionless Rescaling

In order to reduce the number of independent parameters as much as possible while retaining the physics of the problem, we introduce the following dimensionless variables:

$$\lambda = \frac{Q_m}{2Q_D}, \tag{2.7}$$

λ is the charge of the magnetic monopole in units twice the elementary monopole charge ($n = 1$) derived by Dirac

$$Q_D = \frac{2\pi\hbar}{q_e \mu_0} n, \tag{2.8}$$

where n is an integer value. Q_D is a quantised value but λ is not due to Q_M not being quantised. The energy, E, is expressed as the dimensionless quantity, ϵ

$$\epsilon = \frac{2E}{\hbar\omega_c}. \tag{2.9}$$

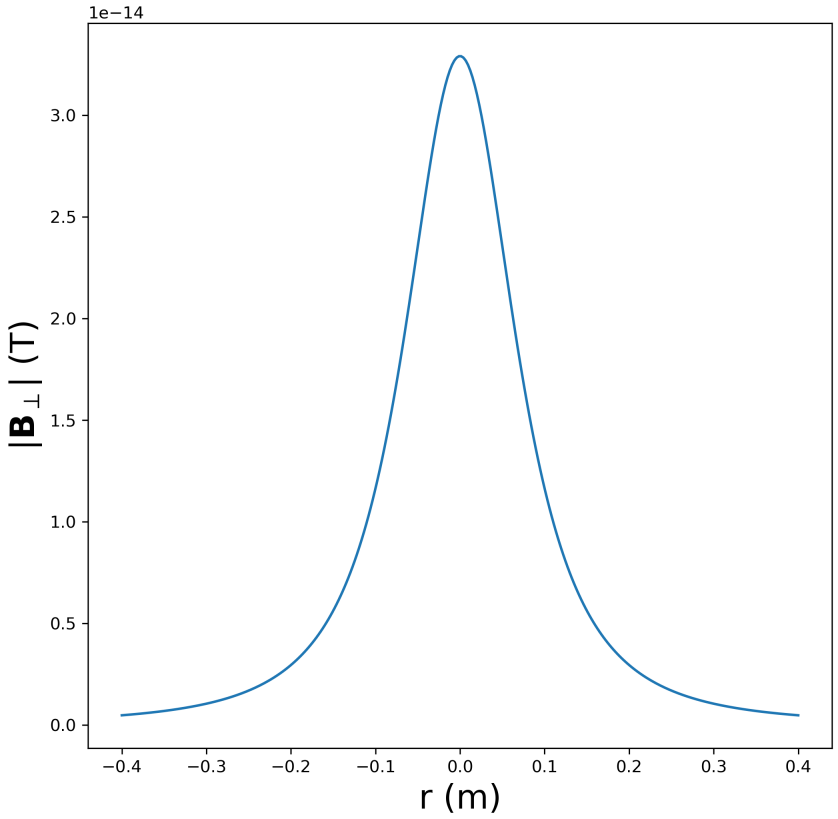

Figure 2.2: $|B_\perp|$ at the plane caused by a magnetic monopole located at $r = 0$ m and $D = 0.1$ m. The highest perpendicular magnetic field is located at the point directly above the magnetic monopole, it is this point at which we will use for defining our value of ω_c.

Here ω_c is the cyclotron frequency in a uniform field corresponding to the

highest field seen by the electron on the plane which is the directly above the magnetic monopole (see Fig. 2.2)

$$\omega_c = \frac{q_e \, |\mathbf{B}|}{\lambda m*}. \tag{2.10}$$

The dimensionless time, t', is

$$t' = t\omega_c, \tag{2.11}$$

where t is the time in seconds. Finally the radial position of the electron on the plane from the point where the monopole is projected can be rescaled as

$$\rho = r/D. \tag{2.12}$$

Chapter 3

A Classical Solution

The classical movement of the electron on a plane has two components a radial and an angular motion. In this section I look at solving the orbital paths utilising Lagrangian mechanics, looking at both the scattering and bound orbits. A classical description was originally attempted J.Minns in their Masters thesis, [33], calculated with Newtonian mechanics but here we take a different approach using Lagrangians to achieve the same orbital trajectories but being able to class each orbit type by the canonical momentum.

3.1 Applying Lagrangian Mechanics to the Problem

A description of how the equations of motion can be generated by Lagrangian mechanics and the methods used to solve these equations of motion are found in Appendix A.1. From the Hamiltonian

$$H = \frac{1}{2m}\left(\boldsymbol{p} + q_e\boldsymbol{A}\right)^2 = \frac{1}{2m}\left(p_r^2 + \left[\frac{1}{r}p_\phi + q_e A_\phi(r)\right]^2\right), \tag{3.1}$$

the Lagrangian can be derived using the transform $L = \sum \dot{q}_i p_i - H$ using the Hamiltonian identities [34,35], where $\dot{q}_i$ is the velocity in direction i and p_i is its corresponding momentum.

$$\dot{r} = \frac{\partial H}{\partial p_r} = \frac{p_r}{m} \longrightarrow p_r = m\dot{r}; \tag{3.2}$$

$$\dot{\phi} = \frac{\partial H}{\partial p_\phi} = \frac{1}{mr}\left(\frac{1}{r}p_\phi + q_e A_\phi(r)\right) \longrightarrow p_\phi = mr^2\dot{\phi} - q_e r A_\phi(r). \tag{3.3}$$

Substituting p_r andp_ϕ into the Hamiltonian and the Legendre transform we get:

$$L = m\dot{r}^2 + mr^2\dot{\phi}^2 - \dot{\phi}q_e r A_\phi - \frac{1}{2}\left(m\dot{r}^2 + mr^2\dot{\phi}^2\right), \tag{3.4}$$

which can be simplified to

$$L = \frac{1}{2}m\left(\dot{r}^2 + r^2\dot{\phi}^2\right) - q_e r\dot{\phi}A_\phi. \tag{3.5}$$

The Euler-Lagrange equation, [36,37] for radial motion is as follows

$$\frac{\partial L}{\partial r} - \frac{\partial}{\partial t}\frac{\partial L}{\partial \dot{r}} = 0. \tag{3.6}$$

Evaluating Eq. (3.6) with the Lagrangian Eq. (3.5) gives the following equation of motion:

$$m\ddot{r} = mr\dot{\phi}^2 - \dot{\phi}q_e\frac{\partial}{\partial r}\left(rA_\phi(r)\right). \tag{3.7}$$

The canonical momentum, $\frac{\partial L}{\partial \dot{\phi}} = M_\phi$, is conserved about a single monopole. This is evaluated as

$$M_\phi = mr^2\dot{\phi} - q_e r A_\phi(r), \tag{3.8}$$

giving an angular velocity of

$$\dot{\phi} = \frac{1}{mr}\left(\frac{M_\phi}{r} + q_e A_\phi(r)\right). \tag{3.9}$$

We see that there is an implied periodicity in the polar position of the electron from Eq. (3.9) if r is an electron constrained to periodically bounce between two radial points then ϕ will also be periodic. Substituting Eq. (3.9) into Eq. (3.7) gives the following radial equation of motion

$$m\ddot{r} = -\frac{1}{2m}\frac{\partial}{\partial r}\left(\frac{M_\phi}{r} - q_e A_\phi(r)\right)^2. \tag{3.10}$$

Eqs. (3.9) and (3.10) are both dependent on the position of the electron in the r direction, this allows us to reframe the problem as one dimensional. An effective one dimensional potential, $V_{\text{classical}}$(r), can be derived using $m\ddot{r} = -\frac{\partial V^{\text{unscaled}}_{\text{classical}}(r)}{\partial r}$:

$$V^{\text{unscaled}}_{\text{classical}}(r) = \frac{1}{2m}\left(\frac{M_\phi}{r} - q_e A_\phi(r)\right)^2. \tag{3.11}$$

Substituting $A_\phi(r)$, Eq. (2.6) into Eq. (3.11) and scaling the potential energy in terms of ϵ using the relation in Eq. (2.9) and using the scaling relationships Eqs. (2.9) and (2.12) $V^{\text{unscaled}}_{\text{classical}}(r)$ can be expressed as a dimensionless quantity $V_{\text{classical}}(\rho)$:

$$V_{\text{classical}}(\rho) = \frac{2}{\hbar\omega_c} V^{\text{unscaled}}_{\text{classical}}(\rho D), \tag{3.12}$$

which expanded gives

$$V_{\text{classical}}(\rho) = \frac{\lambda^2}{\rho^2}\left[\frac{M}{\lambda} + \left(1 - \frac{1}{\sqrt{1+\rho^2}}\right)\right]^2, \tag{3.13}$$

where

$$M_\phi = M\hbar \tag{3.14}$$

The shape of the potential is dependent on two fixed quantities λ^2 and M/λ. Dividing the energy values by λ^2 which affects the scale of the potential Eq. (3.13) the shape of the potential and results can be generalised in terms

of M/λ. The shape of $V_{\text{classical}}(\rho)/\lambda^2$ is now only dependent on the value of M/λ. Anticipating later sections the distinction between the classical and quantum variants of M need to be expressed. This is a classical description, the value of M does not have to be restricted to integer values, as would be the case for quantum solutions. The value of M/λ is not quantised for either classical or quantum problems as λ is not quantised owing to the fact that Q_M is not a quantised monopole charge. How the potential changes with M/λ can be seen in Fig. 3.1. Radial energy values that are less than the peak of the well and also at a radius that falls within the well will be bound orbits, energy values and radius that fall outside these constraints the electron will be unbound, this can be seen in Fig. 3.2.

3.2 Solving the Classical Problem

Previously I have described a non-dimensional classical potential for the radial part of the electrons motion, Eq. (3.13). Following on from the non-dimensional potential we can now give the angular velocity the same treatment

$$\dot{\phi}(\rho) = \frac{1}{\omega_c}\dot{\phi}(\rho D), \tag{3.15}$$

expanding gives

$$\dot{\phi}(\rho) = \frac{\lambda}{\rho^2}\left[\frac{M}{\lambda} + \left(1 - \frac{1}{\sqrt{\rho^2+1}}\right)\right]. \tag{3.16}$$

The next step is to form a non-dimensional Lagrangian by applying the energy scalar (Eq. (2.9)) to the Lagrangian (Eq. (3.5))

$$L(\rho, \phi) = \frac{2}{\hbar\omega_c}L(\rho D, \phi(\rho D)), \tag{3.17}$$

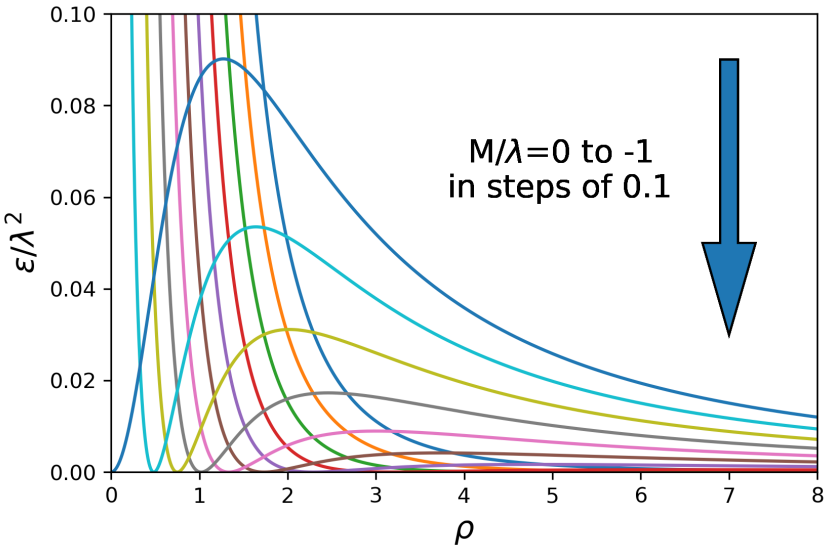

(a)

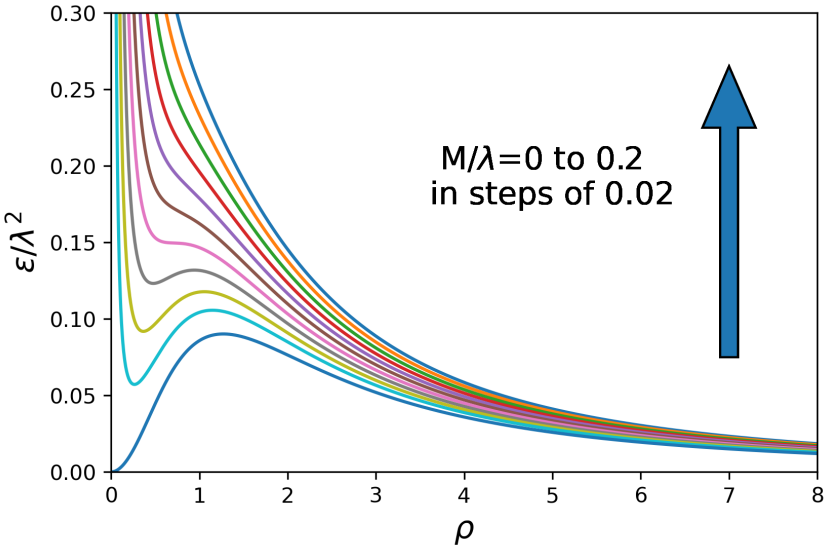

(b)

Figure 3.1: The shape of the classical potential, $V_{classical}(\rho)$ is dependent on M/λ. The y-axis is the energy of the potentials shown ,ϵ, which has been scaled by λ^2. (a) M/λ decreasing from 0 to -1 in step sizes of 0.10 in the direction of the arrow. (b) M/λ increasing from 0 to 0.2 in step sizes of 0.02 in the direction of the arrow.

giving

$$L(\rho,\phi) = \dot{\rho}^2 + \rho^2\dot{\phi}^2 - 2\dot{\phi}\lambda\left(1 - \frac{1}{\sqrt{\rho^2+1}}\right). \tag{3.18}$$

Using the Euler-Lagrange equations

$$\frac{\partial L(\rho,\phi)}{\partial \rho} - \frac{\partial}{\partial t'}\frac{\partial L(\rho,\phi)}{\partial \dot{\rho}} = 0, \tag{3.19}$$

$$\frac{\partial L(\rho,\phi)}{\partial \phi(\rho)} - \frac{\partial}{\partial t'}\frac{\partial L(\rho,\phi)}{\partial \dot{\phi}(\rho)} = 0. \tag{3.20}$$

$$\tag{3.21}$$

Solving the Euler-Lagrange equations then manipulating both to get $\ddot{\rho}$

$$\ddot{\rho} = \rho\dot{\phi}^2(\rho) + \frac{\dot{\phi}(\rho)\lambda\rho}{(\rho^2+1)^{\frac{3}{2}}}, \tag{3.22}$$

and $\ddot{\phi}(\rho)$

$$\ddot{\phi}(\rho) = -\frac{2\dot{\rho}}{\rho}\left[\dot{\phi}(\rho) + \frac{\lambda}{2\,(\rho^2+1)^{\frac{3}{2}}}\right]. \tag{3.23}$$

Now that we have a pair of coupled equations, $\ddot{\rho}$ and $\ddot{\phi}$, we can solve these using the python package scipys odeint module. This requires the initial positions, initial velocities and the time period over which to collect data. For a bound state we can choose an initial ρ as being halfway across the width of the potential well for a chosen electron energy (see Fig. 3.2) and the initial $\phi = 0$. The initial velocity $\dot{\phi}$ can be evaluated using Eq. (3.16). The initial velocity in the radial direction can be evaluated via the potential scaling the kinetic energy ($E - V^{\text{unscaled}}_{\text{classical}}(r) = mv^2/2$) by the energy scalar, Eq. (2.9), and rearranging for velocity we get:

$$\dot{\rho}(\rho) = \sqrt{\epsilon - V_{\text{classical}}(\rho)}. \tag{3.24}$$

Choosing an initial starting point at a radius that is outside of the well but above the potential and with the corresponding initial radial velocity at that position, also calculated form the potential, we can observe the scattering states that move away from the magnetic monopole. The trajectories of the electrons bound and scattering states can be seen for different values of M/λ in Fig. 3.3

3.3 Classical results

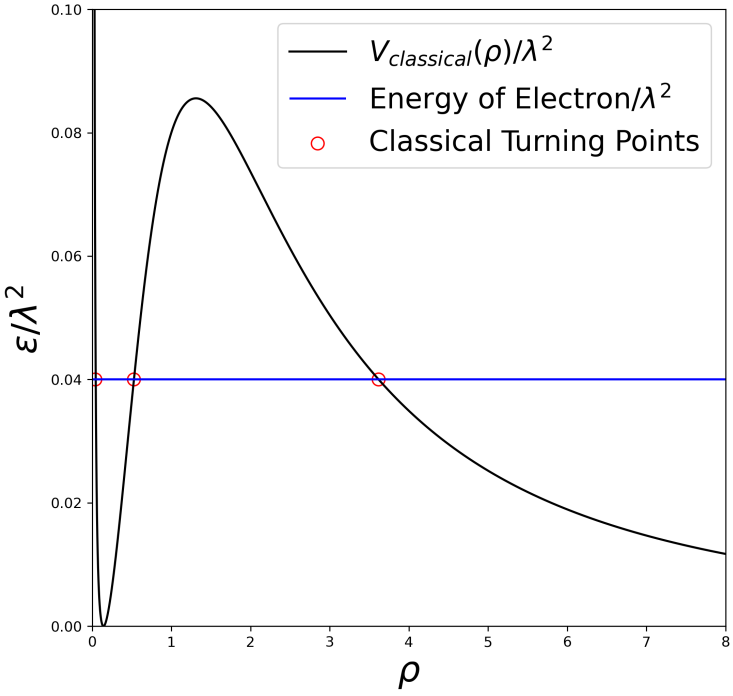

(a)

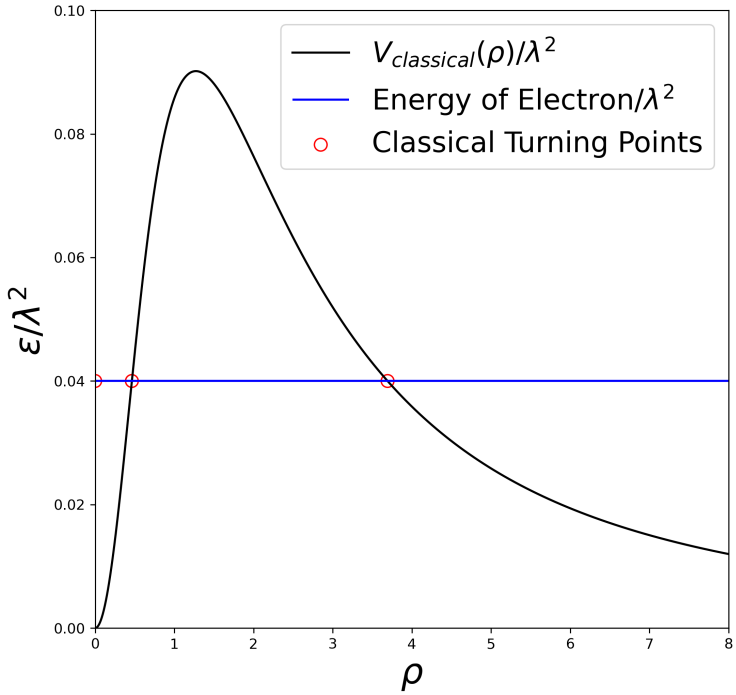

(b)

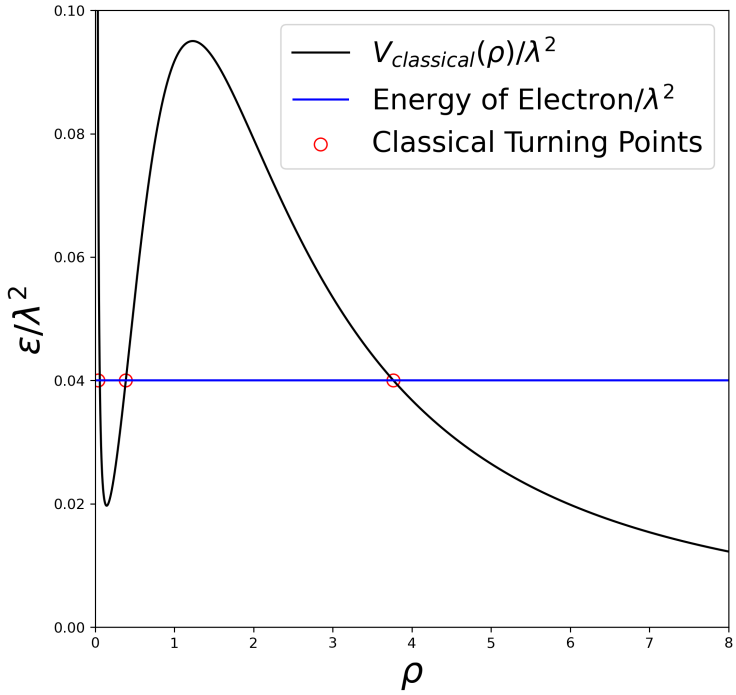

(c)

Figure 3.2: Potentials with a chosen electron energy of $\epsilon/\lambda^2 = 0.04$. The classical turning points for the bound orbits, $\rho 1$,$\rho 2$ and $\rho 3$, are shown by the red circles in ascending order from $\rho = 0$. (a) $M/\lambda = -0.01$. (b) $M/\lambda = 0$. (c) $M/\lambda = 0.01$.

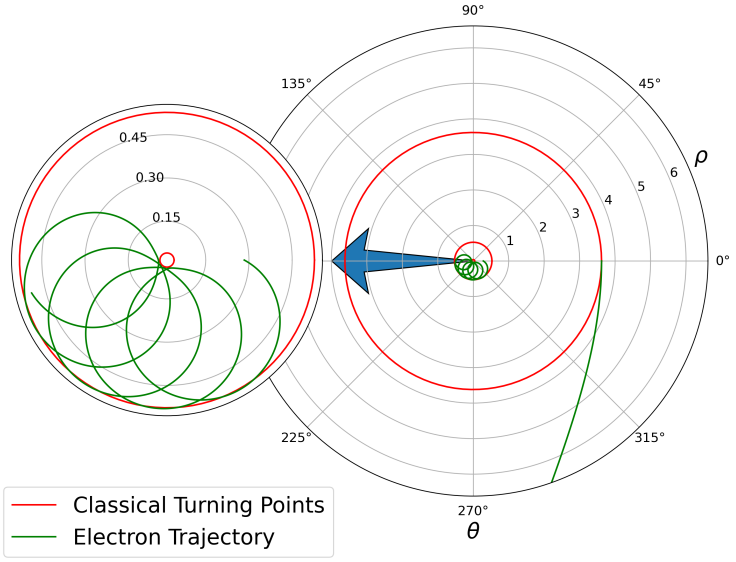
90°
135°
45°
225°
315°
270°
0°
ρ
θ
0.45
0.30
0.15
1
2
3
4
5
6
Classical Turning Points
Electron Trajectory

(a)

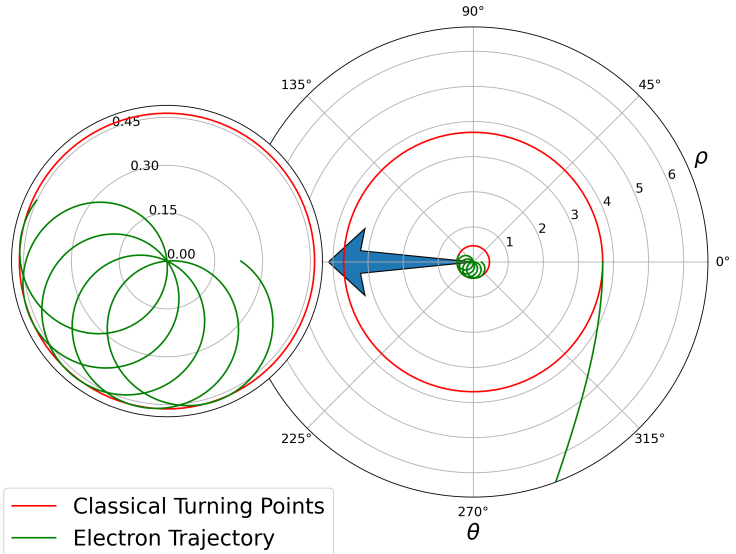
90°
135°
45°
225°
315°
270°
0°
ρ
θ
0.45
0.30
0.15
0.00
1
2
3
4
5
6
Classical Turning Points
Electron Trajectory

(b)

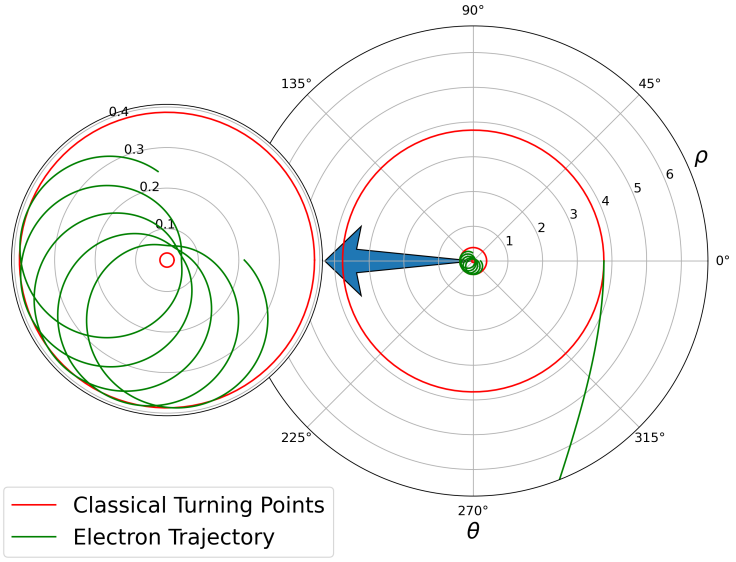

(c)

Figure 3.3: Orbits for the potentials and electron energy seen in Fig. 3.2 with one orbit starting within the well and one starting outside the well for the same value of energy. The starting position outside the well is scattered away from the monopole and unbound. The magnified section shows the bound state within the potential well. The red circles show the classical turning points from the potential. (a) $M/\lambda = -0.01$. (b) $M/\lambda = 0$. (c) $M/\lambda = 0.01$.

The orbits all travel around the origin in the same direction regardless of the value of M/λ, while we may think of M as an angular momentum, it is, in fact, a conserved canonical angular momentum. There are four distinct types of orbit, three are seen in Fig. 3.3, the final type of orbit are circular orbits around the origin. Evaluating $\frac{\partial L(\rho,\phi)}{\partial \dot{\phi}}$ and rearranging for $\dot{\phi}$

$$\dot{\phi} = \frac{1}{\rho^2}\left[\frac{M}{2} - \lambda\left(1 - \frac{1}{(\rho^2+1)^{\frac{1}{2}}}\right)\right]. \tag{3.25}$$

Substituting the angular velocity into the dimensionless radial equation of motion, Eq. (3.22), we get:

$$\ddot{\rho} = \frac{1}{\rho^2}\left(\frac{M}{2} - \lambda\left[1 - \frac{1}{\sqrt{\rho^2+1}}\right]\right)\left[\frac{1}{\rho}\left(\frac{M}{2} - \lambda\left[1 - \frac{1}{\sqrt{\rho^2+1}}\right]\right) + \frac{1}{\sqrt{\rho^2+1}}\right]. \tag{3.26}$$

Using the equation of motion, Eq. (3.26) circular orbits are only obtained when

$$\frac{1}{\rho}\left(\frac{M}{2}-\lambda\left[1-\frac{1}{\sqrt{\rho^2+1}}\right]\right)+\frac{1}{\sqrt{\rho^2+1}}=0, \tag{3.27}$$

a state where no radial force acts on the electron. Looking at Fig. 3.4 we can see that the majority of bound orbit types are for a negative value of M.

Circular orbits are found in the troughs of $V_{\text{classical}}(\rho)$ for positive values of M/λ and on the potential peaks for all values of M/λ. These are stable and unstable orbits, respectively. Circular orbits are not found at the bottom of the well when M/λ is negative; the bottom of the well sits at zero energy, so the electron will not move radially and would not be subject to any force from the magnetic field. These types of circular orbit are stable owing to the fact that any slight perturbation will push them up the well and the electron when it loses this extra energy can only go back to the bottom of the potential well. The unstable circular orbits are at the peak of the potential any perturbations here will push the electron into the well or out of the well and into a scattering state. Since this is a purely classical description of the system for any given radius, there is a circular orbit if a suitable value of M/λ is chosen. The distribution of circular orbits can be seen in Fig. 3.4, where we can see that the stable and unstable circular orbits separate the bound and scattering states.

Classically bound orbits can be found at all values of ρ by varying M/λ, λ and choosing an appropriate energy so that the electron is found within the well.

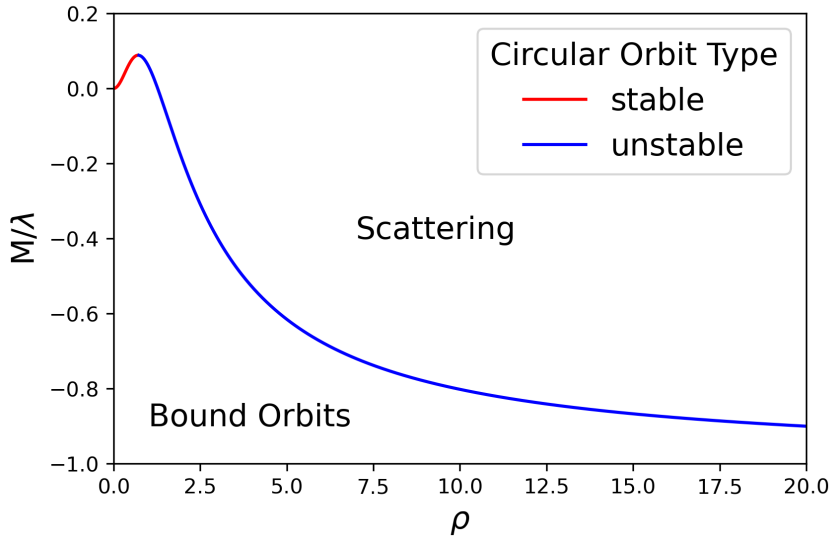

Figure 3.4: Relationship between angular momentum, M/λ, and distance from the centre ρ for circular orbits. Above the curve all orbits are unbound below they are non-circular-bound orbits, see fig. 3.3. This plot is generated by solving Eq. (3.27) for ρ with a given value of M/λ.

3.4 Classical Solutions to the Problem Review

Bound orbits can be found for a given energy as long as the electron is within the well of the $V_{\text{classical}}$, outside of the potential well the electrons are scattered. The type of bound orbit can take one of three types, Fig. 3.3, dependent on the value of M/λ but all travel the same direction about the magnetic monopole. A type of orbit which is circular can be found, the circular orbits form a boundary between the bound orbits and the scattered states of the electron, see Fig. 3.4.

Chapter 4

Semi-Classical Solutions Using the Classical Potential

In this chapter our focus is on the semi-classical solutions to the bound states of an electron confined to two dimensions while in the presence of a stationary magnetic monopole. The initial investigation will be on a simple harmonic oscillator approximation, counting the number of bound states that can occur for a given angular momentum. The next point of interest will be Bohr-Sommerfeld quantisation. Originally used to model the hydrogen atom, which consists of an electron orbiting an atomic nucleus, replacing the atomic nucleus with a magnetic monopole the old quantum theory will be able to model the bound states.

4.1 Harmonic Oscillator Approximation to the Number of Bound States

Having a classical solution, one of the next areas of investigation would be a quantum mechanical solution; what can we gleam about the quantum mechanical problem from the classical one? There are several methods that can be utilised to approximate a quantum solution but here we use the model of a harmonic oscillator. Assuming that the electron can be modelled as a harmonic oscillator, bouncing between the two walls of the potential well, an approximation for the number of quantum bound states, $N_{M/\lambda}$, for a chosen M/λ can be evaluated. The energy of a classical harmonic oscillator can be expressed at a quantum scale as

$$\epsilon_N = \frac{1}{2}\omega_0^2 \rho_c^2, \tag{4.1}$$

where ω_0 is the angular frequency of the harmonic oscillator and ρ_c is the width of the well at the chosen energy see Fig. 4.1. The energy for a quantum harmonic oscillator is

$$\epsilon_N = \omega_0 \left(N + \frac{1}{2} \right). \tag{4.2}$$

This in turn gives us an approximation to the number of quantum states as

$$N \approx \frac{\epsilon_N}{\omega_0}. \tag{4.3}$$

Rearranging and substituting Eq. (4.1) into Eq. (4.3)

$$N \approx \frac{\sqrt{\epsilon_N}}{\sqrt{2}} \rho_c. \tag{4.4}$$

The number of states is an approximation using the energy at half the height of the well and the width at the corresponding height (Fig. 4.1), both of which

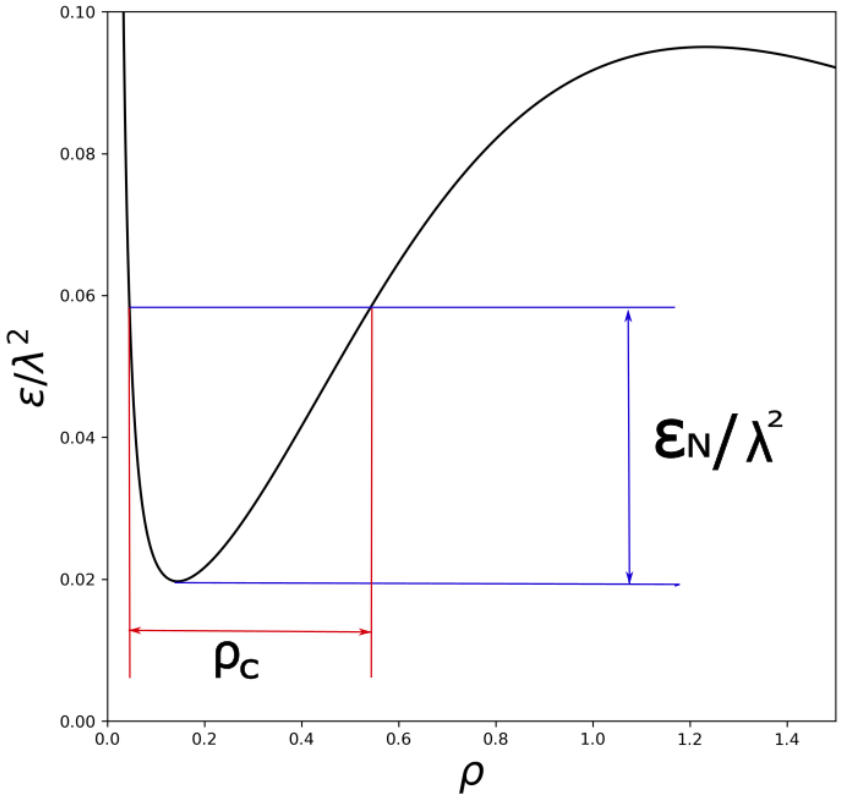

Figure 4.1: The well of $V_{\text{classical}}(\rho)/\lambda^2$ detailing the where values for the variables ρ_c and ϵ_N/λ^2 are taken in the potential.

will be dependent on M/λ.The number of bound states, N, for a given M/λ can be stated as Scaling ϵ_N by $1/\lambda^2$ gives

$$N_{M/\lambda} \approx \frac{\sqrt{\epsilon_N}}{\sqrt{2}\lambda}\rho_c. \tag{4.5}$$

The reason for doing this is $N_{M/\lambda}$ is N scaled by $1/\lambda$ so the plot, Fig. 4.2, represents all values of λ. The total number of bound states for any λ , $\sum N_{M/\lambda}$, is the area under the graph, 12.51, in fig. 4.2 and is scaled by λ^2. This value is independent of D as the characteristic magnetic length scale is proportional to D for a fixed value of Q_m

$$\sum_M N_{M/\lambda} \approx 0.13\lambda^2. \tag{4.6}$$

The total number of states that has been calculated here will be returned to during the exploration of the quantum problem. It will allow us to compare the total number of states between the two regimes highlighting how accurate (or not) the harmonic oscillator approximation.

4.2 The Bohr-Sommerfeld Quantisation Applied to the Problem

Bohr-Sommerfeld quantisation is applicable to periodical motion with one degree of freedom [38–40], a separate Bohr-Sommerfeld equation is required for each degree of freedom. A derivation of the Bohr-Sommerfeld quantisation condition can be found in Appendix A.2. Assuming the orbital momentum and radial momentum are separable, as with techniques such as the finite difference method and WKB methods (which we will come to later on), we can use the Bohr-Sommerfeld quantisation rule in a similar method

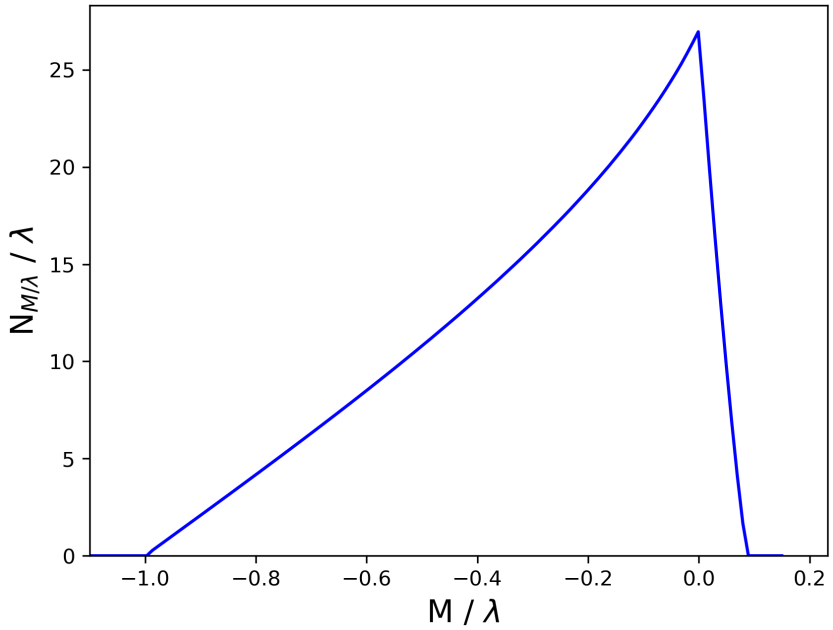

Figure 4.2: The number of bound states compared to M/λ, both scaled by λ, by modelling the system as a simple harmonic oscillator.

as Sommerfeld applied it to the Hydrogen atom [41].

4.3 Applying Bohr-Sommerfeld Quantisation

We now have all the components required to derive the Bohr-Sommerfeld quantisation for the electron on a plane above a magnetic monopole. Starting with the circular motion the Bohr-Sommerfeld equation Eq. (A.5) becomes

$$\oint L d\phi = (M + 0)\, h, \tag{4.7}$$

where L is the angular orbital momentum, M is the corresponding angular momentum quantum number, and ϕ is the angular coordinate. The Maslov index $\gamma = 0$ as the start and end points of the Lagrangian paths are the same but act in opposite directions [42]. The quantum number for the angular momentum is given by $M = \ldots, -2, -1, 0, 1, 2, \ldots$. Adding in the limits of integration of 0 and 2π and solving gives the quantised angular momentum

as

$$\int_0^{2\pi} L d\phi = Mh, \qquad L = M\hbar, \tag{4.8}$$

which is the same result for Bohr-Sommerfeld quantisation for a circular orbit as [43]. The quantisation of the radial momentum $P_r(r)$ is given by

$$\oint P_r(r) dr = (n + \gamma)h. \tag{4.9}$$

The closed path of the electron is from position r_1 to position r_2 then returning back to position r_1. This allows us to rewrite the integral of Eq. (4.9) as

$$2\int_{r_1}^{r_2} P_r(r) dr = \left(n + \frac{1}{2}\right) h. \tag{4.10}$$

where $n = 1, 2, 3, \ldots$. r_1 and r_2 are given by the classical turning points where $P_r(r) = 0$. Derivation of $P_r(r)$ can be made through the fact that the total energy of the system is given by $E = \frac{1}{2m}\left(P_r^2(r) + P_\phi^2(\phi)\right)$, where $P_\phi = mv_t - eA_\phi$ is the polar momentum [44], where v_t is the tangential velocity. Substituting Eq. (2.6) into the P_ϕ and also putting in the quantised angular momentum, by only allowing classical values such that $M = rmv_t$, results in

$$P_\phi = \frac{\hbar}{r}\left[M + \lambda\left[1 - \frac{D}{(D^2 + r^2)^{\frac{1}{2}}}\right]\right], \tag{4.11}$$

where λ is given by Eq. (2.7). Now we have the components to evaluate the total energy of the system

$$E = \frac{P_r^2(r)}{2m} + \frac{\hbar^2}{2mr^2}\left[M + \lambda\left[1 - \frac{D}{(D^2 + r^2)^{\frac{1}{2}}}\right]\right]^2. \tag{4.12}$$

Putting the above equation in the same length scale as used in Chapter 3 and the future Section 5.2 and Appendix C for direct comparison. Rescaling

Eq. (4.12) using Eqs. (2.9) and (2.12) and P_ρ is the linear momentum gives the dimensionless energy equation

$$\epsilon = \frac{P_\rho^2(\rho)}{\hbar^2} + \frac{\lambda^2}{\rho^2}\left[\frac{M}{\lambda} + \left[1 - \frac{1}{(1+\rho^2)^{\frac{1}{2}}}\right]\right]^2. \tag{4.13}$$

Rearranging for the linear momentum $P_\rho(\rho)$

$$P_\rho(\rho) = \hbar\sqrt{\epsilon - \frac{\lambda^2}{\rho^2}\left[\frac{M}{\lambda} + \left[1 - \frac{1}{(1+\rho^2)^{\frac{1}{2}}}\right]\right]^2}. \tag{4.14}$$

Now the Bohr-Sommerfeld quantisation for the radial motion Eq. (4.10) can be evaluated in the coordinate basis ρ as

$$\frac{1}{\pi}\int_{\rho_1}^{\rho_2}\sqrt{\epsilon - \frac{\lambda^2}{\rho^2}\left[\frac{M}{\lambda} + \left[1 - \frac{1}{(1+\rho^2)^{\frac{1}{2}}}\right]\right]^2}\,d\rho = \left(n + \frac{1}{2}\right), \tag{4.15}$$

where $n = 0, 1, 2, \ldots$ and $M = \ldots, -2, -1, 0, 1, 2, \ldots$. The turning points ρ_1 and ρ_2 can be evaluated by finding the positive two roots closest to $\rho = 0$ with the equation

$$\epsilon - \frac{\lambda^2}{\rho^2}\left[\frac{M}{\lambda} + \left[1 - \frac{1}{(1+\rho^2)^{\frac{1}{2}}}\right]\right]^2 = 0. \tag{4.16}$$

For a given value of ϵ a pair of turning points can be derived using Eq (4.16). Using the values of $\epsilon, \rho_1,$ and ρ_2 the Bohr-Sommerfeld quantisation can be computed and a value returned for n using Eq. (4.15). If the value for n is not integer (or close enough to an integer value for an acceptable level of accuracy) then the value of ϵ is not an energy eigenvalue for a bound state. Incrementally increasing ϵ (this step size should be sufficiently small so as to get as close to a integer value of n as possible), and repeating the process until there are no further classical turning points, all energy eigenvalues can

be found for a given system.

4.4 Semi-Classical Solutions Using the Classical Potential Review

The harmonic oscillator approximation shows that we should expect larger amounts of bound states closer to $M = 0$ when we move onto a quantum mechanical solution in the next chapter. The semi classical Bohr-Sommerfeld quantisation results will be presented later on with the quantum mechanical results for direct comparison. Next though we develop a one dimensional quantum mechanical problem that we can evaluate using WKB approximation and a finite difference method.

Chapter 5

The Electron Monopole Problem in Quantum Mechanical Framework

The problem is now expressed in a quantum mechanical framework. The semi-classical technique that I use here is the WKB approximation, to produce energy eigenvalues and wavefunctions which we can compare to the numerical finite difference solution later on. Before that however we introduce a derivation of the quantum potential and compare against the classic potential derived in Chapter 3.

5.1 The quantum Mechanical Electron Monopole Problem

The time independent Schrödinger equation is given as

$$\hat{H}\psi(r,\phi) = E\psi(r,\phi), \tag{5.1}$$

where $\hat{H}$ is the Hamiltonian energy operator, E is the energy eigenvalue, and $\psi(r,\phi)$ is corresponding energy eigenfunction in a polar position basis. The coordinate choice is in this form as the electrons motion is centred about a magnetic monopole below the plane. The Hamiltonian for the quantum mechanical version of the electron in a magnetic field is

$$\hat{H} = \frac{1}{2m}\left(-i\hbar\nabla + q_e\mathbf{A}\right)^2. \tag{5.2}$$

Substituting into the time independent Schrödinger equation gives

$$\frac{1}{2m}\left[\hat{p} + q_e\mathbf{A}_\phi(r)\right]^2\psi\left(r,\phi\right) = E\psi\left(r,\phi\right). \tag{5.3}$$

A solution of $\Psi\left(r,\phi\right) = G(r)\mathrm{e}^{iM\phi}$ is chosen, where $G(r)$ is a function of r and M is the quantum angular momentum number and $A_\phi(r)$ is given by Eq. (2.6). The Schrödinger equation is evaluated as

$$-\frac{\hbar^2}{2m}\frac{\partial^2 G(r)}{\partial r^2} - \frac{\hbar^2}{2mr}\frac{\partial G(r)}{\partial r} + \frac{\hbar^2 M^2 G(r)}{2mr^2} + \frac{g\hbar q_e M G(r) H}{2mD^2} + \frac{g^2 q_e^2 r^2 G(r) H^2}{8mD^4} = EG(r), \tag{5.4}$$

where

$$g = \frac{Q_m\mu_0}{4\pi} = \frac{\lambda\hbar}{q_e}, \qquad \text{and} \qquad H = \frac{2D^2}{r^2}\left(1 - \frac{D}{\sqrt{D^2+r^2}}\right). \tag{5.5}$$

To produce a dimensionless radial equation (Eq. (5.6)) the scaling relationship Eq. (2.9) is utilised along with Eq. (2.12). This gives a radial dimensionless equation

$$-\frac{d^2G(\rho)}{d\rho^2} - \frac{1}{\rho}\frac{dG(\rho)}{d\rho} + V(\rho)G(\rho) = \epsilon G(\rho). \tag{5.6}$$

Here $V(\rho)$ is defined as

$$V(\rho) = \frac{\lambda^2}{\rho^2}\left[\frac{M}{\lambda} + \left(1 - \frac{1}{\sqrt{1+\rho^2}}\right)\right]^2. \tag{5.7}$$

This coincides with the classical potential, $V_{\text{classical}}(\rho)$, in Eq. (3.13). However $V(\rho)$ does not play the role of effective potential for the quantum problem, as we shall see now.

Using the substitution $G(\rho) = \psi(\rho)\rho^{-\frac{1}{2}}$ a one dimensional Schrödinger equation can be derived, where $\psi(\rho)$ are the solutions. The one-dimensional Schrödinger equation is

$$-\frac{d^2\psi(\rho)}{d\rho^2} + V_{\text{quantum}}(\rho)\psi(\rho) = \epsilon\psi(\rho), \tag{5.8}$$

with the potential $V_{\text{quantum}}(\rho)$ given by

$$V_{\text{quantum}}(\rho) = \frac{\lambda^2}{\rho^2}\left(\frac{M}{\lambda} + \left[1 - \frac{1}{\sqrt{1+\rho^2}}\right]\right)^2 - \frac{1}{4\rho^2}. \tag{5.9}$$

Here the quantum angular momentum number is $M = ... -1, 0, 1....$ There are no exact solutions to $\psi(\rho)$. Approximate methods were used to evaluate it analytically and numerically, which we will look at next after exploring the potential a little further.

The difference between the potentials $V_{\text{classical}}(\rho)$ (Eq. (3.13)) and $V_{\text{quantum}}(\rho)$ (Eq. (5.9)) is the additional term $-1/4\rho^2$ found in $V_{\text{quantum}}(\rho)$. The differences between the two potentials can be seen in Fig. 5.1. As the absolute value of M increases $V_{\text{quantum}}(\rho)$ and $V_{\text{classical}}(\rho)$ align. This happens quicker for positive values of M compared to negative values of M. The shape of the potential for $M = 0$ tends to a negative infinite energy as ρ goes to zero in the quantum case, while the classical potential goes to zero.

The Schrödinger equation has different potentials than its classical counterpart in all but one and three dimensions [45, 46], this is the cause for the discrepancy between the classical and quantum potentials but both are correct in their respective regime. A description of this is given in Appendix B where using the correct technique is required to get the correct quantum mechanical problem.

5.2 A Semi-Classical Solution Utilising The WKB Approximation

The WKB approximation allows an analytic solution to Schrödinger equation to be evaluated. It is a semi-classical theory utilising a quantum potential but assuming that a particle behaves classically. The WKB method has allowed regions where energy is greater than the potential energy and disallowed regions where energy is less than the potential energy.

5.3 The WKB Wavefunction

Plotting the potential for M=1, $\lambda = 100$ gives the curve shown in Fig. 5.2.

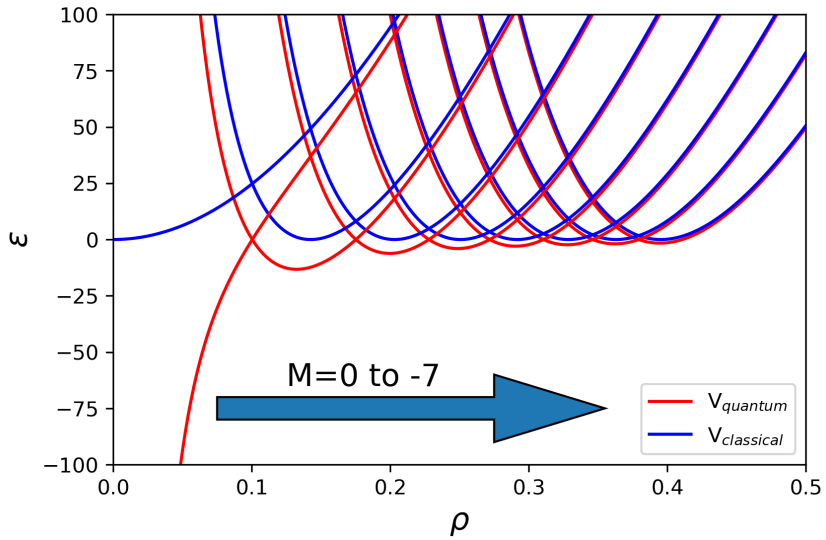

(a)

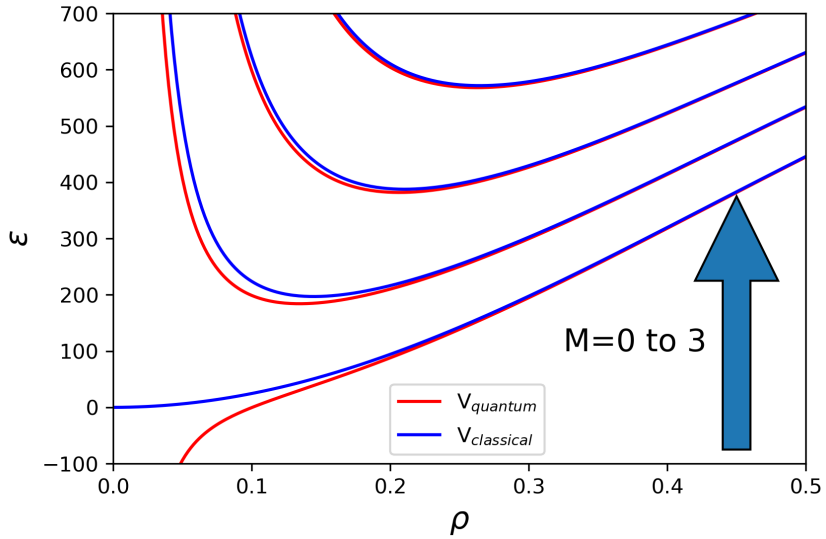

(b)

Figure 5.1: The comparison of the classical and quantum potentials with potential energy ϵ (a) M in the range 0 to -7, (b) M in the range 0 to 3. V_{quantum} is different form $V_{\text{classical}}$ for low values of M, as M is increased both potentials converge onto the same function.

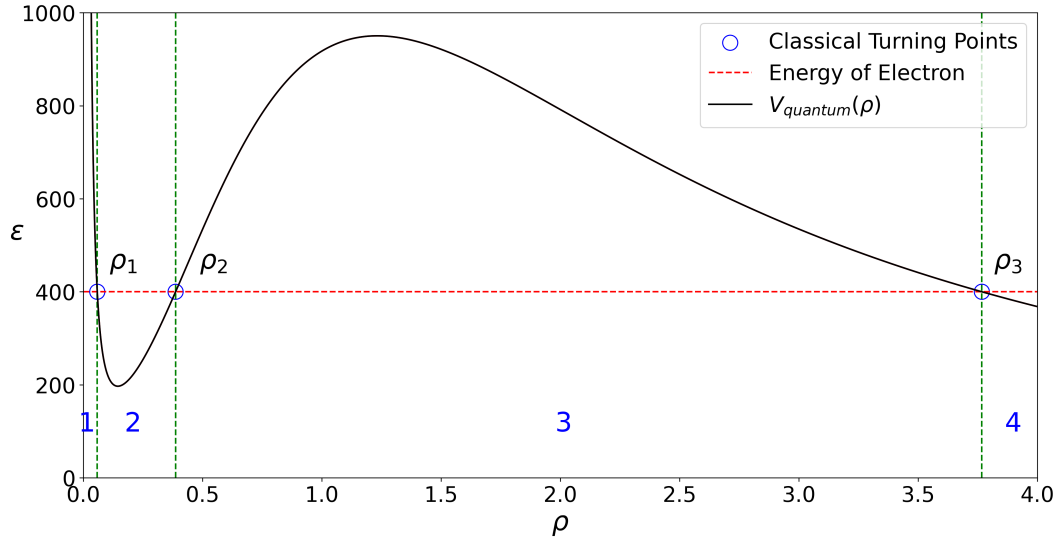

Figure 5.2: Plot of the potential $V_{quantum}(\rho)$ for $M = 1$ and $\lambda = 100$. The red circles ρ_1, ρ_2, ρ_3 are the classical turning points of an electron with an energy of $\epsilon = 400$ in this example. The classical turning points are the ρ coordinates at the intersection of a chosen energy with the potential. The intersection of the potential and the turning points forms four different regions in the potential two classically allowed regions 2 and 4 and two classically disallowed regions 1 and 3. Each one of these regions produces part of the piecewise wavefunction of the WKB approximation.

For a given value of ϵ between 200 and 950 there are three turning points. This splits the potential in to four sections, see Fig. 5.2. Each one of these sections will produce part of a WKB wave function. Using the method detailed in Appendix A.3 we can obtain the wavefunctions and their respective energies.

The first section to tackle is section 1. In section 1 an exponentially decreasing wavefunction is expected which decreases as ρ decreases due to $\epsilon < V(\rho)$. The appropriate choice is Eq. (A.22) with $D = 0$ and $\rho < \rho_1$

$$\psi_1(\rho) = \frac{C}{\sqrt{|P(\rho)|}} \exp\left[\int_{\rho_1}^{\rho} P(\rho')d\rho'\right]. \tag{5.10}$$

The third section follows the same logic except that the wave function should be decreasing as ρ increases. Once again the appropriate choice is Eq. (A.22)

with $C = 0$ and $\rho > \rho_2$

$$\psi_3(\rho) = \frac{D}{\sqrt{|P(\rho)|}} \exp\left[-\int_{\rho_2}^{\rho} P(\rho')d\rho'\right]. \tag{5.11}$$

To get the appropriate wavefunction for section four the connection formula Eq. (A.34) needs to be used. Before it can be used the wavefunction for section 3 needs to be reworked so that the limits of the integral are from the turning point at ρ_3 to ρ where $\rho_2 < \rho < \rho_3$ giving a exponential in section 3 as

$$\psi_3(\rho) = \frac{D}{\sqrt{|P(\rho)|}} \exp(J) \exp\left[-\int_{\rho_3}^{\rho} P(\rho')d\rho'\right], \tag{5.12}$$

where

$$J = -\int_{\rho_2}^{\rho_3} P(\rho)d\rho. \tag{5.13}$$

Now that $\psi_3(\rho)$ is in a form that can be used with the connection formula the wave function for section 4 can be chosen from the connection formula Eq. (A.34) where $\rho > \rho_3$

$$\psi_4(\rho) = \frac{2D}{\sqrt{|P(\rho)|}} \exp(J) \cos\left[-\int_{\rho_3}^{\rho} P(\rho')dr' - \frac{\pi}{4}\right]. \tag{5.14}$$

Section two the wave function is generated from the connection formula from left hand turning point $\rho_1 < \rho$ (Eq. (A.32)) and right hand turning point $\rho_2 > \rho$ (Eq. (A.34)) have to be equal to one another at a position ρ where $\rho_1 < \rho < \rho_2$ giving

$$\frac{2C}{\sqrt{|P(\rho)|}} \cos\left[\int_{\rho_1}^{\rho} P(\rho')d\rho' - \frac{\pi}{4}\right] = \frac{2D}{\sqrt{|P(\rho)|}} \cos\left[-\int_{\rho_1}^{\rho} P(\rho')dr' - \frac{\pi}{4}\right]. \tag{5.15}$$

Either side of Eq. (5.15) can be used as the wave function of section 2 as long as the following conditions are met. The condition that $D = (-1)^n C$ means that the sign of the constant D on all subsequent wave functions to the right

of section two will have the opposite sign values changed, this is so that the wavefunctions for each section remain the same phase. I now set $C = C_n$ and $D = (-1)^n C_n$ to represent our normalisation constant for a quantum number of a given wavefunction. The WKB approximation produces a piecewise wave function $\psi_{\mathrm{WKB}_n}(\rho)$

$$\psi_{\mathrm{WKB}_n}(\rho) = \begin{cases} \frac{C_n}{\sqrt{|P_n(\rho)|}} \exp\left[\int_{\rho}^{\rho_1} P_n(\rho')d\rho'\right] & \rho < \rho_1 \\ \frac{C_n}{\sqrt{|P_n(\rho)|}} \cos\left[\int_{\rho_1}^{\rho} P_n(\rho')d\rho' - \frac{\pi}{4}\right] & \rho_1 < \rho < \rho_2 \\ \frac{(-1)^n C_n}{\sqrt{|P_n(\rho)|}} \exp\left[-\int_{\rho_2}^{\rho} P_n(\rho')d\rho'\right] & \rho_2 < \rho < \rho_3 \\ \frac{2(-1)^n C_n}{\sqrt{|P_n(\rho)|}} \exp(J_n) \cos\left[-\int_{\rho_3}^{\rho} P_n(\rho')d\rho' - \frac{\pi}{4}\right] & \rho_3 < \rho, \end{cases} \tag{5.16}$$

where

$$J_n = -\int_{\rho_2}^{\rho_3} P_n(\rho)d\rho. \tag{5.17}$$

ρ_1, ρ_2 and ρ_3 are the classical turning points at which $\epsilon = V_{\mathrm{quantum}}(\rho_i)$ where $i = 1, 2, 3$. At the classical turning points $p_n(\rho) = 0$ a singularity in the wave function, $\psi_{\mathrm{WKB}_n}(\rho)$, is produced. The singularity causes spikes in the wave function at these points. The normalization coefficient, C_n, of the wavefunction is evaluated as

$$C_n = \left(\int_{\rho_1}^{\rho_2} \frac{1}{P_n(\rho)} \cos^2\left[\int_{\rho_1}^{\rho} P_n(\rho')d\rho' - \frac{\pi}{4}\right] d\rho\right)^{-\frac{1}{2}}. \tag{5.18}$$

The normalization has been chosen to be done over the width of the well at ϵ_n, as the majority of the quasi-bound wave function's amplitude is within the well.

The integral of the momentum over the width of the well is equal to the energy of a simple harmonic oscillator [27,47,48]

$$\int_{\rho_1}^{\rho_2} P_n(\rho) d\rho = \left(n + \frac{1}{2}\right)\pi, \tag{5.19}$$

where $P_n(\rho) = \sqrt{\epsilon_n - V_{\text{quantum}}(\rho)}$. The WKB approximation energy eigenvalues are given by solving Eq. (5.19) for ϵ_n.

Before I discuss or present the results obtained from the WKB approximation I move onto a numerical analysis utilising the Finite difference method. The purpose of this is so that I can compare and contrast the analytical and numerical results side by side.

5.4 The Electron Monopole Problem in Quantum Mechanical Framework Review

The differences between the classical and the quantum potentials are small and become negligible for high values of $|M|$. At $M = 0$ the greatest divergence between the two potentials happens, as the quantum potential has negative energy values below $\rho \approx 0.1$ while the classical case the potential energy goes to 0.

The analytical WKB method produced a piecewise wavefunction formed from the classically allowed and disallowed regions of the quantum potential. Each of these regions has its own wavefunction that connects to the wavefunction in the preceding or next region. The energy eigenvalues are solved by evaluating Eq. (5.19) which is the same equation as the energy values obtained using the corrected Bohr-Sommerfeld quantisation

Eq. (4.15), the difference being the WKB approximation uses V_{quantum} rather than $V_{\text{classical}}$.

The method for how the finite difference model was applied to the problem can be found in Appendix C.

As will be shown in the Chapter 7 the states found are quasi bound which means that they will decay and scatter in time, but how much time? The next chapter looks at the half lives of these quasi bound states.

Chapter 6

Lifetimes

The quasi-bound states decay after a period of time. In this chapter we look at three different methods of evaluating this time. Firstly we shall use a lifetime derived from the WKB approximation, secondly a lifetime calculated using the finite difference method, and finally a lifetime that was calculated using a phase shift method.

6.1 WKB Lifetimes

The lifetime of a bound state of the electron can be modelled as the particle bounces within the well. Each time the particle hits a well wall, there is a probability that it will tunnel through, with each successive bounce increases that probability. Continually adding these probabilities until the running total reaches a 50% probability that the electron will tunnel through, at which point we can caulate this time as being the half-life of the quasi-bound state. The WKB wave function, Eq. (5.16) and Eq. (5.17), can be utilized to produce

the transmission coefficient C_T being

$$C_T = \frac{|E|^2}{|A|^2}, \tag{6.1}$$

where E is the transmitted amplitude of the wavefunction $\rho_3 > \rho$ and A is the incident amplitude of the wavefunction $\rho_1 < \rho < \rho_2$. The transmitted part of the wavefunction can be expressed as exponentials

$$\psi_{\mathrm{WKB}_n}(\rho) = \frac{(-1)^n A_1}{\sqrt{P_n(\rho)}} \exp(J) \left(\exp\left[i \int_{\rho_3}^{\rho} P_n(\rho) d\rho + \frac{\pi}{4} \right] + \exp\left[-i \int_{\rho_3}^{\rho} P_n(\rho) d\rho - \frac{\pi}{4} \right] \right). \tag{6.2}$$

The amplitudes of the transmitted wavefunction E and the incident wavefunction A can now be written as:

$$E = \frac{(-1)^n C_n}{\sqrt{P_n(\rho)}} \exp(J), \tag{6.3}$$

and

$$A = \frac{C_n}{\sqrt{|P_n(\rho)|}}. \tag{6.4}$$

The transmission coefficient, C_T is

$$C_T = \exp(2J_n) = \exp\left(-2 \int_{\rho_2}^{\rho_3} P_n(\rho) d\rho \right). \tag{6.5}$$

Assuming that the decay follows an exponential decay, a 50% probability of being inside the well is $\frac{1}{2} = \exp\left(-\frac{\tau_{\frac{1}{2}}}{\tau}\right)$, where τ is the lifetime of the quasi-bound state and $\tau_{\frac{1}{2}}$ is the half life. Assuming that this is a classical particle bouncing inside of the the well the time (t), for a single bounce from the potential wall and back again, can be determined from the kinetic energy,

$\epsilon_n = \frac{(\rho_2-\rho_1)^2}{t'^2}$

$$t' = \frac{(\rho_2 - \rho_1)}{\sqrt{\epsilon_n}}. \tag{6.6}$$

Assuming that with each bounce C_T is increased by a factor of itself, until it reaches a value where probability of transmission is 100%. The time taken to perform the adequate number of bounces is τ

$$\tau = t'/C_T, \tag{6.7}$$

with a half-life

$$\tau_{\frac{1}{2}} = \tau \ln 2. \tag{6.8}$$

The half life, $\tau_{\frac{1}{2}}$, is

$$\tau_{\frac{1}{2}} \approx \frac{(\rho_2 - \rho_1)}{\sqrt{\epsilon_n} \exp\left(-2\int_{\rho_2}^{\rho_3} P_n(\rho) d\rho\right)} \ln(2). \tag{6.9}$$

The results of the lifetimes for $\lambda = 100$ and M=-5 to 5 can be seen in Fig. 6.1.

6.2 Finite Difference Lifetimes

For a chosen quasi-bound state the potential can be altered so that the amplitude of the wave function, $\zeta_n(\rho)$, exponentially decays to zero outside the well, see Fig. 6.2. We can create a new wave function, $\Psi(r)$ comprised out of the continuation of eigenfunctions, $\psi_n(\rho)$, mapped onto a chosen state $\zeta_n(\rho)$ such that

$$\Psi(\rho, t) = \sum_{n=0}^{N} C_n \psi_n(\rho) e^{-i\epsilon_n t'}, \quad \text{where} \quad C_n = \langle \zeta(\rho) | \psi_n(\rho) \rangle \tag{6.10}$$

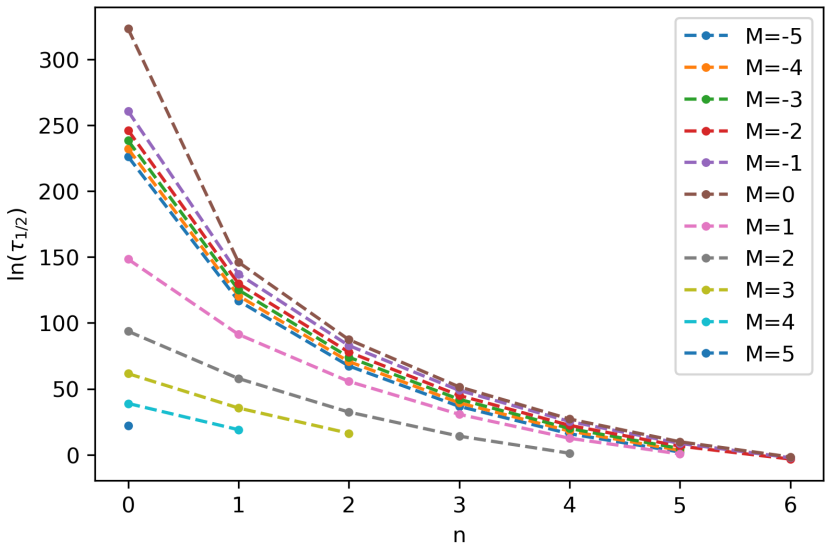

Figure 6.1: $\ln(\tau_{1/2})$ for different values of M for the WKB approximation, $\lambda = 100$. The half-life decreases as the quantum number increases, these states are higher energy and the thickness of the potential wells wall becomes thinner.

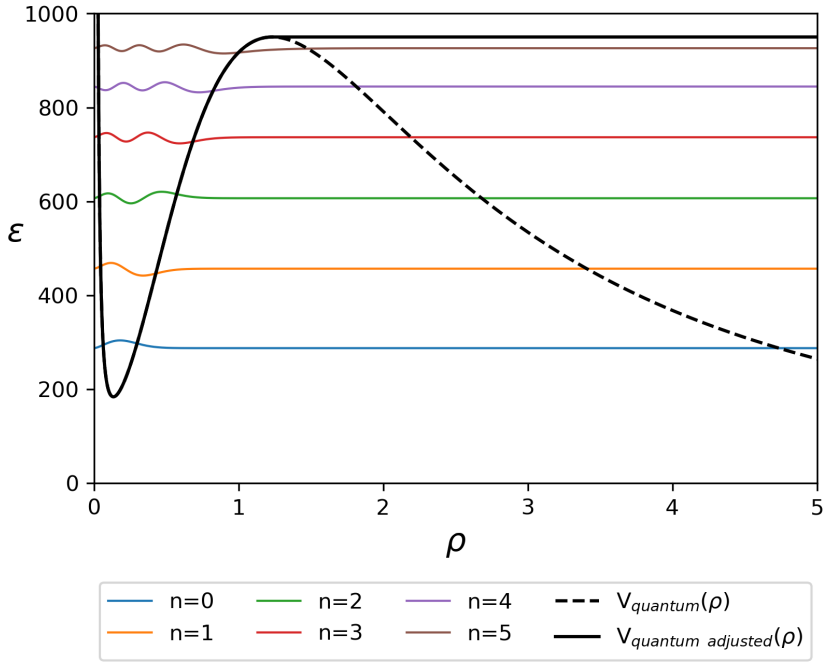

Figure 6.2: The potential, $V_{quantum}(\rho)$ (dashed black line), was adjusted to a new potential, $V_{\text{quantum adjusted}}(\rho)$ (solid black line) leaving the well the same shape but removing the sloping tail. The resulting wave functions $\zeta_n(\rho)$ are now fully bound within the adjusted well. This example is for the values $M = 1$ and $\lambda = 100$.

$\Psi(\rho, t)$ can be evolved through time while calculating the probability that the electron is still within the well. The time when the probability reaches fifty percent can be taken as an estimate of the quasi-bound states half-life, Fig. 6.3.

Increasing the range of ρ and reducing step size, h, both increase the memory requirements required to calculate the results. Increasing the range of ρ allows for the wave function to evolve without reflecting off the boundary and self-interfering within the well. This reduces the accuracy for a given value of h. Reducing h increases the precision of the calculation. The result of these considerations is a balancing act to fully utilise the available computing power to be able to accurately calculate the half-life and fit a curve for the remainder of the decay. This can be seen in Fig. 6.3. The lifetimes calculated via this method are limited to those that do not cause self-interference before a half-life can be evaluated, excluding results with long lifetimes. This can be overcome with more computing power required for longer half-lives.

6.3 Phase Shift Lifetimes

Following the method in [49] Eq. (5.6) can be rewritten in terms of z and $u(z)$, the new position variable $z = \sqrt{\epsilon}\rho$ and the new solution $G(z) = u(z)/\sqrt{z}$ respectively. When $\lambda = 0$ the solution to the monopole problem must return the free electron radial solution Eq. (6.13). When $\lambda = 0$ V(z) reduces to the centrifugal term

$$V(z)_{\lambda=0} = \frac{M^2 - \frac{1}{4}}{z^2}. \tag{6.11}$$

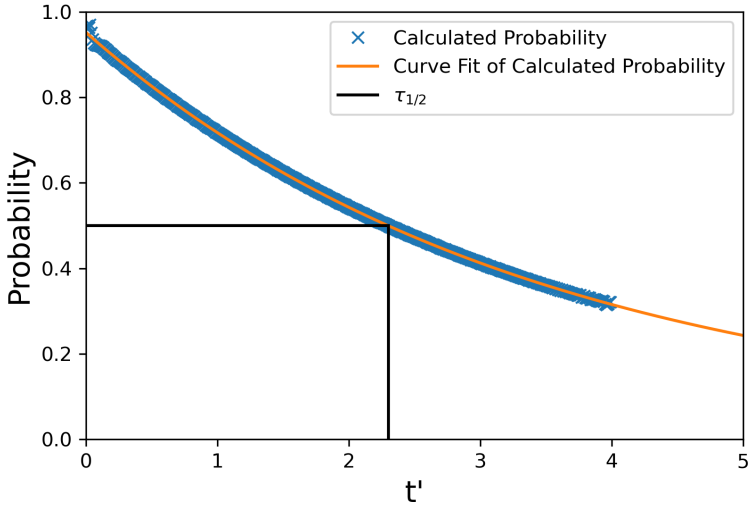

Figure 6.3: The estimated decay in probability of the electron being found within the potential well for $M = 1$ and $\lambda = 100$ and $n = 5$, evaluated with the finite difference method. The equation of the curve in this example is probability of being inside the potential well $\approx 0.921 \exp(-0.293t') + 0.031$. The half-life shown in this plot is $\tau_{1/2} \approx 2.3$. Where $t' = \frac{\omega_c t}{2} = \frac{\hbar t}{2mD^2}$.

This can be rewritten as

$$V(z)_{\lambda=0} = \frac{L(L+1)}{z^2}, \tag{6.12}$$

where the values of L for the above two equations to stay equivalent are: $L = M - \frac{1}{2}$ for $M \geq 0$, $L = -M - \frac{1}{2}$ for $M \leq 0$, and $L = -\frac{1}{2}$ for $M = 0$. The free electron radial solution is

$$u(z) = C(z)\sin(z + \mu(z)), \tag{6.13}$$

where $\mu(z)$ is the variable phase. For $z >> 1$ we obtain

$$u(z) \approx \sqrt{\frac{2}{\pi}} \sin\left(z - L\frac{\pi}{2}\right). \tag{6.14}$$

The Schrödinger equation in terms of $u(z)$ including a magnetic monopole is

$$-\frac{\partial^2 u(z)}{\partial z^2} + (V(z) - 1)u(z) = 0, \tag{6.15}$$

where

$$V(z) = \frac{1}{z^2}\left(-\frac{1}{4} + \left[M + \lambda\left(1 - \frac{1}{\sqrt{1 + \frac{z^2}{\epsilon}}}\right)\right]^2\right). \tag{6.16}$$

The solution to which is

$$u(z) = \sqrt{\frac{2}{\pi}} \sin\left(z - L\frac{\pi}{2} + \delta_L\right), \tag{6.17}$$

where a phase shift, δ_L has to be added due to the presence of the magnetic monopole. At large distances from the monopole, the free electron radial solution should be realised. Comparing Eq. (6.17) and Eq. (6.13) the phase shift can be expressed as

$$\delta_L = L\frac{\pi}{2} + \lim_{z\to\infty} \mu(z). \tag{6.18}$$

Differentiating Eq. (6.13) gives

$$\frac{\partial u(z)}{\partial z} = \frac{\partial C(z)}{\partial z} \sin\left(z + \mu(z)\right) + C(z)\left(1 + \frac{\partial \mu(z)}{\partial z}\right) \cos\left(z + \mu(z)\right). \tag{6.19}$$

The first derivative of $u(z)$ is required to be $\frac{\partial u(z)}{\partial z} = C(z)cos(z + \mu(z))$, as described by [50], for this to be the case with Eq. (6.19) the following must be true

$$\frac{\partial C(z)}{\partial z} \sin\left(z + \mu(z)\right) = -C(z)\frac{\partial \mu(z)}{\partial z} \cos\left(z + \mu(z)\right). \tag{6.20}$$

Taking the second derivative of $u(z)$

$$\frac{\partial^2 u(z)}{\partial z^2} = \frac{\partial C(z)}{\partial z} \cos\left(z + \mu(z)\right) - C(z)\left(1 + \frac{\partial \mu(z)}{\partial z}\right) \sin\left(z + \mu(z)\right). \tag{6.21}$$

Substituting $\frac{\partial C(z)}{\partial z}$ from Eq. (6.20) into Eq. (6.21)

$$\frac{\partial^2 u(z)}{\partial z^2} = -C(z)\frac{\partial \mu(z)}{\partial z}\frac{1}{\sin(z+\mu(z))} - C(z)sin(z+\mu(z)). \tag{6.22}$$

Substituting Eq. (6.22) and Eq. (6.13) into the Schrödinger Equation Eq. (6.15) gives

$$C(z)\frac{\partial \mu(z)}{\partial z}\frac{1}{\sin(z+\mu(z))} + C(z)\sin(z+\mu(z)) + (V(z)-1)C(z)\sin(z+\mu(z)) = 0. \tag{6.23}$$

So,

$$\begin{aligned} \frac{\partial \mu(z)}{\partial z} &= -V(z)\sin(z+\mu(z)), \\ \frac{\partial \mu(z)}{\partial z} &= -\left(-\frac{1}{4} + \left[M + \lambda\left(1 - \frac{1}{\sqrt{1+\frac{z^2}{\lambda\epsilon}}}\right)\right]^2\right)\frac{\sin^2(z+\mu(z))}{z^2}. \end{aligned} \tag{6.24}$$

This allows Eq. (6.18) to be rewritten as

$$\delta_l = L\frac{\pi}{2} + \left.\frac{\partial \mu(z)}{\partial z}\right|_{\infty}. \tag{6.25}$$

Equation Eq. (6.25) cannot be evaluated exactly. Using numerical methods it can be approximated very closely by choosing a sufficiently high value of z. For $\lambda = 0$, we require that $\frac{\partial \mu(z)}{\partial z}$ is approximately equal to $(1-2M)\frac{\pi}{4}$ for $M \geq 0$ and $(1+2M)\frac{\pi}{4}$ for $M \leq 0$. This allows a variety of z-values to be evaluated so the approximation of Eq. (6.24) is adequate, the results of this can be seen in Table 6.1 and Fig. 6.4. In Table 6.1 and Fig. 6.4 the results for negative and positive values of M are the same. This is due to the M^2 term in Eq. (6.24) when $\lambda = 0$.

To solve Eq. (6.24) using the fourth order Runge-Kutta method, see Appendix A.5, the initial conditions need to be known. At $z = 0$ we must have

z	$M=-4$	$M=-3$	$M=-2$	$M=-1$	$M=0$
100	-5.41878629	-3.88335873	-2.33739599	-0.78165724	0.78414519
1000	-5.48991364	-3.92261499	-2.35431984	-0.78502309	0.78527319
2000	-5.49385036	-3.92480292	-2.35525716	-0.78521063	0.78533568
∞	-5.49778714	-3.92699081	-2.35619449	-0.78539816	0.78539816

z	$M=1$	$M=2$	$M=3$	$M=4$
100	-0.78165724	-2.33739599	-3.88335873	-5.41878629
1000	-0.78502309	-2.35431984	-3.92261499	-5.48991364
2000	-0.78521063	-2.35525716	-3.92480292	-5.49385036
∞	-0.78539816	-2.35619449	-3.92699081	-5.49778714

Table 6.1: Tables comparing the values $\mu(z)$ for various M when $\lambda = 0$. The value of $\mu(2000)$ is >99.9% the value of $\mu(\infty)$ for all values of M.

a solution equal to zero, so from Eq. (6.13), $\mu(0) = 0$. If in the limit $z \to 0$ the following is true to remove the singularity at $z = 0$ in Eq. (6.24)

$$\mu(z) = \mu_0 z + O(z^2). \tag{6.26}$$

Then in the limit of $z \to 0$ Eq. (6.24) becomes

$$\mu_0 = -\left(M^2 - \frac{1}{4}\right)(\mu_0 + 1)^2, \tag{6.27}$$

giving the initial conditions required, μ_0, as

$$\mu_0 = \begin{cases} -\frac{M-\frac{1}{2}}{M+\frac{1}{2}} & M \geq 0 \\ -\frac{M+\frac{1}{2}}{M-\frac{1}{2}} & M \leq 0. \end{cases} \tag{6.28}$$

Plotting δ_L against ϵ can be seen in Fig. 6.5. Each step in Fig. 6.5 occurs at an energy eigenvalue, ϵ_n. Determining the line width, Γ, using curve fitting with the equation $\delta_L(\epsilon) = \alpha + \arctan\left(\frac{\epsilon-\epsilon_n}{\Gamma}\right)$, where α is $\delta_L(\epsilon_n)$, the half-life is

$$\tau_{\frac{1}{2}} = \frac{1}{2\Gamma}\ln(2). \tag{6.29}$$

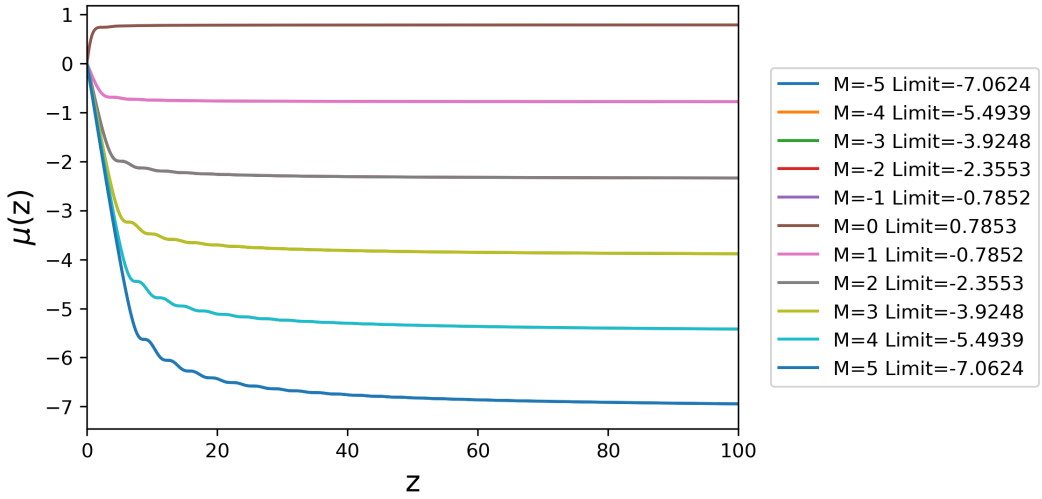

Figure 6.4: Plot showing the dependence of $\mu(z)$ for differing values of M. The behaviour of positive and negative M are identical for all z.

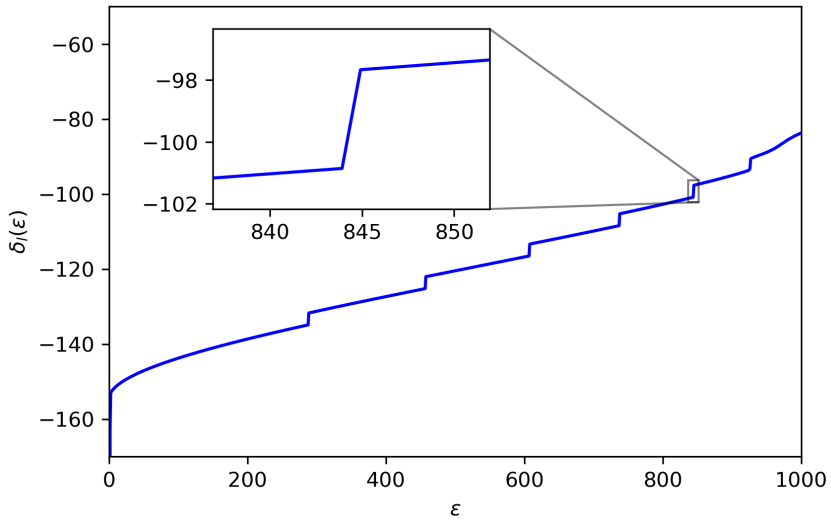

Figure 6.5: The phase shift for $M = 1$ and $\lambda = 100$. The inset plot highlights the jump in the phase shift at a quasi-bound state.

Γ can be seen in the inset of Fig. 6.5 the sharp jump in the phase shift happens at energies where a quasi-bound state is found. The energy of the quasi-bound states agree with those from the finite difference and WKB approximation methods.

6.4 Lifetimes Review

All techniques show that the longest lifetimes are found at the bottom of the potential well and the shortest lifetimes belong to the higher energy electrons. The finite difference method has limitations to the length of the lifetime that can be accurately calculated. The simulation is set within a finite domain and as such any electron that has tunnelled out of the well can bounce off the boundary and tunnel back in again rather than scattering. The WKB and phase shift methods produce results for the longer lifetimes that are expected at the bottom of the potential well. A comparison between the lifetime techniques can only take place over the values that the finite difference method is able to calculate, for that reason only the shortest lived lifetimes are compared between techniques. These techniques can be applied to the various monopole like sources to see what length of lifetimes we could expect experimentally. These results can be found in the next Chapter.

Chapter 7

The Monopole Electron Problem: Results, Discussion and Conclusion

The first results we will look at in this chapter are the energies of the bound states with a comparison between the methods (finite difference, WKB and Bohr-Sommerfeld), and how close was the harmonic oscillator approximation to the actual number of bound states for a given λ. Following this we investigate the minimum monopole charge that would be required to form a single bound state with different values of M. Looking at the different techniques for producing monopoles, will any be of sufficient strength to quasi-bind an electron and what half-life of that state could be expected.

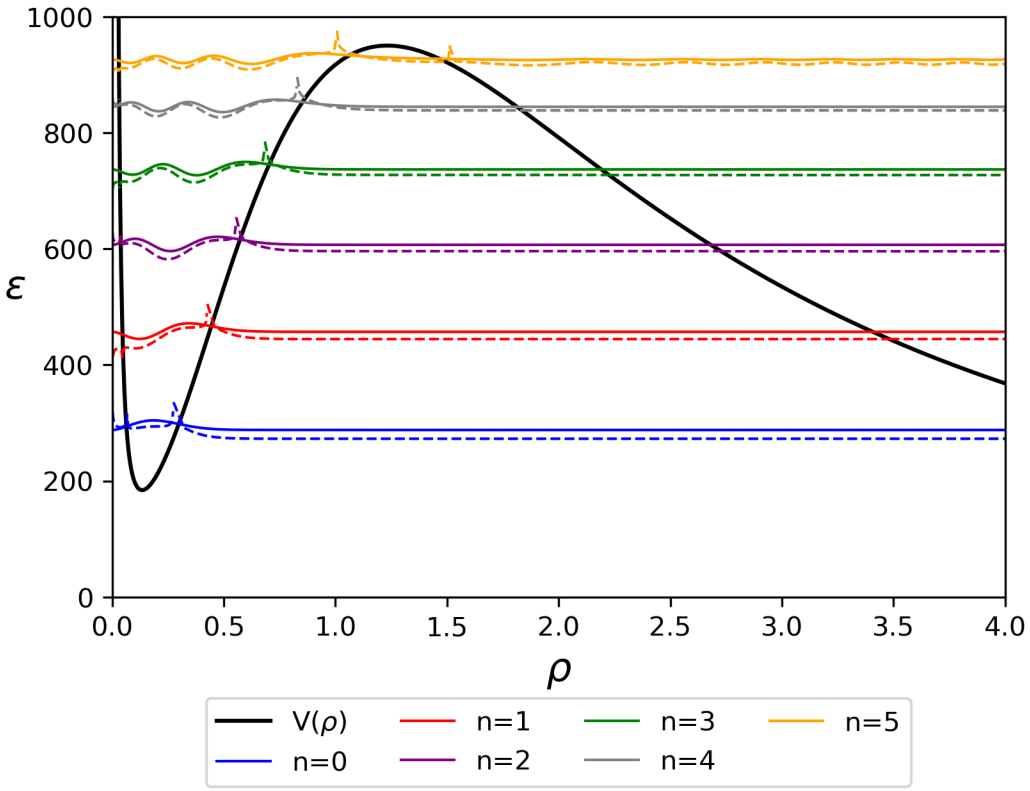

Figure 7.1: The quasi-bound state wave functions calculated numerically with the finite difference method (solid line) and the wave functions derived using the WKB approximation (dashed line). The singularities at the classical turning points are artefacts of the WKB approximation, where $\epsilon = V_{\text{quantum}}(\rho_{1,2})$. The quasi-bound solutions are for $V_{\text{quantum}}(\rho)$ with values of $M = 1$ and $\lambda = 100$ is represented here.

7.1 Binding an Electron to a Magnetic Monopole

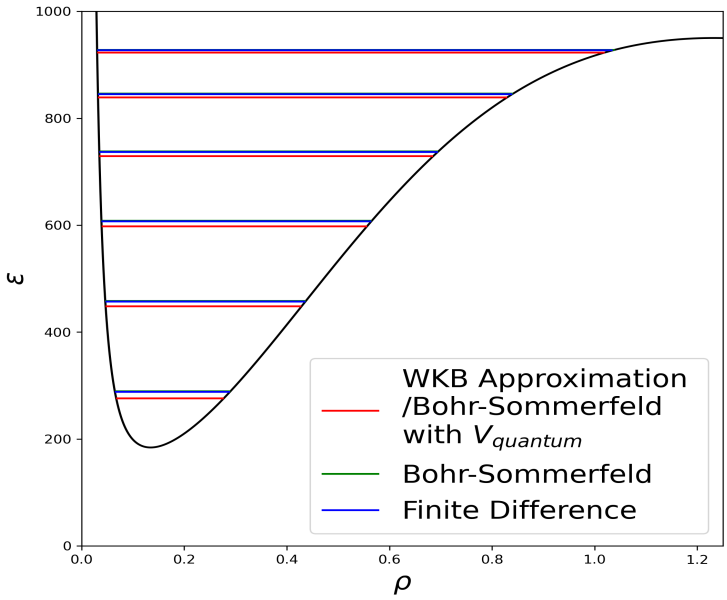

(a)

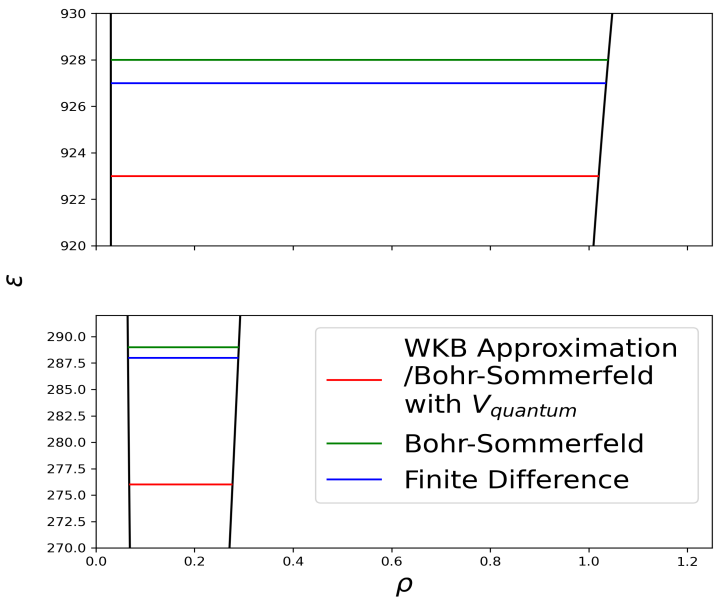

(b)

Figure 7.2: Comparison of eigenvalues for the WKB approximation, Bohr-Sommerfeld quantisation and Finite difference method. (a) The full spectrum of the quasi bound states for $M = 1$ and $\lambda = 100$. (b) Magnified view of the $n = 0$ and $n = 5$ states from (a).

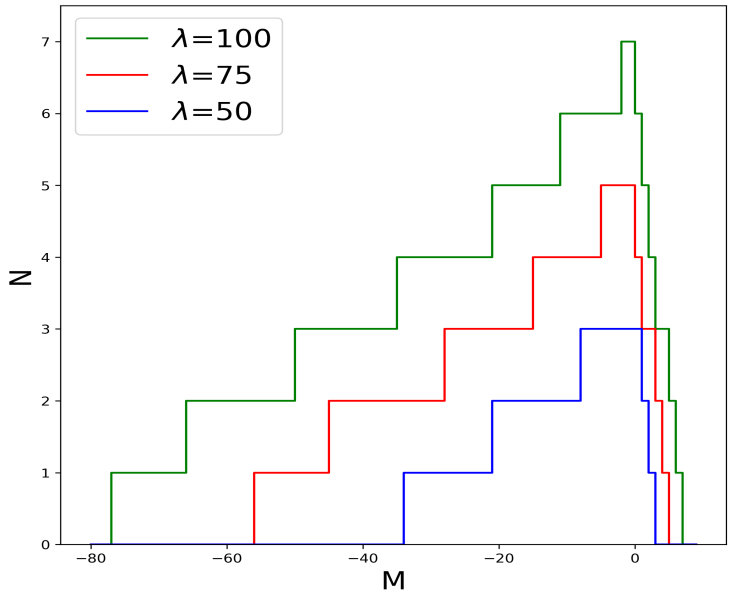

(a)

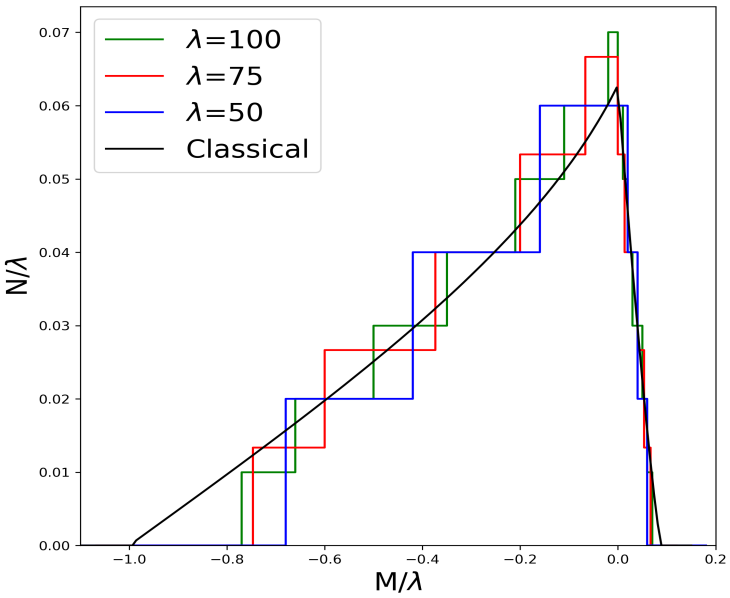

(b)

Figure 7.3: (a) Maximum number of quasi-bound states for different values of λ defined in Eq. (2.7). Evaluated with the finite difference method, the WKB approximation gives very similar results. (b) Number of quasi-bound states and M scaled by λ with the number of states produced by a quantum harmonic oscillator in the classic potential scaled by 4.3λ to equal the total number of quantum states.

In Fig. 7.1 the wave functions depicted only show the quasi-bound states. At the chosen scale, the wave function appears to be zero outside the well, but this is not the case; magnified, this component of the wave function is sinusoidal. This is the case for both methods used. The probability of finding the electron outside the well is always non-zero, so the bound states are, in fact, quasi-bound. The results from the WKB approximation, the Bohr-Sommerfeld quantisation, and the finite difference method become closer with higher quantum numbers. Using $V_{\text{quantum}}(\rho)$ in the Bohr-Sommerfeld quantisation, the energy eigenvalues are closer to the WKB results, as seen in Fig. 7.2.

This is in stark contrast to the classical case where the bound states are permanently bound and there is a continuum of them to be found within the confines of the potential well. A bound state can be formed for any radius in the classical model with a given value of λ and choosing the correct energy. This is not the case for the quantum solution. We find that for large values of negative momentum, where the well is shallow and wide, no quasi-bound states are found.

When a comparison of the number of bound states of the quantum solution with the quantum harmonic oscillator approximation is done, Fig. 7.3b, a similarity in the distribution of states for different values of M. The highest number of bound states for both the quantum harmonic oscillator approximation and finite difference method occurs for $M = 0$. The total number of bound states, $\sum N_M$, that can be found for the quantum solution is given by the area under each graph, which can be written as

$$\sum N_M \approx 0.03\lambda^2. \tag{7.1}$$

As we can see in Eq. (7.1) the number of quasi-bound states are scaled by λ^2. This is the same scaling obtained using the approximation of quantum harmonic oscillators in the classical potential case, Eq. (4.6). The difference is the total number of states generated; classically, M can take any non-integer value, but in the quantum case M is integer, so the number of states that can be found in the quantum mechanical regime is less. The fact that M is an integer causes the stepped plot, Fig. 7.3a, found with the quantum model rather than the smooth slope seen with the classical model, Fig. 4.2. Re-scaling the quantum model so that the total number of quantum bound states, N, by $1/\lambda$, we can see the similarity in the distribution of states in relation to M/λ in Fig. 7.3b.

7.2 Minimum Monopole Charge Required for a single Quasi-Bound State.

There is a value of λ for a given M that will produce a single bound state, any value lower no bound state will be found. Increasing the value of λ more quasi-bound states are found for a chosen value of M. In Fig. 7.4 the value of λ required is less for negative values of M to obtain a quasi-bound state when compared to its positive counterpart. The minimum value of ~$18Q_D$ that will produce a single quasi-bound state is when the angular momentum quantum number is zero, as seen in Fig. 7.4.

Barring the discovery of a magnetic monopole close approximations to one can be found either made by humans or found in nature. Three sources of monopole analogues are magnetic needles, spin-ice, and artificial spin-ice. What would the requirements be for each to realise a bound state?

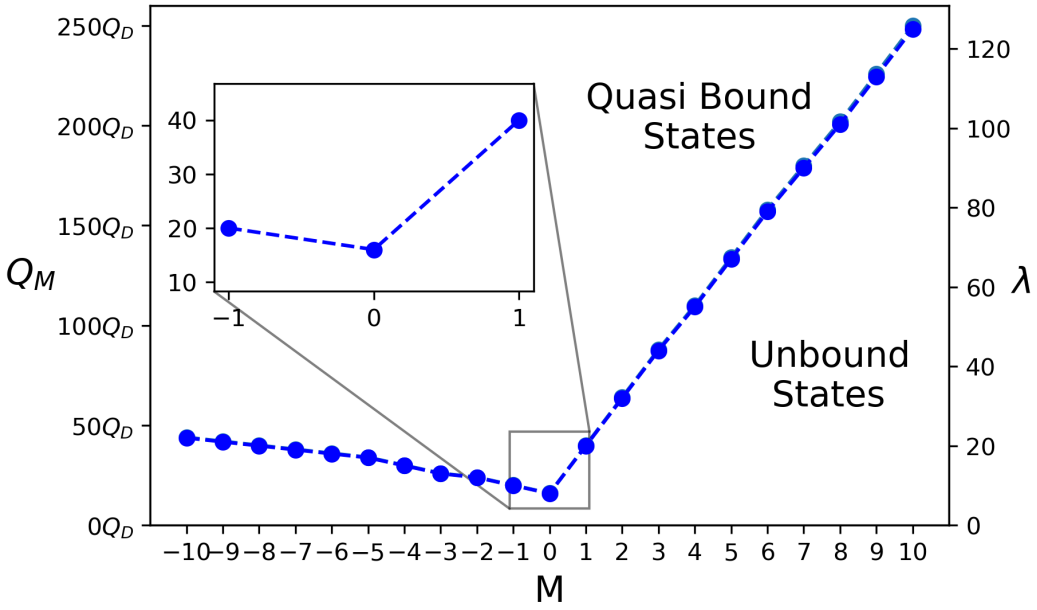

Figure 7.4: Minimum values of λ and Q_m required to produce a single quasi bound state dependent on the angular momentum quantum number, M. Evaluated using the finite difference method, the WKB approximation gives very similar results. The inset plot highlights the minimum value of λ that a quasi-bound state can be found.

7.3 Expected half-life

The minimum monopole charge required for a single quasi-bound electron is $18Q_D$ with the angular momentum quantum number $M = 0$. The dimensionless half-life is $\tau_{1/2} = 1.16$ for the minimum charge required for a quasi-bound state. The half-life in seconds is given by

$$t(D) = \frac{2t' m_e D^2}{\hbar}. \tag{7.2}$$

Using this equation and the distances between monopoles in the various monopole analogues we can make an approximation of lifetimes one might expect.

7.3.1 Magnetic Needle

The magnetic needle in [12] has a magnetic charge of approximately ~$6Q_D$, the needle would have to increase its charge by ~$12Q_D$ to meet the minimum charge required for a bound state with $M = 0$. The tip of the needle can be modelled as a spherical monopole charge with a radius of $100nm$ (the radius of the tip of the needle). At the surface of the sphere, I assume the same magnetic field strength is applied to the needle used to magnetise it, which is ~0.15T. The monopole charge at the needle tip modelled this way is

$$Q_m = \frac{4B\pi r^2}{\mu_0}. \tag{7.3}$$

Reference [12] applied a 0.15T magnetic field to the needle, so $Q_m = 1.909 \times 10^{-8}$Am, assuming the field of the magnetically charged needle matched the field that was applied. A unit of Dirac charge is given by Eq. (2.8), $Q_D = 3.291 \times 10^{-9}$Am. This gives a resulting magnetic needle charge of $\approx 5Q_D$, which is in good agreement with the observed value of ~$6Q_D$. If a magnetic field strength at the tip of the needle can reach a value of ~0.60T then the magnetic charge of the needle tip will be ~$18Q_D$, the threshold to find a quasi-bound state. The aperture radius around the needle tip is approximately $10\mu m$ [12], so if we assume the electron is found at half this distance then the approximate half-life is 5×10^{-7}s for the threshold charge.

7.3.2 Spin-Ice

The charge of a monopole in spin-ice is given by [7]

$$\begin{aligned} Q_m &= \frac{\mu}{\mu_b}\frac{\alpha\lambda_C}{\pi a_d}Q_D, \\ Q_m &\approx \frac{Q_D}{8000}. \end{aligned} \tag{7.4}$$

Here α is the fine structure constant, μ_b is the Bohr magneton, λ_C is the Compton wavelength for an electron, μ is the magnetic permeability, and a_d is the diamond lattice bond length. The required charge of a monopole in spin-ice would need to be 144000 times larger to achieve the minimum charge of $18Q_D$ for a single bound state. In [7] the authors state that the charge of the spin-ice can be tuned by changing the pressure applied to it, causing changes in the value of μ/a_d, if a pressure can be achieved such that

$$\frac{\mu}{a_d} = \frac{18\mu_b\pi}{\alpha\lambda_C}, \tag{7.5}$$

then a spin-ice monopole will be sufficient to form a quasi-bound state for an electron of M=0. The pressures needed are so great that realistically this could not be achieved.

7.3.3 Artificial Spin-Ice

The magnetic charge at any given lattice site is given by [9,10]

$$Q_\alpha = \sum \pm q_i, \tag{7.6}$$

where Q_α is the magnetic charge at the monopole site α and q_i is the charge of a magnetic dipole that is separated by the lattice spacing, where one-half of the dipole is in one lattice site and the other half is in an adjacent lattice site. For the purpose of an example, we assume a square lattice so each lattice site has four charges sitting on it, all of the same magnitude of charge $|q|$. Q_α can take values of $Q_\alpha = \pm 2q$ and $Q_\alpha = \pm 4q$. To reach a value where $Q_\alpha = 18Q_D$ the values of q_i would need to be $q_i = 9Q_D$ for $Q_\alpha = \pm 2q$ and $q_i = 4.5Q_D$ for $Q_\alpha = \pm 4q$. The distance given by [10] range from $100 - 1000nm$ so the lifetimes of the minimum charge in artificial spin ice are in the range $2 - 200 \times 10^{-10}s$.

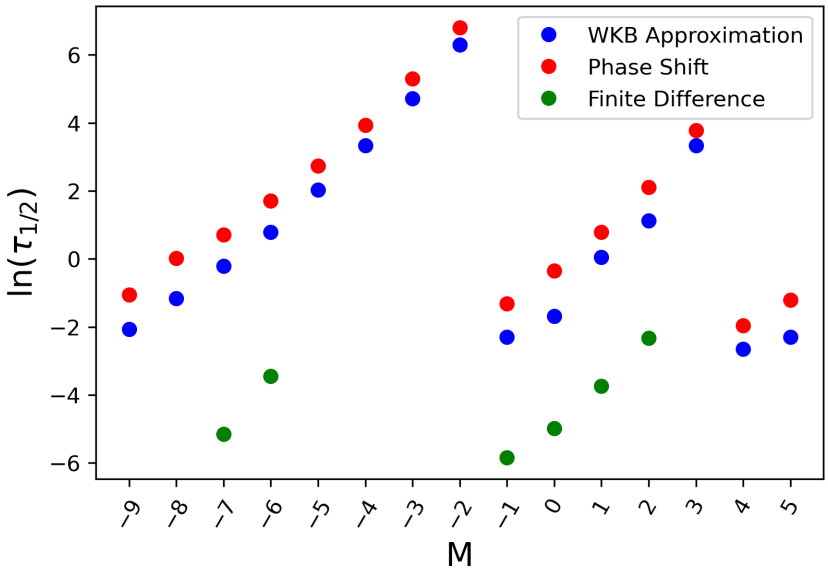

Figure 7.5: Plot of the highest energy bound state half-lives $\ln(\tau_{1/2})$ for $M = -9..5$, where $\lambda = 100$.

7.4 Comparison of Lifetimes from the Different Methods

In Fig. 7.5, we compare the estimates of the lifetimes obtained with three different methods, considering the highest energy quasi-bound states for several values of M and $\lambda = 100$. We can see good agreement between the various methods for the shorter lifetimes. Lifetimes can be very easily computed with the WKB method in contrast to the finite difference and phase-shift methods, for which there are limited results due to the restrictions of the method.

7.5 Conclusion

Classically through the use of Lagrangian mechanics we see four distinct trajectories for an electron. Three trajectories are bound whilst the last type is scattering. A bound orbit is only formed when the electrons energy

is within the potential well for a given value of M/λ, Figs. 3.2a to 3.2c, anywhere outside of this well a scattering orbit is formed. The three types of orbit are dependent on the value of M and λ, Figs. 3.3a to 3.3c, but in each orbit type the motion around the origin located above the magnetic monopole is in the same direction.

The classical solution allows for a continuum of bound states within the potential well, the semi classical and quantum solution do not, Fig. 7.3b. Inside of the potential well there are a finite number of states quantum mechanically, Fig. 7.1, outside of the well we have a continuum of states Fig. C.1. The states that have a non zero component of wavefunction inside the potential well are quasi bound states, these states will eventually tunnel out of the well and form a scattering state , Fig. 6.3 with a half life dependent on quantum number M Fig. 7.5, ϵ and λ.

Future direction for this research is to consider arrangements of magnetic monopoles. Fig. 7.6 is an exploratory attempt I have made in this area, to potentially produce magnetic traps that could be utilised in particle and plasma containment.

Other areas that still require investigation is the effect of spin on these results and would a quasi-bound state of multiple electrons confined in two dimensions be possible?

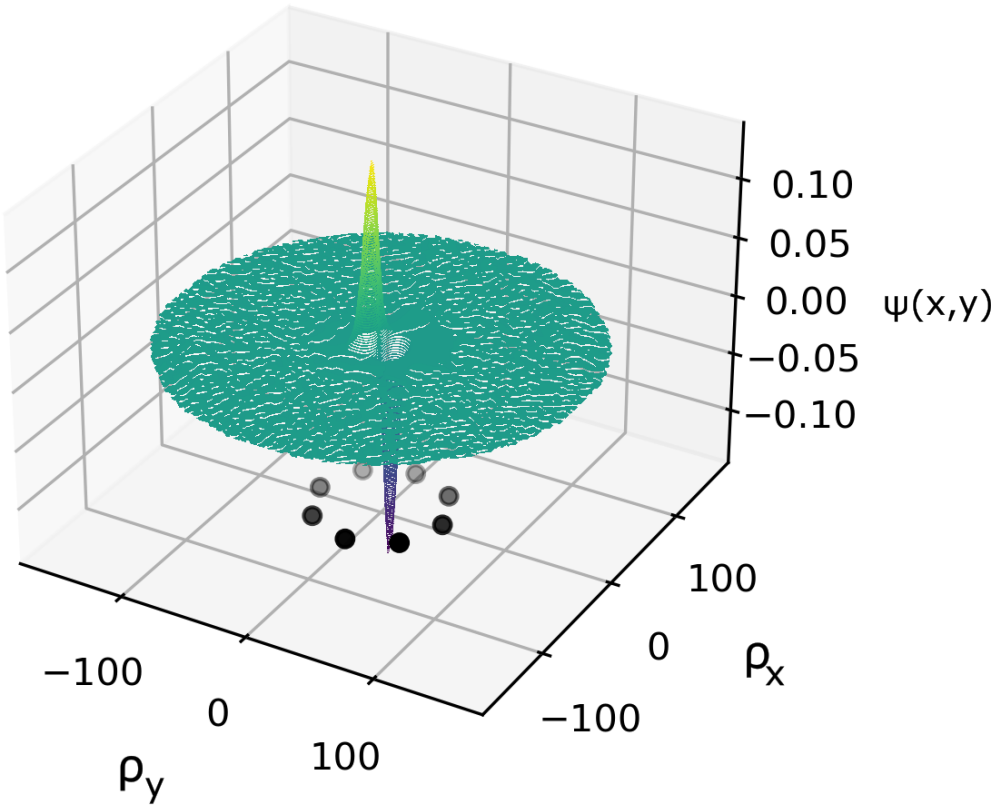

Figure 7.6: Three dimensional wavefunction for an electron's interaction with eight magnetic monopoles with strength $\lambda = 100$ in an circular arrangement (black dots) below the plane. The wavefunction is for quantum number $n = 3$. The colour of the wavefunction is to distinguish between the positive (yellow), negative (purple) and near zero components (green) easier in a three dimensional plot. The wavefunction forms a disk on non-zero amplitude outside of the potential well as seen in the one-dimensional wavefunctions seen earlier as these states are still quasi-bound, the lifetimes of these states of multiple monopoles have not been investigated. Inside the well we see that there are two peaks one positive and one negative as time evolves these peaks rotate around the well, showing that the electron probability density rotates around the centre as time increases.

Chapter 8

Magnetohydrodynamics of an 2D Electron Gas in a Magnetic Field

The aim of this second project is to investigate whether a monopole's magnetic field can be measured using the Hall effect. Since the magnetic field of a monopole is non-uniform the position of the electrons across the plane of a Hall Sensor need to be known. To model this plasma as a fluid we will use magnetohydrodynamics which allows for the interactions of charged particles and magnetic fields to be taken into account which fluid dynamics does not.

Initially we will take a look at the equations of magnetohydrodynamics and the Hall effect. Following on we develop equations of motion for both a uniform magnetic field and non uniform magnetic field. Then we calculate the Hall voltage from the magnetohydrodynamic framework. Finally we develop dimensionless equations of motion and Hall voltage ready for computation.

8.1 An Introduction to Magnetohydrodynamics and the Hall effect

For MHD to be applicable the assumption is made that the characteristic distances are much greater than the mean free path for the electrons (additionally the characteristic time has to be greater than the mean free time but that is not relevant for our derivation as we are looking at a steady state, the velocity of the electron fluid does not change with respect to time) [51]. The self consistent set of equations of Magnetohydrodynamics (MHD) are given by [52–54] as:

$$\text{Continuity Equation} \quad \frac{\partial \rho}{\partial t} + \nabla \cdot (\rho \mathbf{V}) = 0, \tag{8.1}$$

$$\text{Momentum Equation} \quad \rho \left(\frac{\partial}{\partial t} + \mathbf{V} \cdot \nabla \right) \mathbf{V} = \mathbf{J} \times \mathbf{B} - \nabla p, \tag{8.2}$$

$$\text{Amperes Law} \quad \mu_0 \mathbf{J} = \nabla \times \mathbf{B}, \tag{8.3}$$

$$\text{Faraday' Law} \quad \frac{\partial \mathbf{B}}{\partial t} = -\nabla \times \mathbf{E}, \tag{8.4}$$

$$\text{Ohms Law} \quad \mathbf{E} + \mathbf{V} \times \mathbf{B} = \eta \mathbf{J}, \tag{8.5}$$

$$\text{Divergence Constraint} \quad \nabla \cdot \mathbf{B} = 0, \tag{8.6}$$

$$\text{Adiabatic Energy Equation} \quad \frac{d}{dt} \left(\frac{p}{\rho^{\lambda}} \right) = 0. \tag{8.7}$$

Here $\mathbf{B}$ is the magnetic field strength, $\mathbf{V}$ is the plasma velocity, $\mathbf{J}$ is the current density, $\mathbf{E}$ is the electric field vector, ρ is the mass density, p is the plasma pressure, λ is the ratio of specific heats $\lambda = C_P/C_V$, where C_P is the specific heat of the fluid at constant pressure and C_V is the specific heat of the fluid at constant volume), t is time and η is the resistivity. A very extensively modelled MHD problem is that of Hartmann flow, where a plasma flows between two plates with an applied magnetic field and electric field both normal to the velocity as well as to each other [55–57]. Using a similar

model we will investigate the Hall effect, first with uniform magnetic fields and then with non-uniform fields produced by magnetic monopoles. The model will be a mono layer (a material that is a single atom thick such as graphene, often called two dimensional materials) substrate containing a two dimensional electron gas which we will model as a charged fluid using MHD. This will form our sensor plane. One of the most well known two dimensional materials is Graphene, first discovered in 1948 [58] and fully isolated in 2004, using the now famous sticky tape method of graphene production [59]. The other materials that we will investigate as a substrate are Silicon [60], Gallium Arsenide. Silicon and Gallium Arsenide are both semi-conductors that have been extensively used in Hall effect devices.

An electric field is applied in the direction of fluid flow and a magnetic field normal to the surface of the sensor plane, this will produce the conditions necessary to produce the Hall effect. To discuss the Hall effect we need to introduce its cause the Lorentz Force.

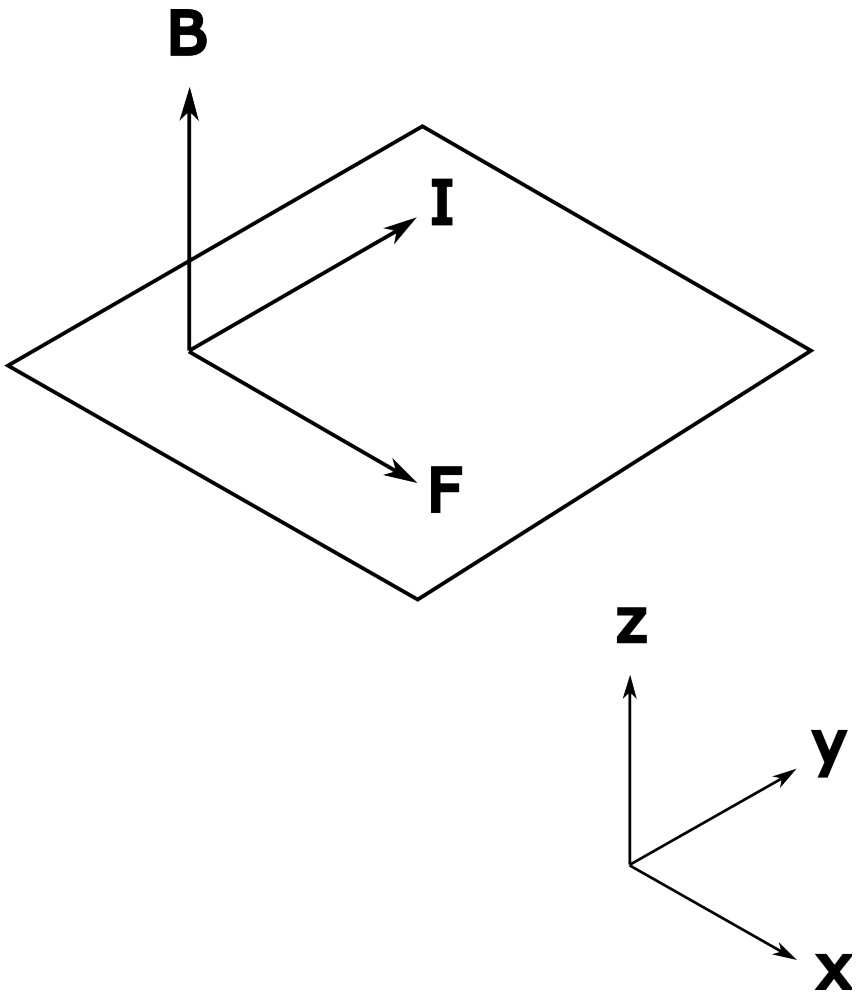

Figure 8.1: The Force felt by a postpositively charged particle particle is in the positive x direction while experiencing a magnetic field perpendicular to is motion in the y direction.

When a current passes through a magnetic field perpendicular to itself it experiences the Lorentz force, [61]

$$\mathbf{F} = q_e(\mathbf{E} + \mathbf{V} \times \mathbf{B}), \tag{8.8}$$

where F is the force acting on a particle with charge $q_e = -1.602 \times 10^{-19}$C. In two dimensions that force, F_x, in the x direction is

$$F_x = q_e \left(E_x - V_y B_z\right), \tag{8.9}$$

as can be seen in Fig. 8.1. In the y direction we have the force, F_y, as

$$F_y = q_e \left(E_y + V_x B_z \right). \tag{8.10}$$

In 1879 Edwin Hall discovered that if a metal plate that has a current applied over it then is placed in a magnetic field of several kilogauss, [62], normal to the surface of the metal plate, then a voltage will form transversely to the current. This is called the Hall effect [63]. The Hall voltage can be easily derived from setting the Lorentz force in the x direction to zero since there cannot be a current travelling in that direction off of the plane. The electric field E_x must oppose any effects produced by $V_y B_z$, [64], so

$$\begin{aligned} 0 &= E_x + V_y B_z, \\ -E_x &= V_y B_z, \\ V_{\mathrm{H}} &= V_y B_z w, \end{aligned} \tag{8.11}$$

where $V_H = -E_x/dx = -E_x/w$ and w is the width of the plane. This can be rewritten in term of R_H and I_y, the Hall coefficient and current in the y direction respectively

$$V_{\mathrm{H}} = \frac{R_{\mathrm{H}} I_y B_z}{T}, \tag{8.12}$$

where $R_{\mathrm{H}} = -1/nq_e$ $\mathrm{m^3C^{-1}}$, $I_y = nq_e v_y wT$ A. T is the thickness of the plane in metres and n is the number density of electrons for a given material per unit volume. The Hall voltage is inversely proportional to the thickness of the sensor plane, but this equation does not work for a two dimensional plane as the Hall voltage approaches infinity as the thickness approaches zero. To evaluate a two dimensional Hall voltage we need to revaluate the current and the Hall coefficient in two dimensions. For two dimensions the Hall coefficient $R_{\mathrm{H2D}} = 1/nq_e$ has units of $\mathrm{m^2C^{-1}}$ and the current is now

the charge flowing through a line segment of the two dimensional plane $I_y = nq_e v_y w$, where n is now chosen as a two dimensional number density of electrons per metre squared. The Hall voltage for a two dimensional electron gas is then

$$V_{\mathrm{HC}} = R_{\mathrm{H2D}} I_y B_z. \tag{8.13}$$

The second issue with Eq. (8.12) is that the relationship becomes more complicated with position dependent magnetic fields, for example the case of a monopole where the magnetic field in the z direction will be dependent on x, y and z positions within the Hall sensor. Removing one of these parameters by utilising a two dimensional sensor so that for a fixed arrangement of monopoles beneath the field at the sensor plane is only dependent on the x and y coordinates see Figs. 8.2a to 8.2d.

Using magnetohydrodynamics I shall look at the behaviour of an electron fluid firstly in uniform magnetic fields with a two dimensional Hall sensor then move on to non-uniform magnetic fields. Exploring what type of results can be expected from actual materials with the same magnetic fields from monopoles as placed in various configurations Figs. 8.2a to 8.2d.

8.2 Equations of Motion for a Two Dimensional Steady State Plasma Flow

To include the Hall effect into the equations of Magnetohydrodynamics a Hall effect term is added into to Ohms Law, Eq. (8.5), [65]

$$\mathbf{E} + \mathbf{V} \times \mathbf{B} - \frac{1}{n_q q} (\mathbf{J} \times \mathbf{B}) = \eta \mathbf{J}, \tag{8.14}$$

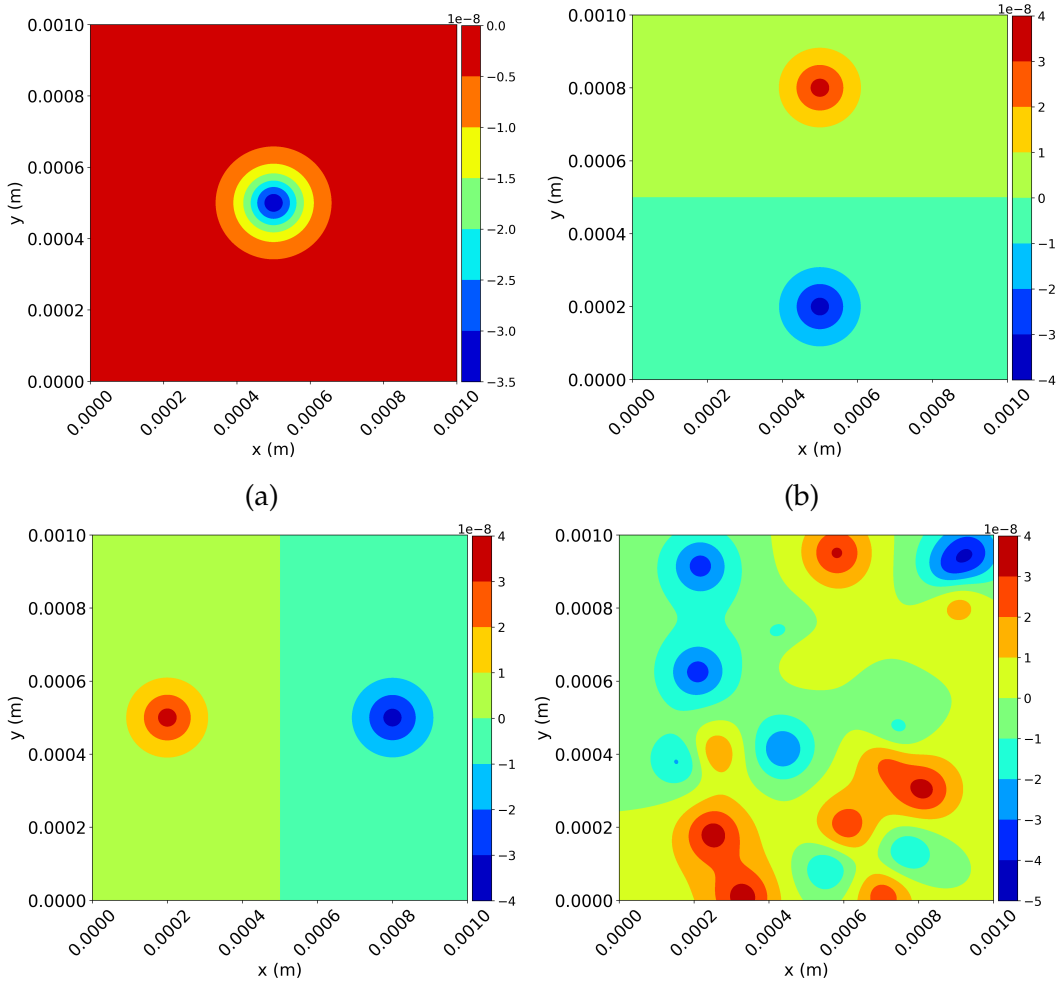

Figure 8.2: The magnetic fields for arrangements of monopoles, the value of the colour bars are in Tesla (a) A single magnetic monopole at the centre of the Hall sensor (b) Two oppositely charged magnetic monopole arranged vertically above one another the lower being a negatively charged Dirac monopole and the upper being a positively charged Dirac monopole, (c) Two oppositely charged magnetic monopoles arranged horizontally from one another the left side is a positively charged Dirac monopole and the right side is a negatively charged Dirac monopole, and (d) Randomly placed Dirac magnetic monopoles of opposite charges but equal in number.

where n_q is the number of charged particles and q is the electric charge of a particle. Rearranging for $\mathbf{J} \times \mathbf{B}$

$$\mathbf{J} \times \mathbf{B} = n_q q(\mathbf{V} \times \mathbf{B} + \mathbf{E} - \eta \mathbf{J}). \tag{8.15}$$

Substituting Eq. (8.15) into the momentum equation, Eq. (8.2) gives

$$\rho \left(\frac{\partial}{\partial t} + \mathbf{V} \cdot \nabla \right) \mathbf{V} = n_q q(\mathbf{V} \times \mathbf{B} + \mathbf{E} - \eta \mathbf{J}) - \nabla p. \tag{8.16}$$

We are looking for a static solution so that any changes to the flow of the plasma with respect to time are equal to zero

$$\rho \left(\mathbf{V} \cdot \nabla \right) \mathbf{V} = n_q q(\mathbf{V} \times \mathbf{B} + \mathbf{E} - \eta \mathbf{J}) - \nabla p. \tag{8.17}$$

Evaluating this as a two dimensional plasma so that velocity is $\mathbf{V} = V_x \mathbf{i} + V_y \mathbf{j}$ and $\mathbf{J} = n_q q \mathbf{V}$ gives

$$\begin{aligned} V_x \frac{\partial V_x}{\partial x}\mathbf{i} + V_y \frac{\partial V_x}{\partial y}\mathbf{i} + V_x \frac{\partial V_y}{\partial x}\mathbf{j} + V_y \frac{\partial V_y}{\partial y}\mathbf{j} = \\ \frac{n_q q}{\rho} \Big(V_y B_z \mathbf{i} - V_x B_z \mathbf{j} + E_y \mathbf{j} \\ - \eta n_q q V_x \mathbf{i} - \eta n_q q V_y \mathbf{j} - \frac{1}{n_q q}\frac{dp}{dx}\mathbf{i} - \frac{1}{n_q q}\frac{dp}{dy}\mathbf{j} \Big). \end{aligned} \tag{8.18}$$

Separating out into the two directions we get the following pair of equations, in the x and y directions respectively:

$$\left(V_x \frac{\partial}{\partial x} + V_y \frac{\partial}{\partial y} \right) V_x = \frac{n_q q}{\rho} \left(V_y B_z - \eta n_q q V_x - \frac{1}{n_q q}\frac{dp}{dx} \right), \tag{8.19}$$

and

$$\left(V_x \frac{\partial}{\partial x} + V_y \frac{\partial}{\partial y} \right) V_y = -\frac{n_q q}{\rho} \left(V_x B_z + E_y - \eta n_q q V_y - \frac{1}{n_q q}\frac{dp}{dy} \right). \tag{8.20}$$

These equations are stationary Burgers' type equations which are derived in fluid dynamics with a viscosity term, ν. In one dimension the stationary Burgers equation for a viscid fluid is

$$u\frac{\partial u}{\partial x} + u\frac{\partial u}{\partial y} = \nu\left(\frac{\partial^2 u}{\partial x^2} + \frac{\partial^2 u}{\partial y^2}\right), \tag{8.21}$$

where u is the fluids velocity as a function of x and y [66, 67]. This means that viscosity of the electron fluid will be very low [68] as the electrons are constantly being scattered by impurities in the material or the structure of the material itself.

The two terms that remain unknown in Eqs. (8.19) and (8.20) are the resistivity, η and the pressure term p. The resistivity, η, is given as [69]

$$\eta = \frac{\mathbf{E}}{\mathbf{j}_c}, \tag{8.22}$$

where $\mathbf{j}_c$ is the current density.

The final part of these equations that needs to be looked at is the pressure term $\frac{1}{\rho}\nabla\cdot P$. There are two sources of pressure within the electron gas, namely the degeneracy pressure, P_d, and the pressure caused by the electrostatic repulsion, P_s, such that $P = P_d(\rho) + P_s(\rho)$. Starting with the degeneracy pressure we have the equation [70, 71]

$$P_d = \frac{\left(3\pi^2\right)^{\frac{2}{3}}\hbar^2}{5m_e}\rho^{\frac{5}{3}}. \tag{8.23}$$

The electrostatic pressure is caused by charges in in the fluid exerting a pressure on neighbouring charges.

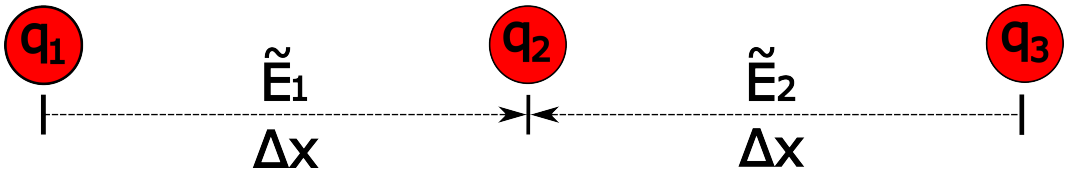

Figure 8.3: The electric field at q_2 is dependent on the electric field produced by the charges either side q_1 and q_3 which are a distance of Δx from q_2.

Fig. 8.3 shows a charge, q_2, flanked either side by charges q_1 and q_2. The central charge q_2 has an electric field at its location dependent on the strengths and distances of the two charges either side of it q_1 and q_3. We assume that each of these charges are comprised of an integer number, n_q, of electron charges, q_e, such that $q_m = n_{qm} q_e$. The electric fields at q_2 in the x direction can be calculated as

$$E_x = E_{1x} + E_{2x} = \frac{q_1 - q_3}{\epsilon_0 4\pi \Delta x^2}, \tag{8.24}$$

derived from Maxwell's equation. Rewriting $\mathbf{E}$ in terms of number density then in terms of mass density using $\rho = m_e n_q/(\Delta x \Delta y)$, where Δy is the distance between two charges in the y direction

$$E_x = -\frac{q_e \left(n_{q3} - n_{q1}\right)}{\epsilon_0 4\pi \Delta x^2} = -\frac{q_e \left(\rho_3 - \rho_1\right) \Delta y}{m_e \epsilon_0 4\pi \Delta x}. \tag{8.25}$$

The force experienced by q_2 is then

$$F_x = n_{q2} q_e E_x = -\frac{n_{q2} q_e^2 \left(\rho_3 - \rho_1\right) \Delta y}{m_e 4\pi \Delta x} = -\frac{\rho_2 q_e^2 \left(\rho_3 - \rho_1\right) \Delta y^2}{m_e^2 \epsilon_0 4\pi}. \tag{8.26}$$

The shear pressure in the x direction caused by F_x is then given by

$$P_{sx} = -\frac{F_x}{\Delta x \Delta y} = -\frac{\rho_2 q_e^2 \left(\rho_3 - \rho_1\right) \Delta y}{m_e^2 \epsilon_0 4\pi \Delta x}. \tag{8.27}$$

A similar derivation can be performed for the shear pressure in the y di-

rection, where the charges are aligned in the y direction rather than the x direction

$$P_{sy} = -\frac{\rho_2 q_e^2 (\rho_3 - \rho_1) \Delta x}{m_e^2 \epsilon_0 4\pi \Delta y}. \tag{8.28}$$

The next step is to take the derivative of the pressure term. Since the central difference approximation is

$$f'(x) = \frac{f(x+h) - f(x-h)}{2h}, \tag{8.29}$$

so the derivative of ρ in the x direction is

$$\frac{\partial \rho}{\partial x} = \frac{\rho_3 - \rho_1}{2\Delta x}, \tag{8.30}$$

and in the y direction

$$\frac{\partial \rho}{\partial y} = \frac{\rho_3 - \rho_1}{2\Delta y}. \tag{8.31}$$

Eq. (8.30) can be substituted into Eq. (8.27) and Eq. (8.31) substituted into Eq. (8.28). We can now evaluate ∇P as a combination of the degeneracy and static pressures in the two directions

$$\nabla P = \left[\frac{\left(3\pi^2\right)^{\frac{2}{3}} \hbar^2}{5 m_e \rho} \frac{\partial}{\partial x} \rho^{\frac{5}{3}} - \frac{\rho q_e^2 \Delta y}{m_e^2 \epsilon_0 2\pi} \frac{\partial \rho}{\partial x} \right] \mathbf{i} + \left[\frac{\left(3\pi^2\right)^{\frac{2}{3}} \hbar^2}{5 m_e \rho} \frac{\partial}{\partial y} \rho^{\frac{5}{3}} - \frac{\rho q_e^2 \Delta x}{m_e^2 \epsilon_0 2\pi} \frac{\partial \rho}{\partial y} \right] \mathbf{j}. \tag{8.32}$$

Evaluating the constants of the degeneracy pressure and the static pressure terms within the acceleration term. In the x direction we get:

$$\frac{1}{\rho} \frac{\partial P_d}{\partial x} \approx 2.33 \times 10^{-38} \frac{1}{\rho} \frac{\partial \rho^{\frac{5}{3}}}{\partial x}, \tag{8.33}$$

$$\frac{1}{\rho} \frac{\partial P_{sx}}{\partial x} \approx 5.56 \times 10^{32} \Delta y \frac{\partial \rho}{\partial x}. \tag{8.34}$$

Comparing Eq. (8.33) and Eq. (8.34) we see that $\frac{1}{\rho} \frac{\partial \rho^{\frac{5}{3}}}{\partial x}$ would need to be ap-

proximately seventy orders of magnitude greater than $\Delta y \frac{\partial \rho}{\partial x}$ to put both of these sources of acceleration on equal footing. This shows that any acceleration due to degeneracy pressure is negligible. We can now rewrite our acceleration term due to pressure as

$$\frac{1}{\rho}\nabla P = -\frac{q_e^2 \Delta y}{m_e^2 \epsilon_0 2\pi}\frac{\partial \rho}{\partial x}\mathbf{i} - \frac{q_e^2 \Delta x}{m_e^2 \epsilon_0 2\pi}\frac{\partial \rho}{\partial y}\mathbf{j}. \tag{8.35}$$

Substituting Eq. (8.35) into Eqs. (8.19) and (8.20), we get the following equations of motion in the x and y directions:

$$\left(V_x \frac{\partial}{\partial x} + V_y \frac{\partial}{\partial y}\right) V_x = \frac{n_q q}{\rho}\left(V_y B_z - \eta n_q q V_x - \frac{1}{n_q q}\frac{\rho q^2 \Delta y}{m_e^2 \epsilon_0 2\pi}\frac{\partial \rho}{\partial x}\right), \tag{8.36}$$

and

$$\left(V_x \frac{\partial}{\partial x} + V_y \frac{\partial}{\partial y}\right) V_y = \frac{n_q q}{\rho}\left(-V_x B_z + E_y - \eta n_q q V_y - \frac{1}{n_q q}\frac{\rho q^2 \Delta x}{m_e^2 \epsilon_0 2\pi}\frac{\partial \rho}{\partial y}\right). \tag{8.37}$$

The final equation that we will require is the continuity equation, Eq. (8.1). For a steady state there is no change in the mass density of the fluid in time so $\frac{\partial \rho}{\partial t} = 0$ giving the steady state continuity equation, Eq. (8.1), as

$$\nabla \cdot (\rho \mathbf{V}) = 0. \tag{8.38}$$

Expanding Eq. (8.38) gives

$$\rho \frac{\partial V_x}{\partial x} + \rho \frac{\partial V_y}{\partial y} + V_x \frac{\partial \rho}{\partial x} + V_y \frac{\partial \rho}{\partial y} = 0. \tag{8.39}$$

8.3 Non Uniform Magnetic Fields from Magnetic Monopoles

Name	Derivative Form	Integral Form
Gauss' Law	$\nabla \cdot \mathbf{E} = \frac{q_\rho}{\epsilon_0}$	$\int \mathbf{E} \cdot d\mathbf{A} = \iiint \frac{\rho}{\epsilon_0} dV$
Gauss' law for magnetism	$\nabla \cdot \mathbf{B} = 0$	$\int \mathbf{B} \cdot d\mathbf{A} = 0$
Faraday law	$\nabla \times \mathbf{E} = -\frac{\partial \mathbf{B}}{\partial t}$	$\oint \mathbf{E} \cdot d\mathbf{l} = -\int \frac{\partial \mathbf{B}}{\partial t} \cdot d\mathbf{A}$
Ampères law	$\nabla \times \mathbf{B} = \mu_0 \mathbf{J} + \mu_0 \epsilon_0 \frac{\partial \mathbf{E}}{\partial t}$	$\oint_C \mathbf{B} \cdot d\mathbf{l} = \mu_0 \left(I + \epsilon_0 \int_s \frac{\partial \mathbf{E}}{\partial t} . d\mathbf{A} \right)$

Table 8.1: The Maxwell equations in derivative and integral forms [26, 72], where q_ρ is the electrical charge density, q is the enclosed electrical charge, I is current, the permeability of free space $\mu_0 = 1.257 \times 10^{-6}$ NA^{-2} and the permittivity of free space $\epsilon_0 = 8.854 \times 10^{-12}$ Fm^{-1}.

In a non uniform magnetic field, produced by a magnetic monopoles distributed under the plane, the magnitude will be position dependent so will take the form $\mathbf{B}(x, y)$ on our two dimensional plane. The specific type of non dimensional field we will investigate is produced by a magnetic monopole, which is analogous to the electric field produced by an electrically charged particle.

The electric field of a charged particle in spherical coordinates can be evaluated using the integral form of the Gauss' Law, this gives an electric field equation

$$\mathbf{E}(R) = \frac{q}{\epsilon_0 4\pi R^2} \hat{R}, \tag{8.40}$$

where R is the radial distance away from the charged particle. The magnetic field for a magnetically charged particle can be evaluated in the same manner but with a slight change to the no monopole law or Faraday Law producing an integrable version $\oint \mathbf{B} \cdot d\mathbf{A} = Q_m \mu_0$, which allows magnetic monopoles, [24, 25]. This new Faraday law can be solved in spherical coordinates giving the result Eq. (2.2).

Looking ahead to solving this equation via a two dimensional finite difference method, we need to evaluate the magnetic field present at any two dimensional element of the charged fluid, Fig. 8.4. The electron fluid travelling across the two dimensional plane will only feel any force that occurs in the z direction. Evaluating the Lorentz force at any given point of the fluid

$$\mathbf{F} = q\,(\mathbf{V} \times \mathbf{B}) = (V_y B_z - V_z B_y)\hat{i} + (V_z B_x - V_x B_z)\hat{j} + (V_x B_y - V_y B_x)\hat{k}. \quad (8.41)$$

The electrons have $V_z = 0$ and are confined to the two dimensional plane. They cannot be accelerated in the z direction which implies that $B_y = B_x = 0$ leaving the Lorentz force as

$$\mathbf{F} = V_y B_z \hat{i} - V_x B_z \hat{j}. \quad (8.42)$$

Thus the only part of the magnetic field that the charged fluid would interact with is

$$\mathbf{B} = 0\hat{i} + 0\hat{j} + B_z \hat{k}. \quad (8.43)$$

Using Pythagoras we see that that R is equal to

$$R(x, y) = \sqrt{D^2 + r^2} = \sqrt{D^2 + (x - x_m)^2 + (y - y_m)^2}, \quad (8.44)$$

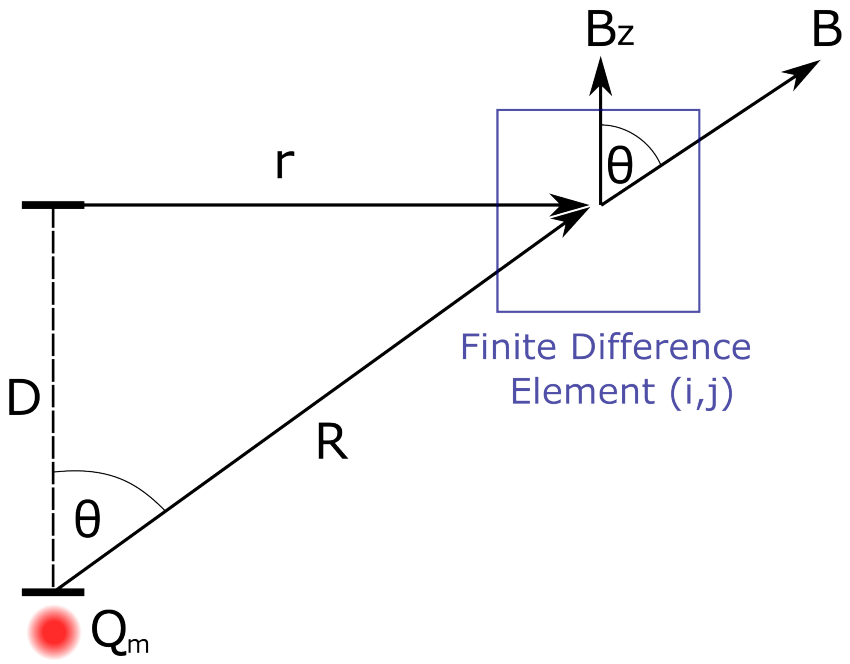

Figure 8.4: Diagram of the magnetic field acting upon a two dimensional element of charged fluid laying in the x, y plane. r is the radial distance from the plane above the monopole to the centre of the element, D is the distance between the monopole and the plane, R is the distance between the monopole and the element, B is the magnetic field at the element in the direction of $\hat{R}$ and B_z is the magnetic field in the direction perpendicular to the plane with a Cartesian coordinates system of x, y).

where x, y is the position of an electron and x_m, y_m are the coordinates of the magnetic monopole. We also note that:

$$\cos(\theta) = \frac{B_z}{B}, \tag{8.45}$$

and

$$\cos(\theta) = \frac{D}{R}. \tag{8.46}$$

Setting Eq. (8.45) equal to Eq. (8.46) and then applying a small amount of algebra we return

$$B_z(x, y) = \frac{BD}{R(x, y)} = \frac{Q_m D \mu_0}{4\pi R(x, y)^3}. \tag{8.47}$$

We can rewrite our equations of motion but now using the position dependent magnetic field. Since the magnetic field from each monopole is additive at each point on the plane we get the equations of motion for a two dimensional plasma interacting with monopoles as:

$$\left(V_x \frac{\partial}{\partial x} + V_y \frac{\partial}{\partial y}\right) V_x = \frac{n_q q}{\rho} \left(V_y \sum B_z(x, y) - \eta n_q q V_x - \frac{1}{n_q q} \frac{\rho q^2 \Delta y}{m_e^2 \epsilon_0 2\pi} \frac{\partial \rho}{\partial x}\right), \tag{8.48}$$

and

$$\left(V_x \frac{\partial}{\partial x} + V_y \frac{\partial}{\partial y}\right) V_y = \frac{n_q q}{\rho} \left(-V_x \sum B_z(x, y) + E_y - \eta n_q q V_y - \frac{1}{n_q q} \frac{\rho q^2 \Delta x}{m_e^2 \epsilon_0 2\pi} \frac{\partial \rho}{\partial y}\right). \tag{8.49}$$

8.4 Hall Voltage from MHD

The Classic Hall voltage is given as

$$V_{\mathrm{HC}} = v_y B_z w, \tag{8.50}$$

where w is the width of the plane that the Hall voltage is being measured. This is easily derived form the Lorentz Force equation and setting the Force equal to zero in the x direction, as was seen in the introduction. I shall recreate this but utilising the equations of motion derived previously, namely the Burgers type equation in the x direction

The force on the fluid is set to zero by the addition of an electric force that opposes it, E_x. This can be broken down into two components one electric field to oppose the Lorentz force, E_x^b, and another to oppose the the force generated by the electrostatic repulsion between electrons, E_x^a.

$$\left(V_x\frac{\partial}{\partial x}+V_y\frac{\partial}{\partial y}\right)V_x=\frac{n_q q}{\rho}\left(B_z V_y-\eta n_q q V_x-\frac{1}{n_q q}\frac{\rho q^2\Delta y}{m_e^2\epsilon_0 2\pi}\frac{\partial\rho}{\partial x}+E_x^a-E_x^b\right). \tag{8.51}$$

The opposing forces of electric fields, E_x^a and E_x^b, and the Lorentz and electrostatic cancel each other, then there can be no movement of the charged particles in the x direction, so we can set $v_x = 0$ in this scenario. The alternative way of viewing this is that there is no current in the x direction across the plane so this can be achieved by having no charged particles or no velocity in the x direction; since the fluid is comprised of charged particles then $\tilde{V}_x = 0$ has to be true. This gives the following equation

$$0=n_q q V_y B_z-\frac{\rho q^2\Delta y}{m_e^2\epsilon_0 2\pi}\frac{\partial\rho}{\partial x}+n_q q E_x^a-n_q q E_x^b, \tag{8.52}$$

moving the E_x^a term to the right

$$-n_q q E_x^a=n_q q V_y B_z-\frac{\rho q^2\Delta y}{m_e^2\epsilon_0 2\pi}\frac{\partial\rho}{\partial x}-n_q q E_x^b. \tag{8.53}$$

Since $-\int E dx = -E\Delta x = V$ (where V is voltage)

$$n_q q V_{\text{HMHD}} = -\left(n_q q V_y B_z - \frac{\rho q^2 \Delta y}{m_e^2 \epsilon_0 2\pi} \frac{\partial \rho}{\partial x} - n_q q E_x^b \right) \Delta x. \tag{8.54}$$

When the fluid has reached a steady state forces produced by the magnetic field and that of the pressure are equal the $V_{\text{HMHD}} = V_{\text{HC}}$ this can be achieved by choosing $-E_x^b w = V_{\text{HC}} = V_y B_z \Delta x$ so

$$V_{\text{HMHD}} = -\frac{1}{n_q q} \left(2 n_q q V_y B_z - \frac{\rho q^2 \Delta y}{m_e^2 \epsilon_0 2\pi} \frac{\partial \rho}{\partial x} \right) \Delta x, \tag{8.55}$$

this can be expressed in terms of the current as

$$V_{\text{HMHD}} = R_{\text{H}} \left(\frac{2 I_y B_z}{T} - \frac{\rho q^2 A}{m_e^2 \epsilon_0 2\pi} \frac{\partial \rho}{\partial x} \right), \tag{8.56}$$

where I_y is the current in the y direction. For a two dimensional Hall sensor plane we need to utilise the two dimensional Hall coefficient R_{H2D}

$$V_{\text{HMHD}} = R_{\text{H2D}} \left(2 I_y B_z - \frac{\rho q^2 A}{m_e^2 \epsilon_0 2\pi} \frac{\partial \rho}{\partial x} \right). \tag{8.57}$$

The Hall coefficient for both the classical and magnetohydrodynamic Hall voltage remains the same, $R_{\text{H}} = -1/n_q q$ m^3C^{-1} for the three dimensional Hall sensor and $R_{\text{H2D}} = -1/n_q q$ m^2C^{-1} for a two dimensional Hall sensor.

8.5 Characteristic Equations of Motion and Hall Voltage

Choosing the parameters:

$$\mathbf{V} = U\tilde{\mathbf{V}}, \quad x = L\tilde{x}, \quad y = L\tilde{y}, \quad \text{and} \quad \rho = \xi\tilde{\rho}. \tag{8.58}$$

U is the scaling parameter for the dimensionless velocity $\tilde{\mathbf{V}}$, L is the scaling parameter for the dimensionless distance $\tilde{x}$ and $\tilde{y}$ and ξ is the scaling parameter for the dimensionless variable $\tilde{\rho}$. Substituting these variables into the static solution Eq. (8.17) gives

$$\frac{\xi U^2}{L}\tilde{\rho}\left(\tilde{\mathbf{V}}\cdot\tilde{\nabla}\right)\tilde{\mathbf{V}} = n_q q\mathbf{E} + n_q q U\tilde{\mathbf{V}}\times\mathbf{B} - \eta n_q^2 q^2 U\tilde{\mathbf{V}} - \frac{1}{L}\tilde{\nabla}p. \tag{8.59}$$

Rearranging gives

$$\left(\tilde{\mathbf{V}}\cdot\tilde{\nabla}\right)\tilde{\mathbf{V}} = \frac{1}{\tilde{\rho}}\left[\frac{n_q q L}{\xi U^2}\mathbf{E} + \frac{n_q q L}{\xi U}\tilde{\mathbf{V}}\times\mathbf{B} - \frac{n_q^2 q^2 L\eta}{\xi U}\tilde{\mathbf{V}} - \frac{1}{\xi U^2}\tilde{\nabla}p\right]. \tag{8.60}$$

Separating this out into the two directions gives in the x direction

$$\left(\tilde{V}_x\frac{\partial}{\partial\tilde{x}} + \tilde{V}_y\frac{\partial}{\partial\tilde{y}}\right)\tilde{V}_x = \frac{1}{\tilde{\rho}}\left[\frac{n_q q L B_z}{\xi U}\tilde{V}_y - \frac{n_q^2 q^2 L\eta}{\xi U^2}\tilde{V}_x - \frac{1}{\xi U}\frac{\partial}{\partial\tilde{x}}p\right], \tag{8.61}$$

and in the y direction

$$\left(\tilde{V}_x\frac{\partial}{\partial\tilde{x}} + \tilde{V}_y\frac{\partial}{\partial\tilde{y}}\right)\tilde{V}_y = \frac{1}{\tilde{\rho}}\left[\frac{n_q q L}{\xi U^2}E_y - \frac{n_q q L B_z}{\xi U}\tilde{V}_x - \frac{n_q^2 q^2 L\eta}{\xi U}\tilde{V}_y - \frac{1}{\xi U^2}\frac{\partial}{\partial\tilde{y}}p\right]. \tag{8.62}$$

Choosing

$$L = \frac{\xi U^2}{qE_y}, \tag{8.63}$$

this choice is made due to the applied electric field in the y direction is constant for any given simulation and will only accelerate the fluid in the y direction. This then enables the E_y term to be scaled to 1. Substituting L into the other terms gives the following equation of motion in the x direction

$$\left(\tilde{V}_x\frac{\partial}{\partial\tilde{x}}+\tilde{V}_y\frac{\partial}{\partial\tilde{y}}\right)\tilde{V}_x=\frac{1}{\tilde{\rho}}\left[\frac{n_qUB_z}{E_y}\tilde{V}_y-\frac{n_q^2qU\eta}{E_y}\tilde{V}_x-\frac{1}{\xi U^2}\frac{\partial}{\partial\tilde{x}}p\right], \tag{8.64}$$

in the y direction the equation of motion becomes

$$\left(\tilde{V}_x\frac{\partial}{\partial\tilde{x}}+\tilde{V}_y\frac{\partial}{\partial\tilde{y}}\right)\tilde{V}_y=\frac{1}{\tilde{\rho}}\left[n_q-\frac{n_qUB_z}{E_y}\tilde{V}_x-\frac{n_q^2qU\eta}{E_y}\tilde{V}_y-\frac{1}{\xi U^2}\frac{\partial}{\partial\tilde{y}}p\right]. \tag{8.65}$$

Substituting in the pressure term from the static repulsion with the relevant scale lengths for the mass density applied gives for the x direction

$$\left(\tilde{V}_x\frac{\partial}{\partial\tilde{x}}+\tilde{V}_y\frac{\partial}{\partial\tilde{y}}\right)\tilde{V}_x=\frac{1}{\tilde{\rho}}\left[\frac{n_qUB_z}{E_y}\tilde{V}_y-\frac{n_q^2qU\eta}{E_y}\tilde{V}_x\right]-\frac{1}{U^2}\frac{q^2\Delta x\xi}{m_e^2\epsilon_0 2\pi}\frac{\partial\tilde{\rho}}{\partial\tilde{x}}, \tag{8.66}$$

and in the y direction

$$\left(\tilde{V}_x\frac{\partial}{\partial\tilde{x}}+\tilde{V}_y\frac{\partial}{\partial\tilde{y}}\right)\tilde{V}_y=\frac{1}{\tilde{\rho}}\left[n_q-\frac{n_qUB_z}{E_y}\tilde{V}_x-\frac{n_q^2qU\eta}{E_y}\tilde{V}_y\right]-\frac{1}{U^2}\frac{q^2\Delta y\xi}{m_e^2\epsilon_0 2\pi}\frac{\partial\tilde{\rho}}{\partial\tilde{y}}. \tag{8.67}$$

Going back to the definition of the dimensionless mass density $\rho = \xi\tilde{\rho}$, assuming the fluid is only made up of the charged particles such that the total number of particles in the fluid is equal to n_q then we can say that mass density $\rho = n_q * m_q/A$, where we have chosen area, A, as opposed to volume due to the fluid being treated as 2 dimensional and m_q is the mass of the charged particle. The dimensionless equation for mass density

becomes

$$\frac{n_q m_q}{A} = \xi\tilde{\rho}. \tag{8.68}$$

Rearranging we get

$$n_q = \frac{A\xi}{m_q}\tilde{\rho}. \tag{8.69}$$

On the left side we now have a dimensionless quantity, to achieve the same on the right side the scaling parameter has to be $\xi = m_q/A$ giving the result of

$$\tilde{\rho} = n_q. \tag{8.70}$$

Applying this to the equations of motion, in the x direction

$$\left(\tilde{V}_x\frac{\partial}{\partial\tilde{x}} + \tilde{V}_y\frac{\partial}{\partial\tilde{y}}\right)\tilde{V}_x = \frac{UB_z}{E_y}\tilde{V}_y - \frac{\tilde{\rho}qU\eta}{E_y}\tilde{V}_x - \frac{1}{U^2}\frac{q^2\Delta x\xi}{m_e^2\epsilon_0 2\pi}\frac{\partial\tilde{\rho}}{\partial\tilde{x}}, \tag{8.71}$$

and in the y direction

$$\left(\tilde{V}_x\frac{\partial}{\partial\tilde{x}} + \tilde{V}_y\frac{\partial}{\partial\tilde{y}}\right)\tilde{V}_y = 1 - \frac{UB_z}{E_y}\tilde{V}_x - \frac{\tilde{\rho}qU\eta}{E_y}\tilde{V}_y - \frac{1}{U^2}\frac{q^2\Delta y\xi}{m_e^2\epsilon_0 2\pi}\frac{\partial\tilde{\rho}}{\partial\tilde{y}}. \tag{8.72}$$

Choosing the following parameters and updating the length scaler with the definition of ξ:

$$\begin{aligned}
\beta &= \frac{UB_z}{E_y},\\
\gamma &= \frac{qU\eta}{E_y},\\
\alpha_x &= \frac{1}{U^2}\frac{q^2\Delta y\xi}{m_e^2\epsilon_0 2\pi},\\
\alpha_y &= \frac{1}{U^2}\frac{q^2\Delta x\xi}{m_e^2\epsilon_0 2\pi},\\
L &= \frac{m_e U^2}{\Delta x\Delta y q E_y}\ \text{m}.
\end{aligned} \tag{8.73}$$

We have the final characteristic equations of motion:

$$\left(\tilde{V}_x\frac{\partial}{\partial\tilde{x}}+\tilde{V}_y\frac{\partial}{\partial\tilde{y}}\right)\tilde{V}_x=\beta\tilde{V}_y-\tilde{\rho}\gamma\tilde{V}_x-\alpha_x\frac{\partial\tilde{\rho}}{\partial\tilde{x}}, \tag{8.74}$$

and

$$\left(\tilde{V}_x\frac{\partial}{\partial\tilde{x}}+\tilde{V}_y\frac{\partial}{\partial\tilde{y}}\right)\tilde{V}_y=1-\beta\tilde{V}_x-\tilde{\rho}\gamma\tilde{V}_y-\alpha_y\frac{\partial\tilde{\rho}}{\partial\tilde{y}}, \tag{8.75}$$

in the x and y directions respectively. These scaling factors apply also for a non uniform field where the value of β becomes position dependent as B_z is potion dependent so for magnetic monopoles we have in the x direction

$$\left(\tilde{V}_x\frac{\partial}{\partial\tilde{x}}+\tilde{V}_y\frac{\partial}{\partial\tilde{y}}\right)\tilde{V}_x=\sum\beta(x,y)\tilde{V}_y-\tilde{\rho}\gamma\tilde{V}_x-\alpha_x\frac{\partial\tilde{\rho}}{\partial\tilde{x}}, \tag{8.76}$$

and in the y direction

$$\left(\tilde{V}_x\frac{\partial}{\partial\tilde{x}}+\tilde{V}_y\frac{\partial}{\partial\tilde{y}}\right)\tilde{V}_y=1-\sum\beta(x,y)\tilde{V}_x-\tilde{\rho}\gamma\tilde{V}_y-\alpha_y\frac{\partial\tilde{\rho}}{\partial\tilde{y}}. \tag{8.77}$$

The dimensionless Hall voltage, $\tilde{V}_{\mathrm{HMHD}}$, that is derived from Eq. (8.74) in the same manner as previously for the dimensional version gives

$$\tilde{V}_{\mathrm{HMHD}}=\left(2\beta\tilde{V}_y-\alpha_x\frac{\partial\rho}{\partial\tilde{x}}\right)\Delta\tilde{x}. \tag{8.78}$$

The scaling factor for the Hall voltage can be derived form the classical Hall voltage equation. Using Eqs. (8.58) and (8.73) we can substitute into the classical Hall effect equation

$$V_{\mathrm{HC}}=\tilde{V}_x\tilde{B}_zE_yL\Delta\tilde{x}. \tag{8.79}$$

Now choosing

$$\tilde{V}_{\mathrm{HC}}=\frac{V_{\mathrm{HC}}}{LE_y}, \tag{8.80}$$

where $\tilde{V}_{\mathrm{HC}}$ is the dimensionless Hall voltage, the denominator LE_y has units of Volts as does the numerator. $\tilde{V}_{\mathrm{HC}}$ can now be expressed as

$$\tilde{V}_{\mathrm{HC}} = \tilde{V}_x \tilde{B}_z \Delta\tilde{x}. \tag{8.81}$$

This will now allow the transformation of the dimensionless Hall voltages into results with dimensions. Finally we can simply rewrite the continuity equation Eq. (8.39) in terms of the dimensionless parameters

$$\tilde{\rho}\frac{\partial\tilde{V}_x}{\partial\tilde{x}} + \tilde{\rho}\frac{\partial\tilde{V}_y}{\partial\tilde{y}} + \tilde{V}_x\frac{\partial\tilde{\rho}}{\partial\tilde{x}} + \tilde{V}_y\frac{\partial\tilde{\rho}}{\partial\tilde{y}} = 0. \tag{8.82}$$

8.6 Summary and Outlook

I have developed equations of motion for the electron gas in both a uniform magnetic field and also monopole magnetic fields. The Hall voltage has been derived from the equations of motion and takes into account the additional factor of the internal pressure of the electron gas. The characteristic equations of motion and Hall voltage are created for generating solutions. The next chapter we will look at how to solve the equations of motion across the Hall sensor plane and generate the corresponding Hall voltages.

Chapter 9

Two Dimensional Finite Difference Method and Solutions

In this chapter we look at how we can get solutions for the equations of motion and build a picture of how the electron gas flows across the plane and what the corresponding Hall voltage distribution in uniform and non-uniform magnetic fields. Following I move onto modelling two dimensional materials as the Hall sensor plane and see what effect they have on the Hall voltage. Finally different monopole distributions are modelled across the Hall sensor plane which correspond to the magnetic fields seen in Fig. 8.2.

9.1 Solving the Momentum and Continuity Equations via Finite Differences

To solve the equations of motion a two dimensional finite differences method has been chosen, which will enable the equations to be discretized across the

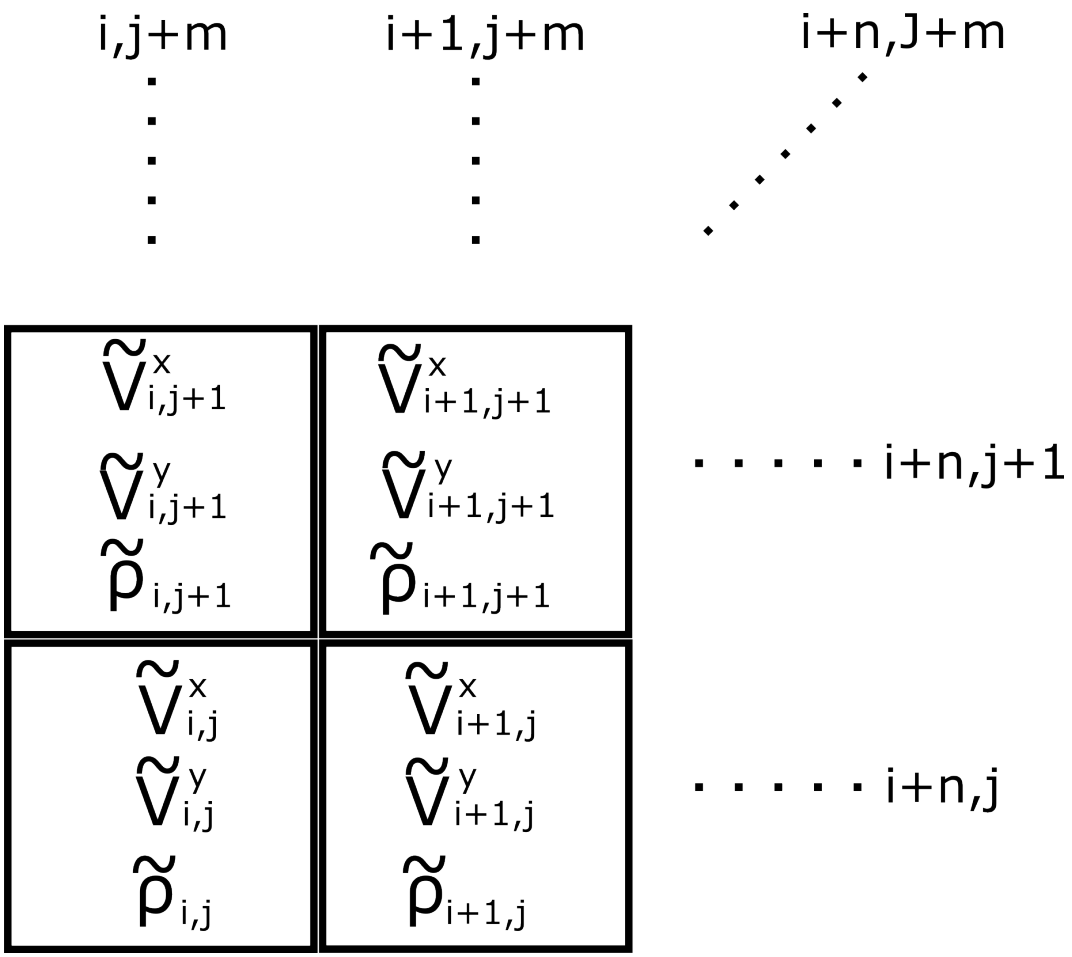

Figure 9.1: A diagrammatic representation of the two dimensional finite difference method layout. The initial element in the lower left has an index of i, j subsequent elements have indexes of $i + n, j + m$. Since each fluid element once discretised has its own address then the mass density and velocity's can be addressed appropriately. The finite difference method will allow the calculation of the next row of elements building up a complete data set of velocities and mass density over the plane at each element.

plane and form two dimensional arrays containing values of the velocity and number density of the electron fluid at all points over the sensor plane [73,74]. The finite differences method involves dividing the plane of the Hall sensor up into a grid of elements. The aim is to calculate the value of velocity and number of electrons at each element. Each element has its own unique address which is denoted by the row number i and the column number j. Since we are going to be using the central finite difference method the grid will extend two elements past the edges of the plane. This is so boundary

and initial conditions can be implemented. At the elements extending past the plane in the x direction there is no fluid so the velocity will be equal to 0 and the number of electrons will also be zero and these will not change value during any calculations. For the elements extending below the plane these will populated with the initial conditions of the fluid.

Since we have the first two rows of the elements chosen with starting values for velocity and electron number density the task is to calculate the row the comes next, then repeat until the end of the grid.

Discretising the equations of motion using the finite differences shown in Eqs. (A.40) and (A.41). The notation used is: $V^x_{i,j}$ where in this example we are representing a velocity, the superscript is the direction in which the vector is pointing, if this is not present then there is no direction applicable. The subscript is the element grid coordinates, i is the x coordinate and j is the y coordinate. Discretising the equation of motion in the x direction Eq. (8.74) gives

$$\tilde{V}^x_{i,j}\frac{\tilde{V}^x_{i+1,j}-\tilde{V}^x_{i-1,j}}{2\Delta\tilde{x}}+\tilde{V}^y_{i,j}\frac{\tilde{V}^x_{i,j+1}-\tilde{V}^x_{i,j-1}}{2\Delta\tilde{y}}= \beta_z\tilde{V}^y_{i,j}-\alpha\frac{\tilde{\rho}_{i+1,j}-\tilde{\rho}_{i-1,j}}{2\Delta\tilde{x}}-\tilde{\rho}_{i,j}\gamma\tilde{V}^x_{i,j}, \quad (9.1)$$

where Δx and Δy are the lengths of any given element in the x and y directions respectively. The same process is repeated but this time for the equation of motion in the $\tilde{y}$ direction Eq. (8.75)

$$\tilde{V}^x_{i,j}\frac{\tilde{V}^y_{i+1,j}-\tilde{V}^y_{i-1,j}}{2\Delta\tilde{x}}+\tilde{V}^y_{i,j}\frac{\tilde{V}^y_{i,j+1}-\tilde{V}^y_{i,j-1}}{2\Delta\tilde{y}}= 1-\beta_z\tilde{V}^x_{i,j}-\alpha\frac{\tilde{\rho}_{i,j+1}-\tilde{\rho}_{i,j-1}}{2\Delta\tilde{y}}-\tilde{\rho}_{i,j}\gamma\tilde{V}^y_{i,j}. \quad (9.2)$$

Finally for the continuity equation Eq. (8.82)

$$\tilde{\rho}_{i,j}\frac{\tilde{V}^x_{i+1,j}-\tilde{V}^x_{i-1,j}}{2\Delta\tilde{x}}+\tilde{\rho}\frac{\tilde{V}^y_{i,j+1}-\tilde{V}^y_{i,j-1}}{2\Delta\tilde{y}}+ \\ \tilde{V}^x_{i,j}\frac{\tilde{\rho}_{i+1,j}-\tilde{\rho}_{i-1,j}}{2\Delta\tilde{x}}+\tilde{V}^y_{i,j}\frac{\tilde{\rho}_{i,j+1}-\tilde{\rho}_{i,j-1}}{2\Delta\tilde{y}}=0. \quad (9.3)$$

Rearranging so that we have an equation that gives us the required velocity and number density in the next element in the y direction, so we get for $\tilde{V}^x_{i,j+1}$

$$\tilde{V}^x_{i,j+1}=\frac{2\Delta\tilde{y}}{\tilde{V}^y_{i,j}}\left(\beta\tilde{V}^y_{i,j}-\alpha\frac{\tilde{\rho}_{i+1,j}-\tilde{\rho}_{i-1,j}}{2\Delta\tilde{x}}- \\ \tilde{V}^x_{i,j}\frac{\tilde{V}^x_{i+1,j}-\tilde{V}^x_{i-1,j}}{2\Delta\tilde{x}}-\tilde{\rho}_{i,j}\gamma\tilde{V}^x_{i,j}\right)+\tilde{V}^x_{i,j-1}. \quad (9.4)$$

$\tilde{V}^y_{i,j+1}$ in the next element in the y direction is

$$\tilde{V}^y_{i,j+1}=\frac{2\Delta\tilde{y}}{\tilde{V}^y_{i,j}}\left(1-\beta\tilde{V}^x_{i,j}-\alpha\frac{\tilde{\rho}_{i,j+1}-\tilde{\rho}_{i,j-1}}{2\Delta\tilde{y}}- \\ \tilde{V}^x_{i,j}\frac{\tilde{V}^y_{i+1,j}-\tilde{V}^y_{i-1,j}}{2\Delta\tilde{x}}-\tilde{\rho}_{i,j}\gamma\tilde{V}^y_{i,j}\right)+\tilde{V}^y_{i,j-1}. \quad (9.5)$$

$\tilde{\rho}_{i,j+1}$ in the next element in the y direction is

$$\tilde{\rho}_{i,j+1}=\tilde{\rho}_{i,j-1}-\frac{2\Delta\tilde{y}}{\tilde{V}^y_{i,j}}\left(\tilde{\rho}_{i,j}\left[\frac{\tilde{V}^x_{i+1,j}-\tilde{V}^x_{i-1,j}}{2\Delta\tilde{x}}+\frac{\tilde{V}^y_{i,j+1}-\tilde{V}^y_{i,j-1}}{2\Delta\tilde{y}}\right]+ \\ \tilde{V}^x_{i,j}\frac{\tilde{\rho}_{i+1,j}-\tilde{\rho}_{i-1,j}}{2\Delta\tilde{x}}\right). \quad (9.6)$$

Moving along the elements of a row until all the velocities and mass density of the next row have been calculated, we can then move up a row and repeat the process until the entire grid has been updated with the required

velocity's and electron number density. This excludes the elements that are to the left and right of the Hall sensor plane as these remain at zero for all values forming the boundary conditions.

The finite difference method is applied to Eqs. (8.50) and (8.78). The classical Hall voltage calculated for each row of elements in the plane

$$\tilde{V}_{HC}(j) = \sum_{i=0}^{n} \tilde{V}_{i,j}^{y} \beta_{i,j} \Delta\tilde{x}. \tag{9.7}$$

Then the magnetohydrodynamic Hall voltage per row of elements is calculated as

$$\tilde{V}_{\mathrm{HMHD}}(j) = \sum_{i=0}^{n} \left(2\tilde{V}_{i,j}^{y} \beta_{i,j} - \alpha \frac{\tilde{\rho}_{i+1,j} - \tilde{\rho}_{i-1,j}}{2\Delta\tilde{x}} \right) \Delta\tilde{x}. \tag{9.8}$$

The equations generated for the finite difference method only take into account interaction cells that are $i \pm 1$ and $j \pm 1$, this means that long range interactions are not taken into account. Any perturbations caused by interactions with the elements that are diagonally positioned, $(i+1, j+1)$, $(i+1, j-1)$, $(i-1, j+1)$, $(i-1, j-1)$, from the element, (i, j) that we are interested in, are not included in the simulation.

9.2 Applying the Finite Difference method for a Uniform Magnetic Field

The first consideration when applying the finite difference method is the boundary conditions along the edges of the Hall sensor plane parallel to the y axis. The choice for $\tilde{\rho}$ is that outside the boundary the mass density of the fluid has to be zero, this ensures that no mass from beyond the plane can affect the fluid on the plane. The next condition is at the boundary $\tilde{V}_x = 0$ as no fluid can travel through the boundary either exiting or entering the

Hall sensor plane. For a fluid that contains ions such as water a no slip boundary condition would be used to conserve the continuity [75–80] up to that boundary. A no slip condition is the requirement that if the boundary is not moving then the fluid that is in contact across that boundary should also have the same velocity as it, so $\tilde{V}_y = 0$. The simulations start with the same initial conditions: initial velocity, $\tilde{V}_{y0}$ and initial mass density $\tilde{\rho}_0$. The mass density and initial velocity starts uniformly distributed, as we move up the plane the mass density decreases as the fluid is accelerated by the applied electric field E_y. This can be seen in Fig. 9.2a. When there is no magnetic field the edge effects of the no slip boundary condition can be seen, the mass density moves away from the edges of the plane. When a magnetic field is applied there is a movement of mass density to the left for a negative magnetic field, Fig. 9.2b. While the no slip condition works for fluids that are experiencing friction with a physical boundary restricting the fluid motion, we wish to model a two dimensional electron gas within a material.

For an electron gas it will not be constrained using a boundary that causes drag on the electron fluid, so a slip condition on the boundary would be better to model. For a slip condition at the boundary we remove the requirement that $\tilde{V}_y = 0$. This allows at the boundary, a non-zero velocity in the y direction. This produces no changes in either the x or y velocity over the plane. The mass density of the electron fluid remains constant across the plane and no Hall voltage is produced, as we would expect from an absence of magnetic field. From this point on all modelling will be with the slip condition on the boundary.

Now applying a magnetic field for a region we can observe what happens to an electron fluid on entering the magnetic field and also on exiting the magnetic field. An electron fluid flowing through a uniform magnetic field

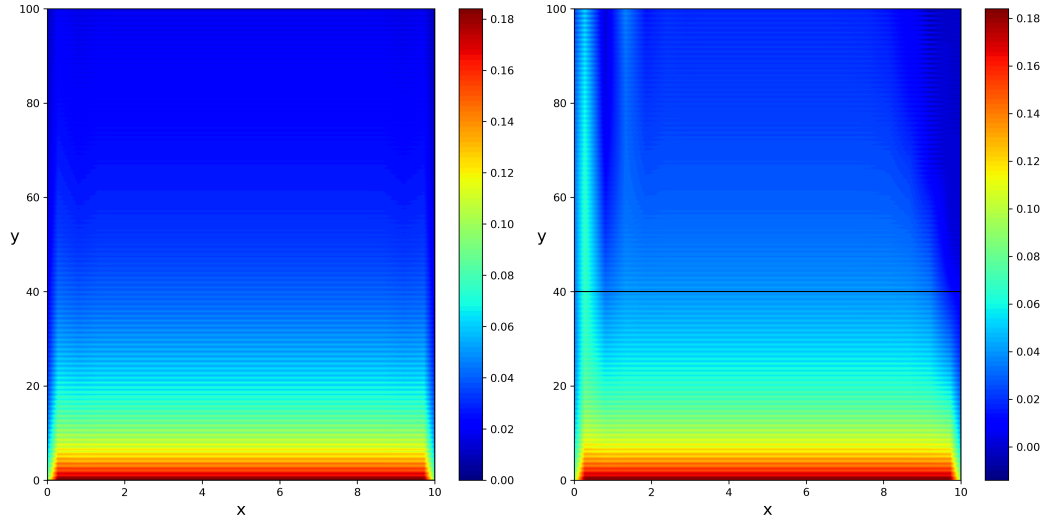

(a) (b)

Figure 9.2: The mass density of the the fluid with no slip boundary conditions (a) No applied magnetic field. Initial conditions and variables are $\tilde{B}_z = 0$, $\tilde{V}_{y0} = 7$, $\tilde{\rho}_0 = 0.2$, $\tilde{\eta} = 0.001$, $\tilde{P} = 0.01$, (b) applied magnetic field between $y = 0$ to 40. Initial conditions and variables are $\tilde{B}_z = -0.001$, $\tilde{y}_0 = 7$, $\tilde{\rho}_0 = 0.2$, $\tilde{\eta} = 0.001$, $\tilde{P} = 0.01$.

will see it mass pushed towards one side, dependent on the direction of the magnetic field. Fig. 9.3a shows that a negative field pushes the mass of the fluid towards the left of the sensor plane. The fluid is pushed towards the right and side of the sensor plane for a positive magnetic field, Fig. 9.3b. In both of these cases we see an initial fluctuation of the mass density when entering the magnetic field and once again on exiting the magnetic region. The fluctuation dies off allowing for a mass density that does not change as we move further up the sensor panel. Within the magnetic field this results in a balance being struck between Lorentz force from the magnetic field acting upon the fluid and the internal pressure force of the plasma that is caused by the build up of negative charge on one side of the plane. On exiting the magnetic region the mass density homogenises across the width of the plane. Since no magnetic field is present here the only force driving this change is the internal pressure of the charged fluid which is dependent on the differential of mass density, so works to once again homogenise the

mass density of the plasma.

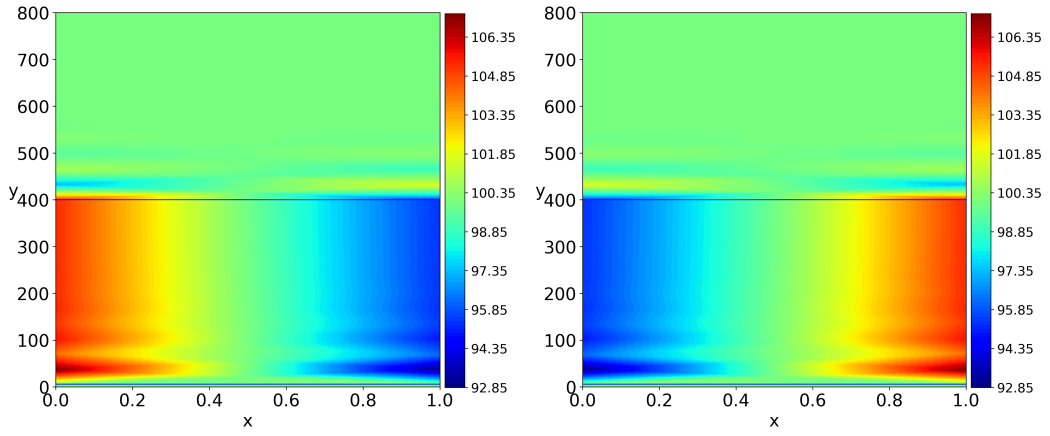

(a) (b)

Figure 9.3: Mass Density for a uniform magnetic field present between $y = 6$ to 400, $\tilde{P} = 1 \times 10^{-3}$, $\tilde{\eta} = 1 \times 10^{-3}$, $\tilde{\rho}_0 = 100$, Hall plane dimensionless width is 10, $\Delta\tilde{x} = 0.01$ and $\Delta\tilde{y} = 0.01$. (a) $\tilde{B}_z = 1{\times}10^{-3}$ and (b) $\tilde{B}_z = -1{\times}10^{-3}$.

The x velocities show that the fluid is sloshing from side to side once it enters the magnetic field and then once again once it exits. The direction of the sloshing is reversed dependent on whether the magnetic field is into or out of the plane as can be see in Fig. 9.4a and Fig. 9.4b. This sloshing movement lines up to the changing mass density that is seen in Figs. 9.3a and 9.3b. Mass is driven in a sideways motion, this displacing of the mass continues until it is decelerated by the sides of the panel where it builds up, until accelerated in the other direction by internal pressure of the plasma. For a negative field the fluid velocity is greater on the left side of the plane and less on the right side of the plane compared to the fluids initial starting velocity, Fig. 9.4a; the opposite is true for a positive magnetic field Fig. 9.4b. The distance required for the $\tilde{V}_y$ to once again reach its original velocity across the plane is considerably greater than that of $\tilde{V}_x$. $\tilde{V}_y$ has a greater magnitude the closer to the edge of the plane it is, in a uniform magnetic field.

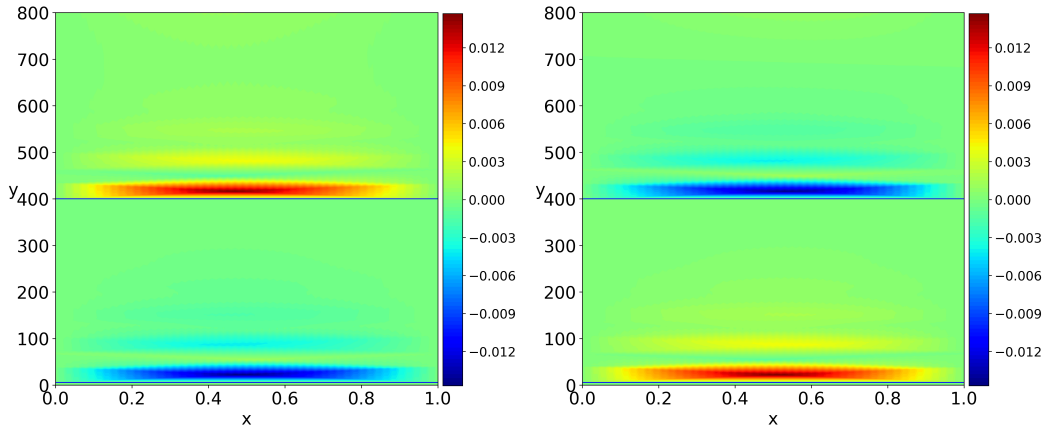

(a) (b)

Figure 9.4: x velocity for a uniform magnetic field present between y = 6 to 400, $\tilde{P} = 1\times10^{-3}$, $\tilde{\eta} = 1\times10^{-3}$, $\tilde{\rho}_0 = 100$, Hall plane dimensionless width is 10, $\Delta\tilde{x} = 0.01$ and $\Delta\tilde{y} = 0.01$. (a) $\tilde{B}_z = 1\times10^{-3}$ and (b) $\tilde{B}_z = -1\times10^{-3}$.

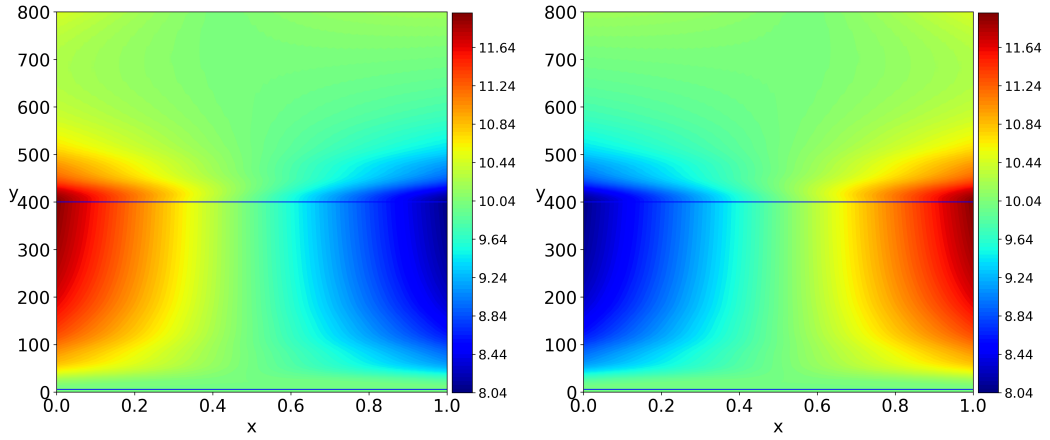

(a) (b)

Figure 9.5: y velocity for a uniform magnetic field present between y = 6 to 400, $\tilde{P} = 1\times10^{-3}$, $\tilde{\eta} = 1\times10^{-3}$, $\tilde{\rho}_0 = 100$, Hall plane dimensionless width is 10, $\Delta\tilde{x} = 0.01$ and $\Delta\tilde{y} = 0.01$. (a) $\tilde{B}_z = 1\times10^{-3}$ and (b) $\tilde{B}_z = -1\times10^{-3}$.

V_{HMHD} oscillates about V_{HC} on entering the magnetic field, Figs. 9.6a and 9.6b, this once again aligns with the sloshing that we see in the mass density and x velocity, Figs. 9.3a, 9.3b, 9.4a and 9.4b the charge oscillating between the two sides of the plane causes the V_{HMHD} to oscillate. Further into the magnetic field V_{HMHD} reaches a settled point where its value is the same as that given by V_{HC}. This is at the point when the mass density has reached a steady state

and the x velocity has gone to zero. On leaving the magnetic field V_{HMHD} oscillates once again about $V_{\text{HC}} = 0$, reaching a settled state of zero itself as the mass density homogenises and the x velocity reaches zero.

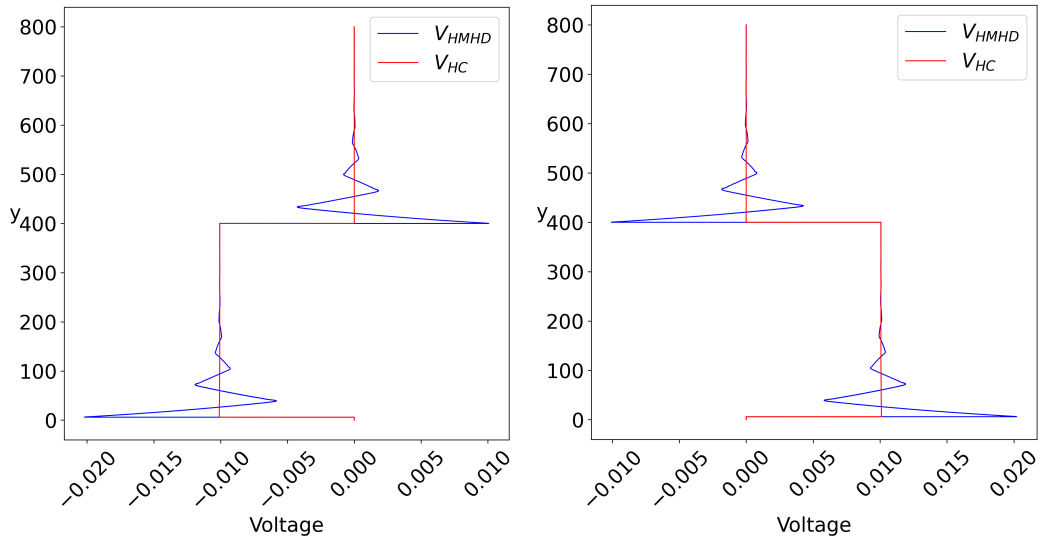

(a) (b)

Figure 9.6: Hall voltage for a uniform magnetic field present between $y = 6$ to 400, $\tilde{P} = 1\times10^{-3}$, $\tilde{\eta} = 1\times10^{-3}$, $\tilde{\rho}_0 = 100$, Hall plane dimensionless width is 10, $\Delta\tilde{x} = 0.01$ and $\Delta\tilde{y} = 0.01$. (a) $\tilde{B}_z = 1\times10^{-3}$ and (b) $\tilde{B}_z = -1\times10^{-3}$.

9.3 Applying the Finite Difference method for a Magnetic Monopole Field

The uniform region of magnetic field is replaced by a non-uniform magnetic field produced by a monopole we see stark differences in how the charged fluid behaves. The magnetic field at any point on the plane caused by a magnetic monopole is inversely proportional to $R(x, y)^3$, this means that the highest magnetic field on the plane is felt directly over the magnetic monopole, and this is also where we see the maximum change in mass density.

In Figs. 9.7a and 9.7b we see that there are two jets of mass density emerging

from the position directly above the monopole, one is a jet of lower mass density and the other a jet of higher mass density when compared to the initial mass density. Depending on the charge of the monopole the direction of the jets is reversed as can be seen when comparing the two figures. As we move further up the plane the mass density returns to its initial distribution.

The x velocity shows that the electron fluid is moving faster the closer it is to the magnetic monopole. Once the fluid moves away from the monopole, where the magnetic field becomes negligible, the x velocity around the centre of the plane reverses direction as the pressure parameter forces a more uniform distribution of number density, Figs. 9.8a and 9.8b.

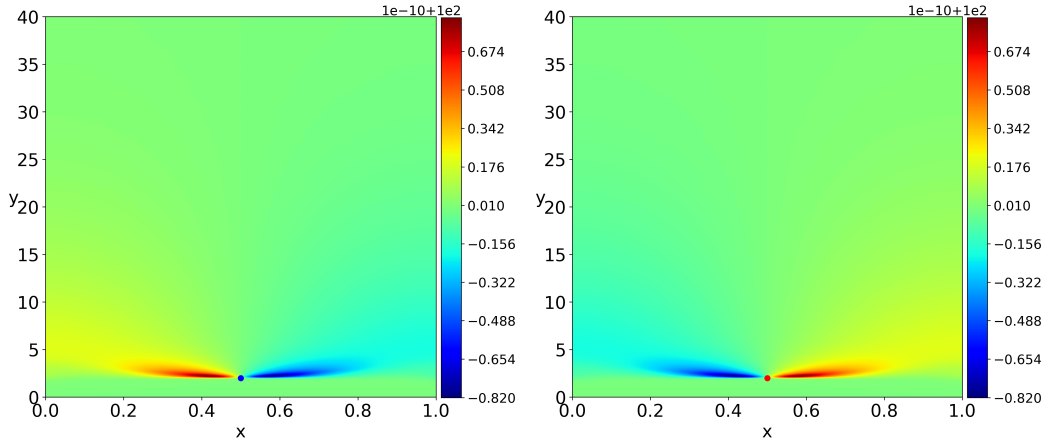

(a) (b)

Figure 9.7: Mass Density for a magnetic monopole field at position $\tilde{\alpha} = 1 \times 10^{-1}$, $\tilde{\eta} = \times 10^{-3}$, $\tilde{\rho}_0 = 100$, $\tilde{D} = 0.1$, $\Delta\tilde{x} = 0.005$ and $\Delta\tilde{y} = 0.005$. (a) $\tilde{Q}_m = 1 \times 10^{-12}$ and (b) $\tilde{Q}_m = -1 \times 10^{-12}$.

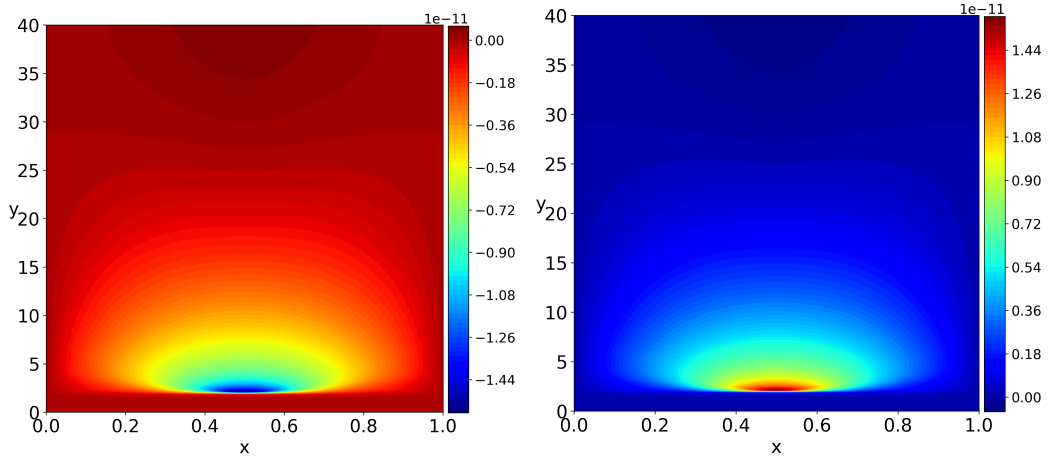

(a) (b)

Figure 9.8: x velocity for a magnetic monopole field at position $\tilde{\alpha} = 1 \times 10^{-1}$, $\tilde{\eta} = \times 10^{-3}$, $\tilde{\rho}_0 = 100$, $\tilde{D} = 0.1$, $\Delta\tilde{x} = 0.005$ and $\Delta\tilde{y} = 0.005$. (a) $\tilde{Q}_m = 1 \times 10^{-12}$ and (b) $\tilde{Q}_m = -1 \times 10^{-12}$.

The y velocity behaves in the same manner as for the uniform magnetic field. The velocity in the y direction is separated by a slower moving half and the faster moving half; they take a larger distance to return to an homogenised state when compared to V_y for a uniform magnetic field. The higher mass density is always on the side of the plane that has a higher y velocity, Figs. 9.9a and 9.9b. The highest and slowest velocities in the y direction are found at the edges of the sensor plane, the same as for the uniform magnetic field case.

The MHD Hall voltage has a peak that is twice as large as the classic Hall voltage as was to be expected from the derivation, Figs. 9.10a and 9.10b. The MHD Hall voltage sloshes to the opposite voltage after passing the monopole, corresponding to where the magnetic field of the monopole is negligible. As with the uniform case a sloshing motion occurs in a monopoles magnetic field but as we will see later on this is variable dependent.

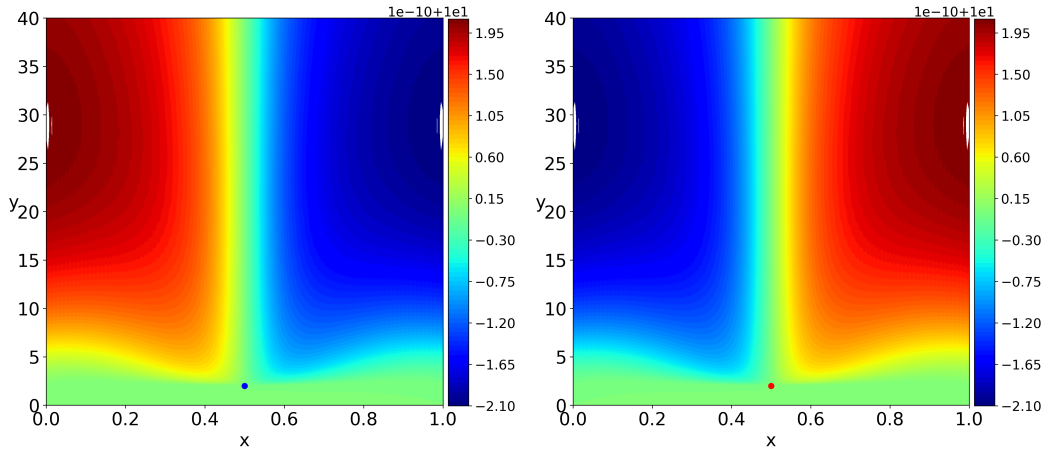

(a) (b)

Figure 9.9: y velocity for a magnetic monopole field at position $\tilde{\alpha} = 1 \times 10^{-1}$, $\tilde{\eta} = \times 10^{-3}$, $\tilde{\rho}_0 = 100$, $\tilde{D} = 0.1$, $\Delta\tilde{x} = 0.005$ and $\Delta\tilde{y} = 0.005$. (a) $\tilde{Q}_m = 1 \times 10^{-12}$ and (b) $\tilde{Q}_m = -1 \times 10^{-12}$.

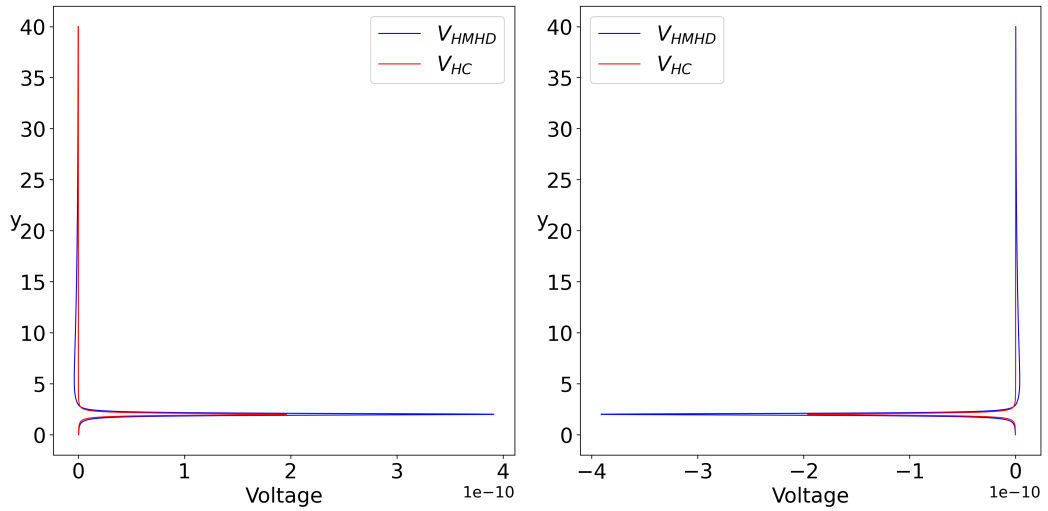

(a) (b)

Figure 9.10: Hall voltage for a magnetic monopole field at position $\tilde{\alpha} = 1 \times 10^{-1}$, $\tilde{\eta} = \times 10^{-3}$, $\tilde{\rho}_0 = 100$, $\tilde{D} = 0.1$, $\Delta\tilde{x} = 0.005$ and $\Delta\tilde{y} = 0.005$. (a) $\tilde{Q}_m = 1 \times 10^{-12}$ and (b) $\tilde{Q}_m = -1 \times 10^{-12}$.

9.4 Exploration of the Variables in the Equations of motion

In Appendix D.2 a detailed description of how the altering the variables affects the Hall voltage is shown. The behaviour of each variable is looked at with both the uniform magnetic field and one that is produced by a magnetic monopole. One of the most important results, from the exploration of the variables, is that there is an optimised distance for the monopole from the plane to maximise the Hall voltage.

Given that the magnetic field perpendicular to the plane, B_z, changes with the distance away form the monopole we can go from a weak magnetic field but a more uniform magnitude across the plane or a high magnetic field concentrated in a small area with rest of the plane having a weak field. Measuring the peak of the MHD Hall voltage of a single monopole it can be seen that there is an optimal distance to measure, to produce the greatest peak Hall voltage, that distance is approximately 10^{-3} to 10^{-4} m; this can be seen in Fig. 9.11.

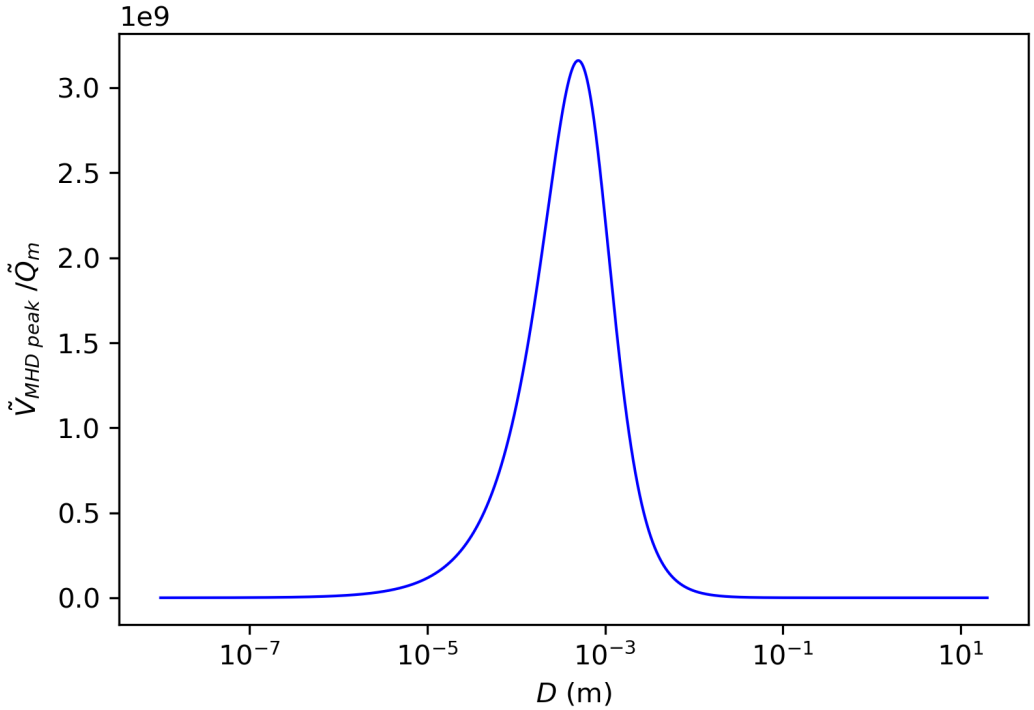

Figure 9.11: The peak in dimensionless Hall voltage generated by magneto-hydrodynamics, $\tilde{V}_{MHD\ peak}$, scaled by dimensionless monopole charge, $\tilde{Q}_m$ vs distance away from the plane the magnetic monopole is, expressed in meters, D.

9.5 Applying the MHD simulation to Real Materials

In this section we look at three different materials that have a two dimensional profile, i.e. length and width but no thickness. Silicon and Gallium Arsenide are semi-conductors that have been used extensively in Hall effect devices, the final one being Graphene a two dimensional material that is currently being utilised in producing experimental electronic devices with impressive results [81, 82]. Applying the MHD simulation to Silicon, Gallium Arsenide, and Graphene we can observe how each of these behave under the same conditions but with their own specific properties of charge carrier density and resistivity, Table 9.1.

Material	Resistivity, (Ωm)	Electron Number Density, (n/m^2)
Silicon	1	1.45×10^{10}
Gallium Arsenide	1×10^{-7}	1.8×10^{8}
Graphene	2×10^{-4}	10^{10}

Table 9.1: Resistivity and charge carrier density for various materials. Resistivity for the materials were sourced from the following: Silicon [83], Gallium Arsenide [84], and Graphene [85]. Electron number densities sourced from: Silicon [86,87], Gallium Arsenide [88], and Graphene [89,90]. Electron number density in two dimensions has been extrapolated from the number density in three dimensions by raising to the power 2/3.

Once the dimensions of the Hall sensor have been chosen, the only physical quantities that can be altered are the applied voltage and the material of the Hall sensor. With this in mind choosing a suitable voltage will ensure the electron fluid flows against the resistance of the sample. Using a mono-layer Silicon with the charge density and resistivity shown in Table 9.1, and with dimensions of 1×10^{-3}m in the x direction and 8×10^{-2}m in the y direction to form the Hall sensor. A uniform magnetic field of 5×10^{-5}T (the magnetic field strength of the Earth ranges from 2×10^{-5}T to 5×10^{-5}T [91]) is applied across the entire width of the Hall sensor within the region $y = 2 \times 10^{-3}$m to $y = 40 \times 10^{-3}$m.

The first aspect to test is changing the applied voltage observing what effect it has on the mass density, the velocities and the Hall voltage produced by electron fluid. I will be decreasing from a starting voltage of 5×10^{-4}V to 5×10^{-6}V. The step size used in this simulation is 5×10^{-6}m.

Moving through Figs. 9.12a to 9.12c in all cases the mass density has shifted towards the left of the plane. The amount of mass density that has moved

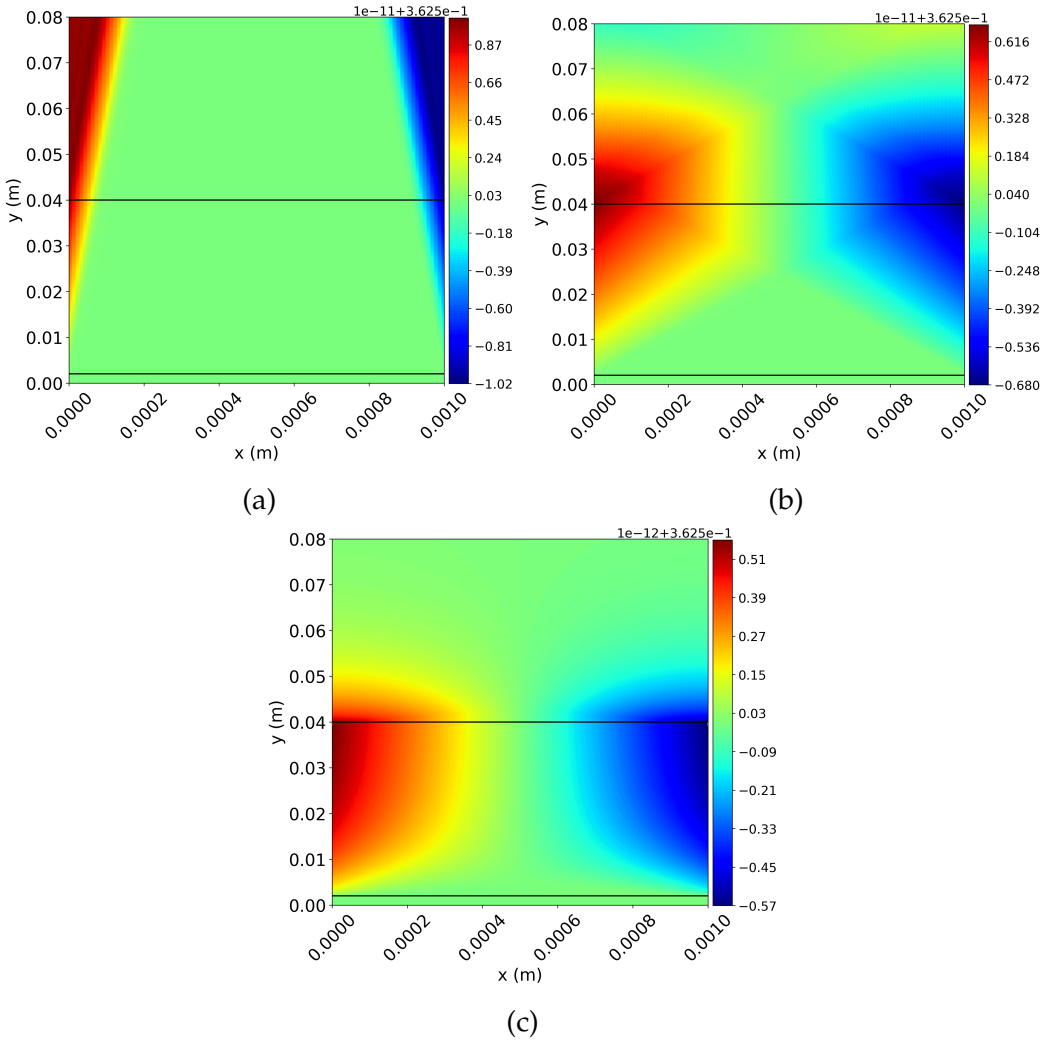

Figure 9.12: Mass density plots for a silicon monolayer material with applied voltage: (a) 5×10^{-4} V, (b) 5×10^{-5} V, and (c) 5×10^{-6} V.

towards the left has decreased with applied voltage, this is also the case with V_x, Figs. 9.13a to 9.13c, which decreases in peak magnitude with voltage. The initial starting V_y decreases with applied voltage Figs. 9.14a to 9.14c. The Hall voltage, both the classical and the MHD, decrease with the decreasing applied voltage. V_{HMHD} goes form being an over-damped system, Fig. 9.15a, to under-damped, Fig. 9.15b, to finally being a critically damped MHD Hall voltage, Fig. 9.15c.

Next let us look at the Hall voltages produced by different materials in a uniform magnetic field. We can compare the Hall voltages produced by

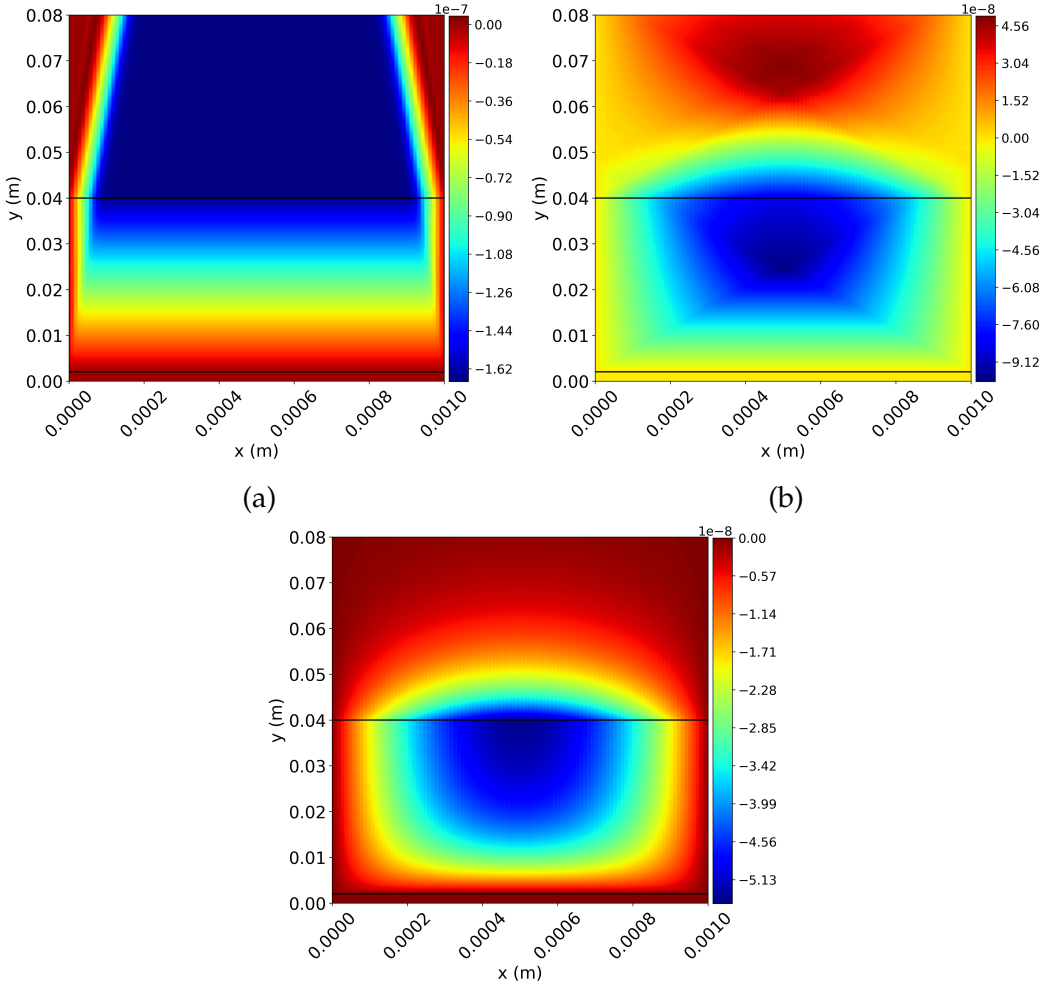

Figure 9.13: V_x plots for a silicon monolayer material with applied voltage: (a) 5×10^{-4} V, (b) 5×10^{-5} V, and (c) 5×10^{-6} V.

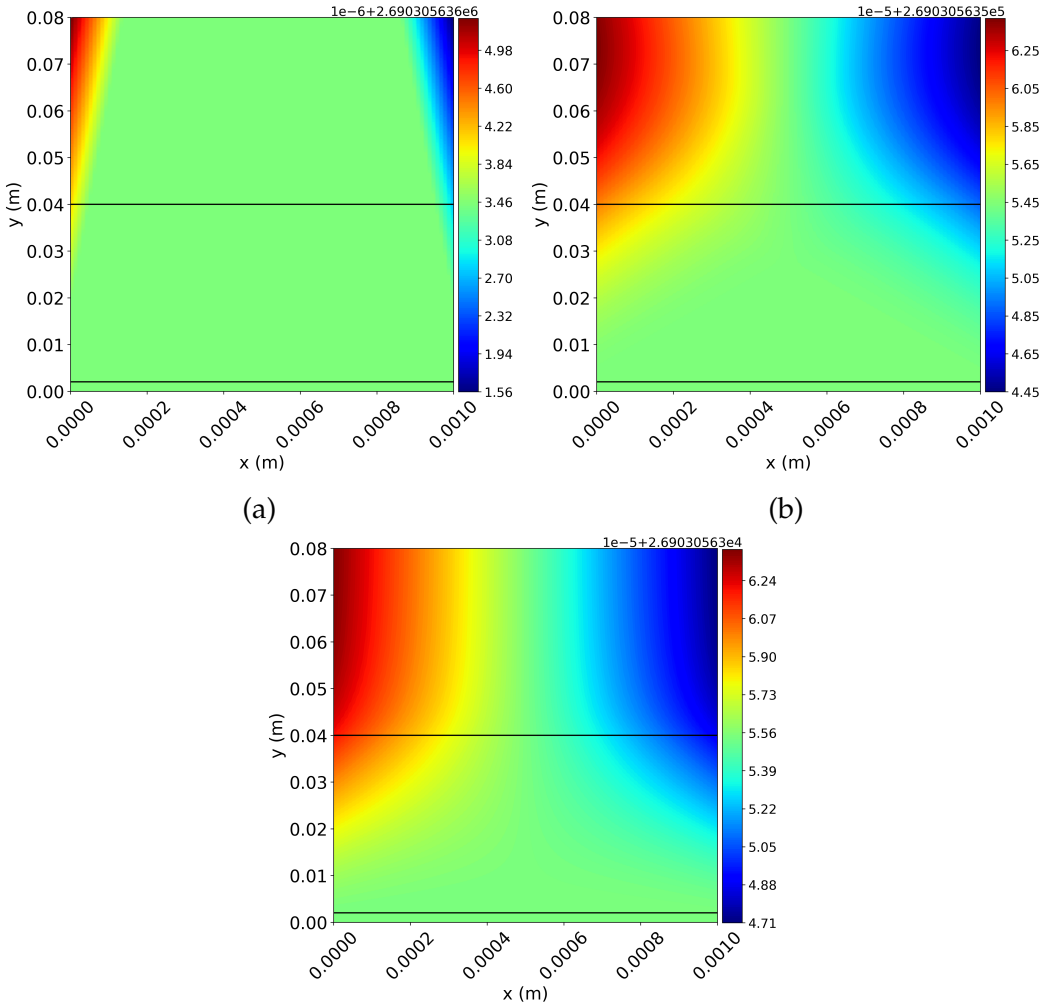

Figure 9.14: V_y plots for a silicon monolayer material with applied voltage: (a) 5×10^{-4} V, (b) 5×10^{-5} V, and (c) 5×10^{-6} V.

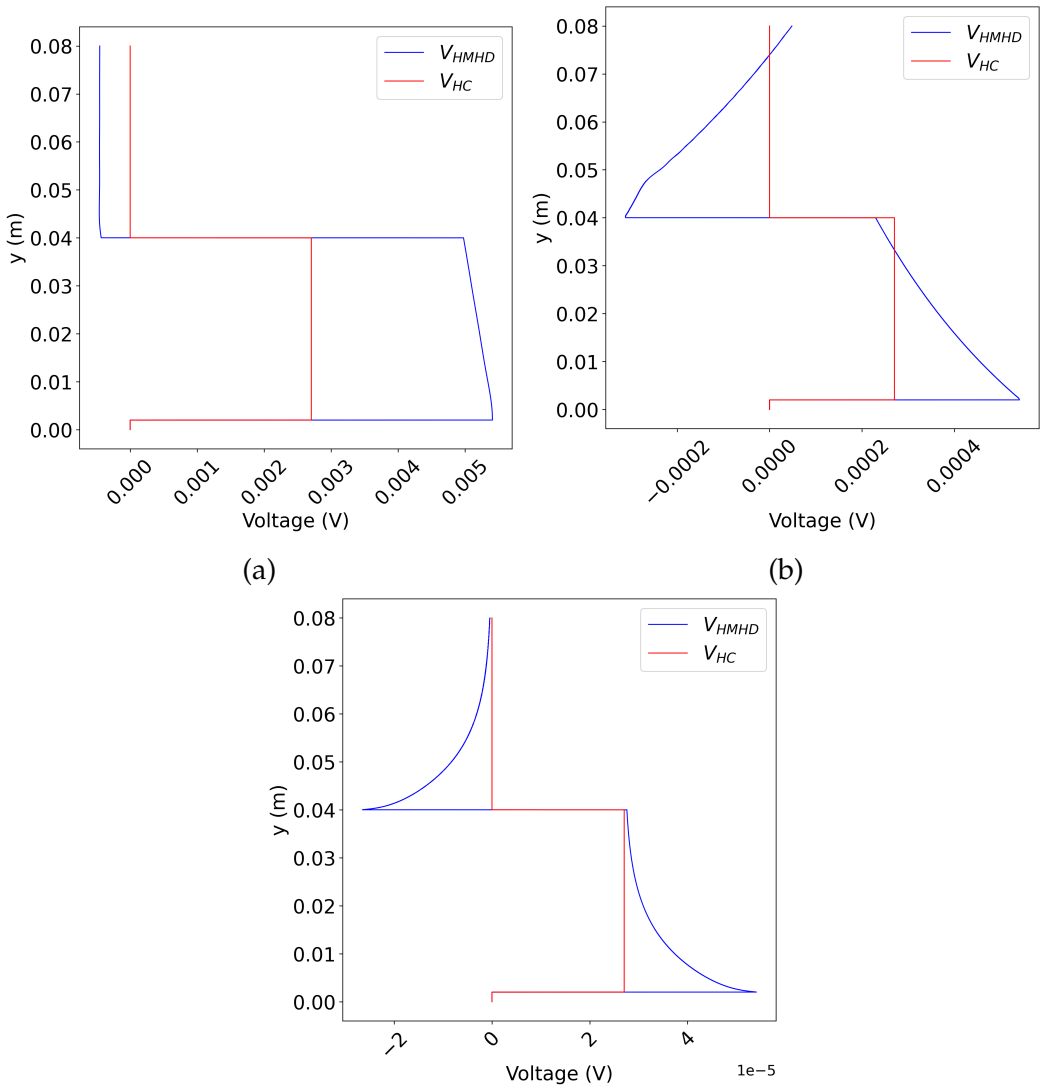

(a) (b)

(c)

Figure 9.15: Hall voltage plots for a silicon monolayer material applied voltage: (a) 5×10^{-4} V, (b) 5×10^{-5} V, and (c) 5×10^{-6} V.

Silicon (Fig. 9.16a), Graphene (Fig. 9.16b), and Gallium Arsenide (Fig. 9.16c). All three samples produce the same peak MHD Hall voltage, due to the same initial starting velocity (which we can alter by differing the applied voltage). How the MHD Hall voltage decays to the classical Hall voltage is different dependent on what material the Hall sensor plane is made from. To tell which is the better material for producing a Hall voltage we can look at the current, voltage and power supplied to get the same classical Hall voltages and peak MHD Hall voltage. Looking at Table 9.2 we can see that Gallium Arsenide requires less power to produce the same Hall voltage when compared to Silicon and Graphene, while Graphene is better than Silicon requiring less power to generate the same Hall voltage.

Material	Current (A)	Voltage (V)	Power (W)
Silicon	2.32×10^{-8}	1.86×10^{-6}	4.32×10^{-14}
Graphene	1.60×10^{-8}	2.56×10^{-10}	4.11×10^{-18}
Gallium Arsenide	2.88×10^{-12}	2.31×10^{-16}	6.65×10^{-28}

Table 9.2: Table of current, applied voltage and power required to produce the Hall voltages seen in Figs. 9.16a to 9.16c. We see that the lowest power required was by the Gallium Arsenide, then Graphene and finally Silicon was the poorest performer.

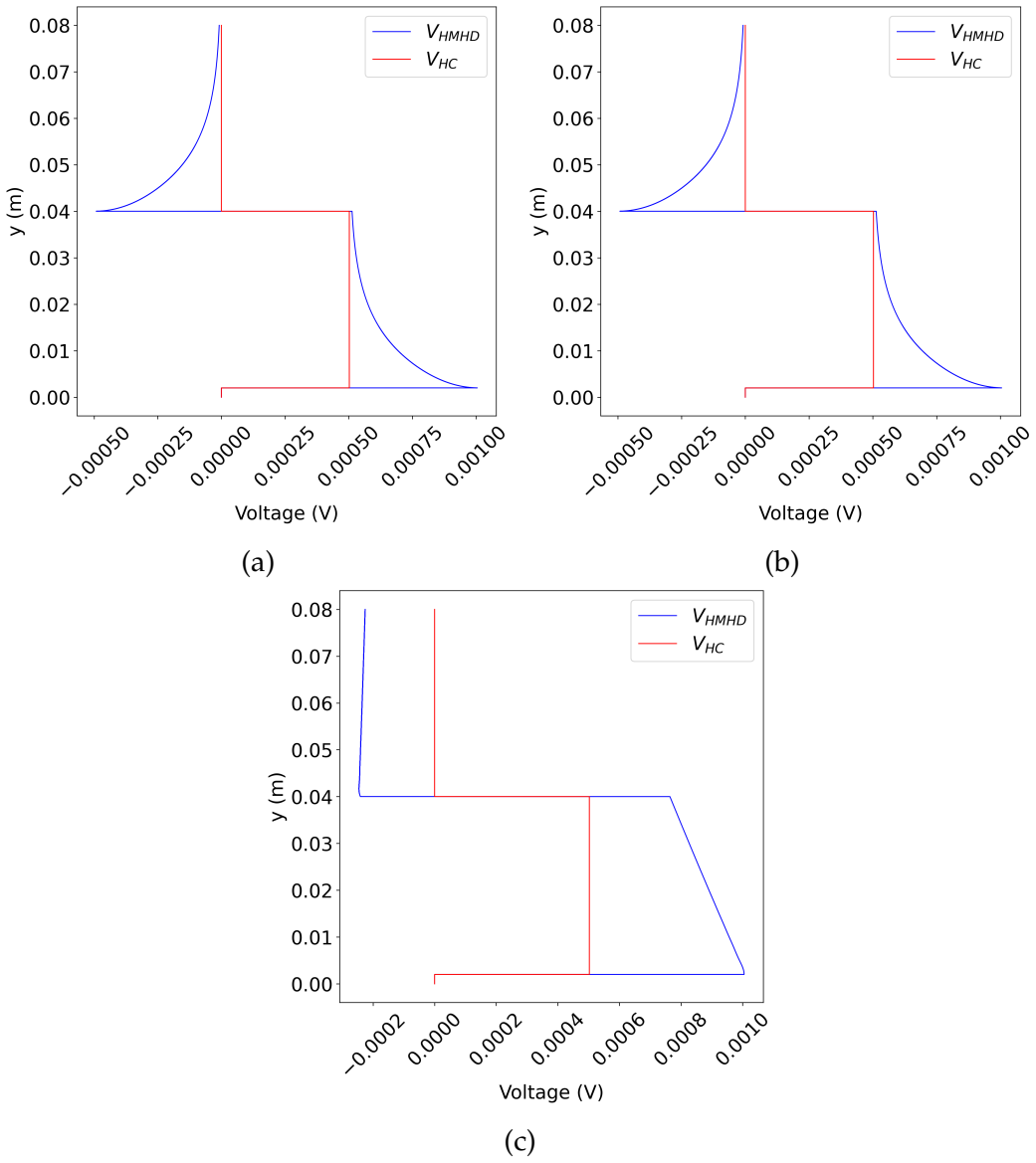

Figure 9.16: Hall voltages produced by different materials with the same applied current and voltage (a) Silicon, (b) Graphene, and (c) Gallium Arsenide.

9.6 Applying the MHD Simulation to Dirac Monopoles

The following results for monopoles are utilising Dirac monopoles of charge Q_D, Eq. (2.8), in various arrangements. The value of $n = 1$ is chosen for the smallest Dirac monopole charge. The other parameters that have been chosen are plane width 0.001m, plane length 0.001m. The voltage applied

in the y direction is 1×10^{-3}V, all monopole distances to the plane are $D = 1 \times 10^{-4}$m. The step sizes used for this simulation are $\Delta x = 5 \times 10^{-6}$, $\Delta y = 5 \times 10^{-6}$ and the material used is a two dimensional Silicon with properties shown in Table 9.1.

Placing in values for real material the differences from the initial mass density and V_y are so small that they cannot be seen, as such these plots are not shown.

The uniform field highlighted what effect material and applied voltage can have on the Hall effect. Here I will look at how different monopole layouts can effect the Hall voltage. Using the magnetic monopole layouts that were shown in the introduction to this project (Figs. 8.2a to 8.2d). The greatest V_x is of the order of 10^{-12} ms^{-1} see Fig. 9.17a. This explains why there is a very small change in the mass density around the magnetic monopole. A Hall voltage with a single peak aligned with the magnetic monopole, Fig. 9.18a with a peak Hall voltage of approximately 6×10^{-6}V.

For two monopoles positioned directly above one another, with opposite magnetic charges, we see that V_x moves to the left after passing the initial negatively charged Dirac monopole. When reaching the second positively charged Dirac monopole the plasma is accelerated to the right leaving $V_x = 0$, Fig. 9.17b. The Hall voltages reach the same magnitude as that for a single monopole $V_{\text{HMHD}} \approx 6{\times}10^{-6}$V and $V_{\text{HC}} \approx 3{\times}10^{-6}$V initially as a positive voltage concentrated over the negatively charged monopole, then as a negative voltage centred over the positively charged monopole see Fig. 9.18b.

Arranging two oppositely charged Dirac monopoles in a horizontally aligned configuration. They are far enough away form each other for V_x to behave as if the other monopole was not present, with both pushing the electron

fluid in opposite directions, Fig. 9.17c. The Hall voltages on the other hand are not as unaffected. The summation of the Hall voltages produced by each monopole across the plane cancel out and what we are left with is a noise. The noise likely caused by floating point rounding errors from the computational calculation. Interestingly there is still a peak in these errors aligned at the same y coordinate as the two Dirac monopoles, Fig. 9.18c.

Finally looking at a random arrangement of Dirac monopoles, here higher magnitudes of V_x of the order 10^{-10} are achieved (compared to a single or double monopole configuration), Fig. 9.17d. This is due to some of the monopoles being close enough to form stronger or larger areas of magnetic field see Fig. 8.2d. The Hall voltage is produced by varying levels of reinforcement and shielding of the effects of a single monopole on the electron fluid by the monopoles that surround it, Fig. 9.18d.

9.7 Summary

The finite difference method is an established method of solving fluid dynamics problems and that remains the case for magnetohydrodynamics. In a uniform field oscillations can be formed in the mass density and the Hall voltage as the electron gas sloshes across the plane and the internal pressure pushes it back in the opposing direction. Due to the short duration of the magnetic field caused by the monopole a single peak in Hall voltage is produced about the y position of the magnetic monopole before returning to zero, with less sloshing.

When real values for materials are chosen the same peak in the Hall voltage is achieved across the three materials, but more or less power has to be applied showing that each material has a different sensitivity to the Hall effect. The

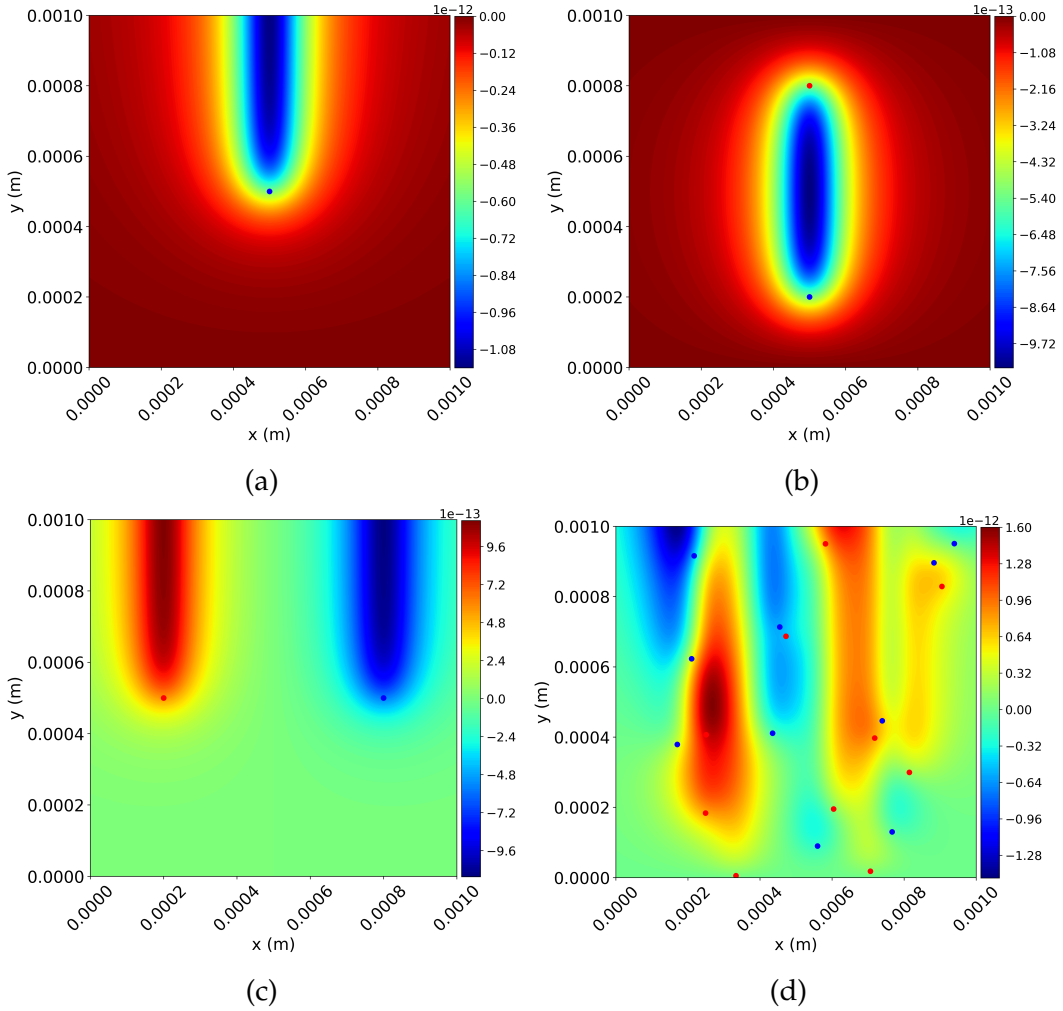

Figure 9.17: V_x for arrangements of monopoles, (a) A single magnetic monopole at the centre of the Hall sensor (b) Two oppositely charged magnetic monopole arranged vertically above one another the lower being a negatively charged Dirac monopole and the upper being a positively charged Dirac monopole, (c) Two oppositely charged magnetic monopoles arranged horizontally from one another the left side is a positively charged Dirac monopole and the right side is a negatively charged Dirac monopole, and (d) Randomly placed Dirac magnetic monopoles of opposite charges but equal in number.

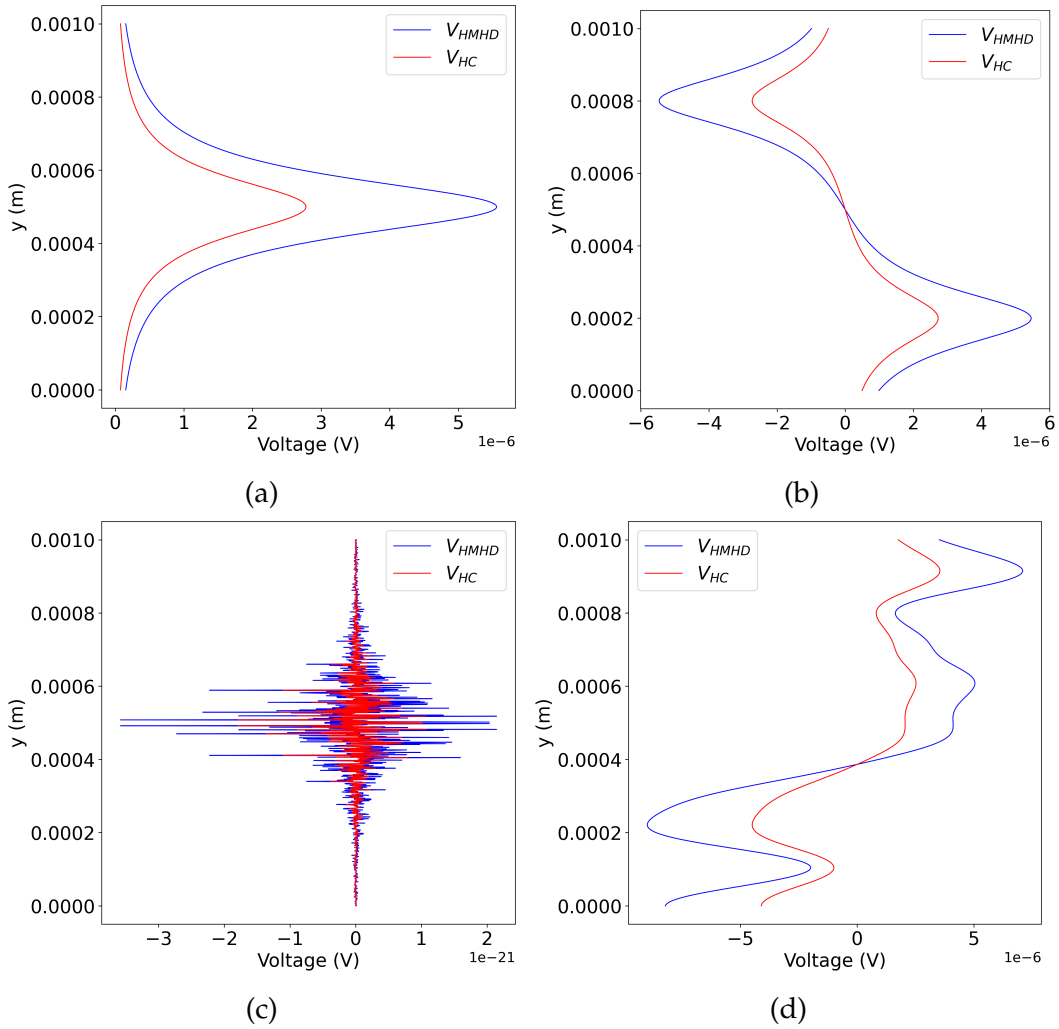

Figure 9.18: The Hall voltages for arrangements of monopoles, (a) A single magnetic monopole at the centre of the Hall sensor (b) Two oppositely charged magnetic monopole arranged vertically above one another the lower being a negatively charged Dirac monopole and the upper being a positively charged Dirac monopole, (c) Two oppositely charged magnetic monopoles arranged horizontally from one another the left side is a positively charged Dirac monopole and the right side is a negatively charged Dirac monopole, and (d) Randomly placed Dirac magnetic monopoles of opposite charges but equal in number

decay in V_{HMHD} from the peak to a steady value is different for each material. A single magnetic monopole with a magnetic charge of Q_D (at a distance of $D = 1 \times 10^{-4}$m from the surface of the Hall sensor that has dimensions of 1mm by 1mm with an applied voltage of 10^{-3}V) produces a peak Hall voltage of approximately 6×10^{-6}V. Additional magnetic monopoles can act to increase or decrease Hall voltage depending on monopole charge and position.

Chapter 10

Discussion and Conclusion

10.1 Discussion

In the derivation of the Hall voltage for an MHD regime the assumption was made that when the electron fluid had reached a settled state and was no longer sloshing on the plane (in the uniform field case) it should return a Hall voltage that is the same as the classical case Eq. (8.50). The result of this assumption is that initially when the fluid enters the magnetic field the pressure term in Eq. (8.78) is zero so the Hall voltage is initially double. It is only when the pressure term becomes great enough to overcome the Lorentz force of the magnetic field that the fluid is accelerated in the opposite direction and a build up of fluid is created on the opposite side of the plane. This process repeats back and forth, slowly settling to a point where the force supplied by the internal pressure of the fluid is equal and opposing the force supplied by the magnetic field. We also have the same effect happen on exiting the magnetic field but this time the Lorentz force is zero so the spike in Hall voltage is driven by the pressure within the plasma itself, where it will continue to slosh at ever decreasing amplitudes until the electron fluid

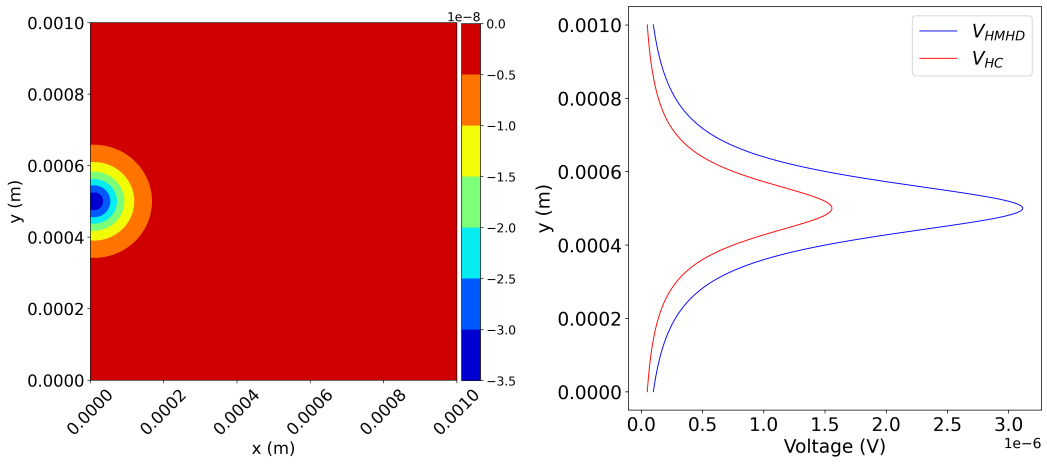

(a) (b)

Figure 10.1: Plots of (a) magnetic field and (b) Hall voltage for a single Dirac monopole positioned against the side of the sensor panel. The material is Silicon, $D = 5 \times 10^{-5}$m, $I_{y0} = 3 \times 10^{-8}$A, and the applied voltage is 1×10^{-3}V.

becomes homogenised in the x axis and the pressure term is once again zero causing the MHD Hall voltage to also return to zero Volts.

In the monopole simulations run for this thesis, the monopole is placed near to the centre of the plane. Placing the Dirac monopole at the boundary, Fig. 10.1a, we get a Hall voltage, Fig. 10.1b, that is approximately a half of what it was when the magnetic monopole was located at the centre of the plane the centre of the plane, Fig. 9.18a.

The results for V_{HMHD} and V_{HC} for the various materials return the same results for each type of voltage, but hide the fact that each material has a different sensitivity to producing a Hall voltage. The easiest way to categorize how sensitive a material is to the Hall effect is by how large the Hall coefficient is. This remains true for a magnetohydrodynamic treatment and also for two dimensional materials with a two dimensional Hall coefficient,

$$R_{\mathrm{H2D}} = \frac{1}{n q_e} \mathrm{m}^2\mathrm{C}^{-1}. \tag{10.1}$$

If value of R_{H2D} is higher than in another material then the current required to produce the same Hall voltage will be lower. This means that a lower R_{H2D} material has a lower sensitivity to the Hall effect when compared to another material with a higher value of R_{H2D}.

Calculating the Hall voltages for the three different materials with the currents shown in Table 9.2, the two dimensional Hall coefficients from Table 10.1 and the uniform magnetic field of -5×10^{-5}T we get a Hall voltage of 5×10^{5}V. This calculated Hall voltage matches that seen in the V_{HC} simulated results, Fig. 9.16. A direct comparison between the MHD simulation and the formula is not possible as the pressure gradient is not known across the plane, but an approximate calculation of the peak in the MHD Hall voltage (where the gradient in the mass density is negligible) as being $V_{\mathrm{HMHD}} \approx 2V_{\mathrm{HC}}$. As can be seen in Eqs. (8.13) and (8.57) both are proportional to R_{H2D} so even with the added complexity of the pressure component in the V_{HMHD} the R_{H2D} is a reliable indicator of a materials sensitivity to Hall effects.

Material	nq_e (Cm^{-2})	R_{H2D} ($\mathrm{m}^2\mathrm{C}^{-1}$)
Silicon	-2.32×10^{-9}	-4.30×10^{8}
Gallium Arsenide	-2.90×10^{-13}	-3.45×10^{12}
Graphene	-1.60×10^{-8}	-6.24×10^{8}

Table 10.1: Table comparing the charge density and R_{H2D} for different materials

As we can see in Table 10.1 Gallium Arsenide is the best material of which to construct a Hall effect device for the same applied of voltage. The Hall voltages produced by Silicon and Graphene take more power (see Table 9.2) to produce the same Hall voltage than that of Gallium Arsenide, the relative

sensitivity of a material to the Hall effect both classical and MHD can be gauged by comparing a materials R_{H2D} value (see Table 10.1). The same conclusions are drawn in three dimensions with experimental results and established theoretical predictions of the Hall effect, [92,93], namely that the Hall coefficient will dictate how sensitive a material is to the Hall effect.

10.2 Conclusion

After searching not much material could be found on using magnetohydrodynamics to investigate the Hall effect. The closest investigations are currently focused on treating two dimensional electron gases on a Graphene lattice as fluids. These investigations utilise hydrodynamics to model the flow of the electrons, [94, 95], with experiments producing aligning results [96,97].

Treating the flow of a two dimensional electron gas as a charged fluid in a uniform magnetic field produces the same Hall voltage as Eq. (8.11). The interesting result that the magnetohydrodynamic calculation gave was the oscillation / sloshing of the electron plasma before it settled down to a consistent value of Hall voltage. This sloshing movement could be seen in the mass density and the velocity of the fluid, in the direction tangential to applied current. When it came to the single magnetic monopole the magnetohydrodynamic Hall voltage overshoots the Hall voltage. In both the uniform and non-uniform magnetic fields the cause for the discrepancy between the Hall voltage and the Magnetohydrodynamic Hall voltage is caused by the electrostatic pressure of the electrons between one another.

The question as to whether the Hall voltage can be useful as a means of detecting magnetic monopoles is not as simple as the results would suggest.

A voltage of the order 10^{-6}V would require an appropriate voltmeter, but this is for a Dirac monopole. Detecting spin ice with a magnetic charge approximately 1/8000 less would be considerably more challenging. Until a highly sensitive semi conductor that could be used as a Hall sensor is developed the better option would be to use a SQUID device.

Future direction of the project could include a three dimensional analysis where instead of being a two dimensional fluid it is now three dimensional. Possible methods for solving this could be three dimensional finite difference or even a finite volume analysis [98, 99]. Another area to be explored is time dependency of the electron fluid. This could be achieved by adding time dependency to the finite difference model or via a Lattice Boltzmann simulation, [100–102]. An example of a Lattice Boltzmann simulation can be seen in the series of figures which increase in time Figs. 10.2a to 10.2d, using an adapted code from [103] which displays the density of the fluid but can also be used to measure the vorticity of the fluid.

10.3 Thesis Summary

This thesis focused on two main questions the first of which is can an electron be bound to a magnetic monopole if constrained to a plane adjacent to it? Classically it was found that the electron can be bound for a given value of energy and proximity to the point on the plane sitting directly above the monopole. Outside of this the electron will scatter away from the monopole. In a quantum mechanical framework the electron was found to be quasi-bound, decaying over time into a scattering state. The minimum monopole charge required to bind an electron was found to be $16Q_D$ and for a magnetic needle this resulted in a lifetime of approximately 5×10^{-7}s. The binding of an electron confined to two dimensions about a magnetic monopole could be

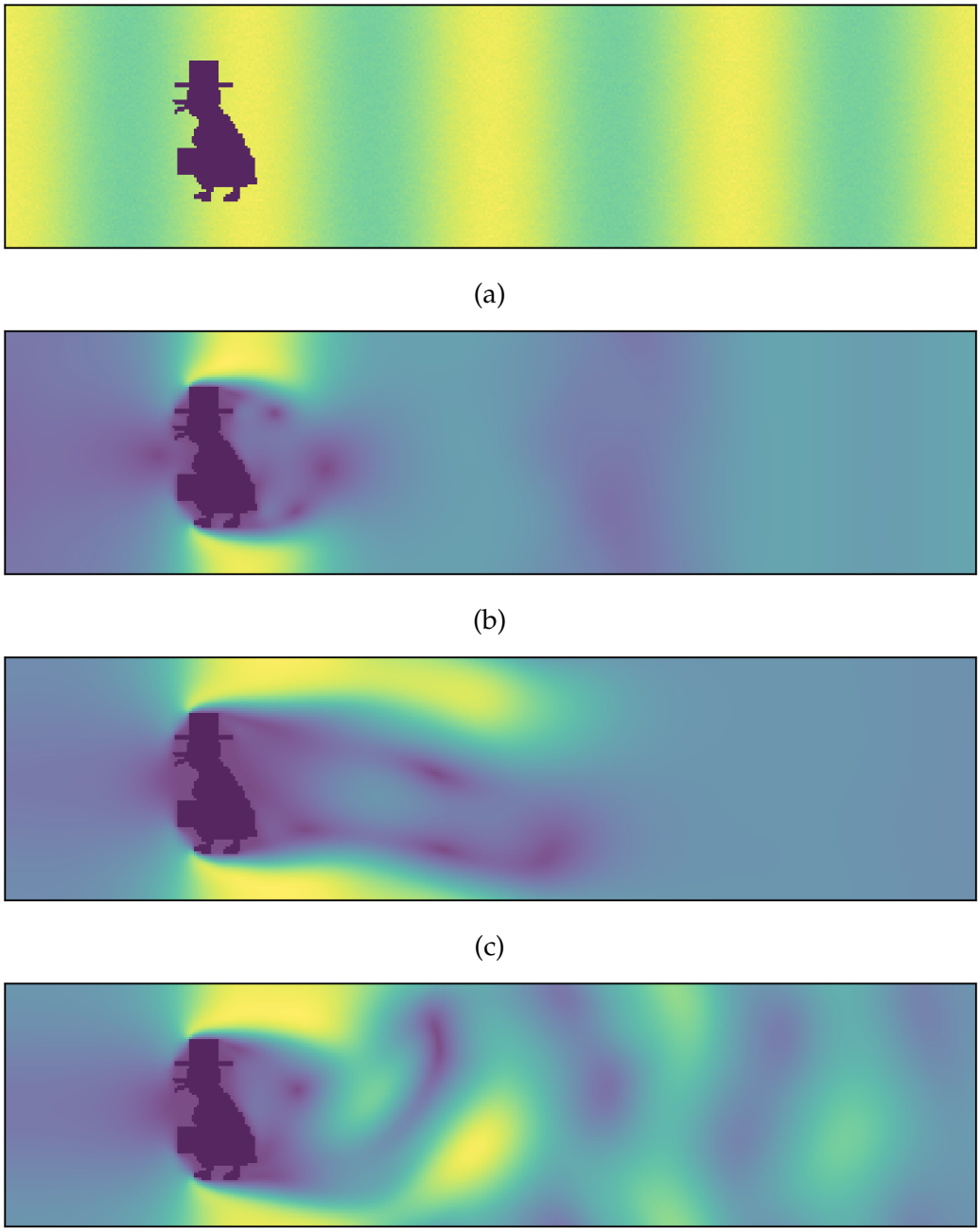

(a)

(b)

(c)

(d)

Figure 10.2: Fluid density around a duck with a top hat and briefcase at simulation ticks (a) 0, (b) 11, (c) 36 and (d) 97. Yellow is high density and blue is low density and green lays in between the two.

achieved experimentally with a sufficiently charged magnetic needle.

The second question was can a magnetic monopole be detected with the Hall voltage? The answer is yes for Dirac monopoles but currently not practical for effective monopoles in spin-ice. For a Dirac monopole at the optimum distance form the Hall sensor plane the peak in Hall voltage was found to be of the order 10^{-6}V, this is of a value that specialist equipment can measure [104]. The simulations run in this thesis has the magnetic monopoles placed at the optimum distance form the plane and having a charge of $1Q_D$. The Hall voltage produced by spin ice would be orders of magnitude lower due to the monopole charge being 1/8000 of a Dirac charge and there is no guarantee that the monopoles will form at the optimum distance. It is for this reason while a Hall voltage would be produced detecting anything other than strong magnetic charges the Hall effect would not be practical for this use. Currently CERN are looking for magnetic monopoles with charge 2_D to $45Q_D$ in the MoDEL experiment (Monopole and Exotics Detector at the Large Hadron Collider) [105] and $1Q_D$ to $2Q_D$ in the ATLAS experiment [106]. Both of these experiments have cost billions of pounds and are multi-national efforts due to the scale and complexity of the design, construction and operation of the facilities. An alternative method is MACRO [107] a large area underground liquid scintillator detector looking for monopoles that interact with the fluid, this experiment ran from 1988 to 2000 [108]. Currently the cheapest and easiest way to build a monopole detector is by the induction technique, where the monopole passes through a superconducting ring inducing a permanent current [109]. Using the Hall effect with a two dimensional electron gas has the potential to be both a cheaper method and one not requiring cooling to near absolute zero temperatures.

Bibliography

[1] B. Cabrera, "First results from a superconductive detector for moving magnetic monopoles," *Physical Review Letters*, vol. 48, pp. 1378–1381, 5 1982.

[2] P. Dirac, "Quantised singularities in the electromagnetic field," *Proceedings of the Royal Society of London. Series A, Containing Papers of a Mathematical and Physical Character*, vol. 133, no. 821, pp. 60–72, 1931.

[3] R. Heras, "Dirac quantisation condition: a comprehensive review," *Contemporary Physics*, vol. 59, pp. 331–355, 10 2018. doi: 10.1080/00107514.2018.1527974.

[4] collaboration ATLAS, "Quest for the curious magnetic monopole continues," 2023. Avaliable at `https://home.cern/news/news/physics/quest-curious-magnetic-monopole-continues`, last accessed 04/04/2024.

[5] A. Lopatka, "A new search for magnetic monopoles," *Physics Today*, vol. 75, pp. 14–16, 4 2022.

[6] S. Errede, "Magnetic monopoles - fundamantal / point-like magnetic charges," 2007. Avaliable at `https://hep.physics.illinois.e`

du/home/serrede/P435/Lecture_Notes/P435_Lect_18.pdf, last accessed 08/07/2024.

[7] C. Castelnovo, R. Moessner, and S. L. Sondhi, "Magnetic monopoles in spin ice," *Nature*, vol. 451, pp. 42–45, 2008.

[8] S. T. Bramwell and M. J. Harris, "The history of spin ice," *Journal of Physics: Condensed Matter*, vol. 32, p. 374010, 2020.

[9] S. Ladak, D. E. Read, G. K. Perkins, L. F. Cohen, and W. R. Branford, "Direct observation of magnetic monopole defects in an artificial spin-ice system," *Nature Physics*, vol. 6, pp. 359–363, 2010.

[10] G.-W. Chern, P. Mellado, and O. Tchernyshyov, "Two-stage ordering of spins in dipolar spin ice on the Kagome lattice," *Physical review letters*, vol. 106, p. 207202, 5 2011.

[11] R. F. Wang, C. Nisoli, R. S. Freitas, J. Li, W. McConville, B. J. Cooley, M. S. Lund, N. Samarth, C. Leighton, V. H. Crespi, and P. Schiffer, "Artificial 'spin ice' in a geometrically frustrated lattice of nanoscale ferromagnetic islands," *Nature*, vol. 439, pp. 303–306, 2006.

[12] A. Beche, R. V. Boxem, G. V. Tendelo, and J. Verbeeck, "Magnetic monopole field exposed by electrons," *Nature Physics*, vol. 10, 2014.

[13] L. D. C. Jaubert and R. Moessner, "Multiferroicity in spin ice: Towards magnetic crystallography of $Tb_2Ti_2O_7$ in a field," *Physical Review B*, vol. 91, p. 214422, 6 2015.

[14] K. T. McDonald, "Birkeland, Darboux and Poincaré: Motion of an electric charge in the field of a magnetic pole," 2017. Avaliable at

http://kirkmcd.princeton.edu/examples/birkeland.pdf, last accessed 04/04/2024.

[15] H. Poincaré, "Remarques sur une expérience de M. Birkeland," *Comptes Rendus de l'Académie des sciences*, vol. t.123, pp. 530–533, 1896.

[16] I. A. Taimanov, "Geometry and quasiclassical quantization of magnetic monopoles," *Theoretical and Mathematical Physics*, vol. 218, pp. 129–144, 1 2024.

[17] J. Pooley, *Quantum Treatment of Quasi-Bound States in a 2-Dimensional Electron Gas Situated Above a Magnetic Monopole*. University of Kent Masters Thesis supervised by J. Quintanilla, 2018.

[18] L. Landau, "Diamagnetismus der Metalle," *Zeitschrift für Physik*, vol. 64, pp. 629–637, 1930.

[19] S. M. Girvin and K. Yang, *Modern condensed matter physics*. Cambridge University Press, 2019.

[20] M. D. Smith, *Astrophysical jets and beams*. Cambridge University Press, 2012.

[21] D. J. Mullan, *CRC series in pure and applied physics: Physics of the Sun*. CRC, 2010.

[22] K. S. Thorne and R. D. Blandford, *Modern classical physics : optics, fluids, plasmas, elasticity, relativity, and statistical physics*. Princeton University Press, 2017.

[23] N. S. Clay Mathematics Institute, "Navier-stokes equation." Avaliable at https://www.claymath.org/millennium/navier-stokes-equation/, last accessed 03/04/2024.

[24] J. J. Sakurai, *Modern Quantum Mechanics*. Menlo Park, Calif. [u.a.]: Benjamin/Cummins, 1st ed., 1994.

[25] D. J. Griffiths, *Introduction to Electrodynamics*. Cambridge: Cambridge University Press, 4th ed., 1981.

[26] P. A. T. 1933, *Physics for scientists and engineers*. W. H. Freeman and Company Worth Publications, fourth edition ed., 1999.

[27] D. L. Landau and E. M. Lifshitz, *The Quasi-Classical Case*, pp. 164–198. Quantum Mechanics (Non-relativistic Theory) Volume 3, Linacre House, Jordan Hill, Oxford, OX2 8DP: Butterworth-Heinemann, third ed., 1977.

[28] C. Kittel, *Quantum Theory of Solids*. Chichester: John Wiley and Sons, 2nd edition ed., 1987.

[29] W. Greiner, *Quantum Mechanics an Introduction*. Berlin: Springer, 3rd ed., 1998.

[30] D. J. Griffiths and D. F. Schroeter, *Introduction to Quantum Mechanics*. Harlow: Pearson, 3rd ed., 2013.

[31] S. Blundell, *Magnetism in condensed matter*. Oxford University Press, 2001.

[32] L. H. Ryder, *Quantum Field Theory*. Cambridge: Cambridge University Press, second ed., 1996.

[33] J. Minns, *Electron Monopole interactions Along a 2 Dimensional Plane*. University of Kent Masters Thesis supervised by J. Quntanilla, 2017.

[34] J. M. Cassels, *Basic Quantum Mechanics*. London [u.a.]: McGraw-Hill, second ed., 1970.

[35] P. Dirac, *The Principles of Quantum Mechanics*. Oxford: Clarendon Press, fourth ed., 1981.

[36] T. L. Chow, *Classical mechanics*. CRC, second edition ed., 2013.

[37] G. J. Sussman and J. Wisdom, *Structure and interpretation of classical mechanics*. The MIT Press, second edition ed., 2014.

[38] P. N. Argyres, "The Bohr-Sommerfeld quantization rule and the Weyl correspondence," *Physics Physique*, vol. 2, no. 3, pp. 131–139, 1965.

[39] A. S. Tarnovskii, "The Bohr-Sommerfeld quantization rule and quantum mechanics," *Soviet Physics Uspekhi*, vol. 33, no. 1, pp. 86–86, 1990.

[40] R. Cushman and J. Sniatycki, "On Bohr-Sommerfield-Heisenberg quantization," *Journal of Geometry and Symmetry in Physics*, vol. 35, pp. 11–19, 2014.

[41] R. Eisberg and R. Resnick, *Interpretation of the Quantization Rules, Sommerfields Model*, pp. 110–116. Quantum Physics of Atoms, Molecules, Solids, Nuclei, and Particles, Canada: John Wiley and Sons, second ed., 1985.

[42] J. Robbin and D. Salamon, "The Maslov index for paths," *Topology*, vol. 32, no. 4, pp. 827–844, 1993.

[43] R. Gautreau and W. Savin, *Schaum's outline of theory and problems of modern physics*. McGraw-Hill, second edition ed., 1999.

[44] A. Zangwill, *Modern Electrodynamics*. United States of America: Cambridge University Press, first ed., 2013.

[45] G. Paz, "The non-self-adjointness of the radial momentum operator in n dimensions," *Journal of Physics A: Mathematical and General*, vol. 35, 9 2000.

[46] G. Paz, "On the connection between the radial momentum operator and the hamiltonian in n dimensions," *European Journal of Physics*, vol. 22, 9 2000.

[47] B. H. Bransden and C. J. Joachain, *8 Approximation Methods for Stationary Systems, 8.4 The WKB approximation*, pp. 408–419, 783–785. Quantum Mechanics, Edinburgh Gate, Harlow, Essex, CM20 2JE: Pearson Education Ltd, second ed., 2000.

[48] J. G. Simmonds and J. E. M. Jr, *The WKB Approximation*, pp. 71–80. A First Look at Perturbation Theory, Mineola, NewYork: Dover Publications , INC, second ed., 1998.

[49] P. M. Morse and W. Allis, "The effect of exchange on the scattering of slow electrons from atoms," *Physical Review*, vol. 44, 8 1933.

[50] M. P. Morse and W. P. Allis, "The effect of exchange on the scattering of slow electrons from atoms," *Physical Review*, vol. 44, no. 4, pp. 269–276, 1933.

[51] L. Landau, E. Lifshitz, and L. Pitaevskii, *Electrodynamics of Continuous Media*, vol. Eight. Elsevier, second ed., 2008.

[52] S. Galtier, *Introduction to Modern Magnetohydrodynamics*. Cambridge University Press, 2016.

[53] N. Murphy, "Introduction to magnetohydrodynamics," 7 2015. Available at https://lweb.cfa.harvard.edu/~namurphy/Presentations/Introduction_to_MHD.pdf.

[54] E. R. Priest, "Magnetohydrodynamics: Overview," 2020. Avaliable at https://oxfordre.com/physics/view/10.1093/acrefore/9780190871994.001.0001/acrefore-9780190871994-e-6.

[55] Z. Yang, Z. Hussain, A. Hussanan, S. Hussain, and H. Zhang, "Instability of magnetohydrodynamic flow of hartmann layers between parallel plates," *AIP Advances*, vol. 9, p. 055003, 5 2019.

[56] O. G. W. Cassells, T. Vo, A. Pothérat, and G. J. Sheard, "From three-dimensional to quasi-two-dimensional: transient growth in magnetohydrodynamic duct flows," *Journal of Fluid Mechanics*, vol. 861, pp. 382–406, 2019.

[57] U. Müller and L. Bühler, *Analytical solutions for MHD channel flow*, pp. 37–55. Springer Berlin Heidelberg, 2001.

[58] G. Ruess and F. Vogt, "Höchstlamellar carbon from graphite oxyhydroxide.," *Monatshefte für Chemie*, vol. 78, pp. 222–242, 1948.

[59] K. S. Novoselov, A. K. Geim, S. V. Morozov, D. Jiang, Y. Zhang, S. V. Dubonos, I. V. Grigorieva, and A. A. Firsov, "Electric field effect in atomically thin carbon films," *Science*, vol. 306, pp. 666–669, 10 2004. doi: 10.1126/science.1102896.

[60] X. Deng, H. Chen, and Z. Yang, "Two-dimensional silicon nanomaterials for optoelectronics," *Journal of Semiconductors*, vol. 44, 2023.

[61] H. D. Young and R. A. Freedman, *University Physics*, vol. Two. Pearson, fourteenth ed., 2016.

[62] M. P. Marder, *Condensed matter physics*. Wiley, second edition ed., 2010.

[63] M. Alonso and E. J. Finn, *Physics*. Addison Wesley, 1992.

[64] J. Breithaupt, *Pagrave foundations: Physics*. Palgrave Macmillan, third edition ed., 2010.

[65] E. A. Witalis, "Hall magnetohydrodynamics and its applications to laboratory and cosmic plasma," *IEEE Transactions on Plasma Science*, vol. 14, pp. 842–848, 1986.

[66] L. Landau and E. Lifshitz, *Fluid Mechanics*, vol. Sixth. Elsevier, second ed., 2009.

[67] N. A. Mohamed, "Solving one- and two-dimensional unsteady burgers' equation using fully implicit finite difference schemes," *Arab Journal of Basic and Applied Sciences*, vol. 26, pp. 254–268, 1 2019. doi: 10.1080/25765299.2019.1613746.

[68] P. S. Bernard, *Fluid Dynamics*. Cambridge University Press, 2015.

[69] N. W. Ashcroft and N. D. Mermin, *Solid State Physics*. Belmont: Brookes/Cole CENGAGE Learning, 1st edition ed., 1976.

[70] D. V. Schroeder, *An introduction to thermal physics*. Addison Wesley Longman, 2000.

[71] R. Baierlein, *Thermal physics*. Cambridge University Press, 1999.

[72] P. Strange, *Relativistic quantum mechanics : with applications in condensed matter and atomic physics*. Cambridge University Press, 1998.

[73] H. H. Versteeg and W. Malalasekeram, *An introduction to computational fluid dynamics : the finite volume method*. Pearson India Education Services, second edition ed., 2007.

[74] A. Waman, *Introduction to computational fluid dynamics*. Cambridge University Press, 2005.

[75] J. Braithwaite, *Magnetohydrodynamics: equations and basic concepts*, pp. 8–1 to 8–16. Morgan and Claypool Publishers, 2017.

[76] T. E. Faber, *Fluid dynamics for physicists*. C.U.P., 1995.

[77] D. Acheson, *Elementary fluid dynamics*. Clarendon Press, 1990.

[78] F. White, *ISE Fluid Mechanics*. McGraw-Hill, 9th edition ed., 2021.

[79] J. F. Douglas, *Fluid mechanics*. Prentice Hall, 6th ed ed., 2011.

[80] Y. A. Cengel and J. M. Cimbala, *Fluid Mechanics: Fundamentals and Applications*, vol. 1. McGraw Hill Education, fourth ed., 20181.

[81] K. Kim, J.-Y. Choi, T. Kim, S. Cho, and H. Chung, "A role for graphene in silicon-based semiconductor devices," *Nature*, vol. 479, pp. 338–344, 2011.

[82] F. Schwierz and J. Pezoldt, "Device concepts using two-dimensional electronic materials: Graphene, mos2, etc," *2012 IEEE 11th International Conference on Solid-State and Integrated Circuit Technology*, pp. 1–4, 2012.

[83] M. Web, "Matweb material property data: Silicon," 2024. Avaliable at `https://www.matweb.com/search/DataSheet.aspx?MatGUID=7d1b56e9e0c54ac5bb9cd433a0991e27`, last accessed 18/03/24.

[84] L. T. Chemistry, "Properties of gallium arsenide." Avaliable at https://chem.libretexts.org/Bookshelves/Inorganic_Chemistry/Chemistry_of_the_Main_Group_Elements_(Barron)/06%3A_Group_13/6.11%3A_Properties_of_Gallium_Arsenide, last accessed 17/04/2024.

[85] A. Ambrosi, C. K. Chua, A. Bonanni, and M. Pumera, "Electrochemistry of graphene and related materials," *Chemical Reviews*, vol. 114, pp. 7150–7188, 7 2014. doi: 10.1021/cr500023c.

[86] P. P. Altermatt, A. Schenk, F. Geelhaar, and G. Heiser, "Reassessment of the intrinsic carrier density in crystalline silicon in view of band-gap narrowing," *Journal of Applied Physics*, vol. 93, pp. 1598–1604, 2 2003.

[87] A. B. Sproul and M. A. Green, "Improved value for the silicon intrinsic carrier concentration from 275 to 375 k," *Journal of Applied Physics*, vol. 70, pp. 846–854, 7 1991.

[88] University Berkeley, "Carrier concentrations." Avaliable at https://inst.eecs.berkeley.edu/~ee105/fa05/handouts/discussions/Discussion1.pdf#:~:text=Simply%2C%20ni%20%3Aintrinsic%20carrier%20concentration%2C%20which%20refers%20to,x%20106%20cm-3%20Germanium%202.4%20x%201013%20cm-3, last accessed 17/04/2024.

[89] J.-H. Chen, C. Jang, S. Xiao, M. Ishigami, and M. S. Fuhrer, "Intrinsic and extrinsic performance limits of graphene devices on sio2," *Nature Nanotechnology*, vol. 3, pp. 206–209, 2008.

[90] K. S. Novoselov, A. K. Geim, S. V. Morozov, D. Jiang, M. I. Katsnelson, I. V. Grigorieva, S. V. Dubonos, and A. A. Firsov, "Two-dimensional gas

of massless Dirac fermions in graphene," *Nature*, vol. 438, pp. 197–200, 11 2005.

[91] European Space Agency ESA, "Esa earth online visuals," 2024. Available at `https://visuals.earth.esa.int/data`, last accessed 05/04/2024.

[92] D. Collomb, P. Li, and S. J. Bending, "Nanoscale graphene Hall sensors for high-resolution ambient magnetic imaging," *Scientific Reports*, vol. 9, p. 14424, 2019.

[93] S. Entler, I. Duran, K. Kovarik, P. Sladek, O. Grover, M. Vilemova, D. Najman, M. Kohout, J. Sebek, K. Vyborny, and Z. Soban, "Temperature dependence of the hall coefficient of sensitive layer materials considered for demo hall sensors," *Fusion Engineering and Design*, vol. 153, p. 111454, 2020.

[94] B. N. Narozhny, I. V. Gornyi, A. D. Mirlin, and J. Schmalian, "Hydrodynamic approach to electronic transport in graphene," *Annalen der Physik*, vol. 529, p. 1700043, 11 2017.

[95] B. Narozhny, "Hydrodynamic approach to two-dimensional electron systems," *La Rivista del Nuovo Cimento*, vol. 45, 7 2022.

[96] D. A. Bandurin, I. Torre, R. K. Kumar, M. B. Shalom, A. Tomadin, A. Principi, G. H. Auton, E. Khestanova, K. S. Novoselov, I. V. Grigorieva, L. A. Ponomarenko, A. K. Geim, and M. Polini, "Negative local resistance caused by viscous electron backflow in graphene," *Science*, vol. 351, pp. 1055–1058, 3 2016. doi: 10.1126/science.aad0201.

[97] A. Lucas and K. C. Fong, "Hydrodynamics of electrons in graphene," *Journal of Physics: Condensed Matter*, vol. 30, p. 053001, 2018.

[98] B. F. Hamfeldt and J. Lesniewski, "Convergent finite difference methods for fully nonlinear elliptic equations in three dimensions," *Journal of Scientific Computing*, vol. 90, p. 35, 2021. Avaliable at https://doi.org/10.1007/s10915-021-01714-6, last accessed 21/03/2024.

[99] C. R. Maliska, *The Finite Volume Method*, pp. 41–83. Springer International Publishing, 2023.

[100] S. Chen and G. D. Doolen, "Lattice boltzmann method for fluid flows," *Annual Review of Fluid Mechanics*, vol. 30, pp. 329–364, 1 1998.

[101] A. J. Wagner, "A practical introduction to the lattice boltzmann method," 2008.

[102] H. Gould and J. Tobochnik, *An Introduction to Computer Simulation Mathods: Applications to physical Systems*. Addison-Wesley, 1988.

[103] A. Roman, "Lattice boltzmann," 2017. Avaliable at https://github.com/aromanro/LatticeBoltzmann, last accessed 21/03/2024.

[104] BMI Surplus Inc., "Keithley 177 microvolt." Avaliable at https://bmisurplus.com/product/keithley-177-microvolt-dmm-2/, last accessed 09/09/2024.

[105] MoDEL Collaboration, "Cern-moedal," 2024. Avaliable at https://home.web.cern.ch/science/experiments/moedal-mapp, last accessed 23/09/2024.

[106] ATLAS Collaboration, "Quest for curious magnetic monopoles continues," 8 2023. Avaliable at https://atlas.cern/Updates/Physics-Briefing/Run2-Monopoles, last accessed 23/09/2024.

[107] M. Ambrosio et al, "The performance of macro liquid scintillator in the search for magnetic monopoles," *Astroparticle Physics*, vol. 6, pp. 113–128, 1997.

[108] M. Ambrosio et al, "The macro detector at gran sasso," *Nuclear Instruments and Methods in Physics Research Section A: Accelerators, Spectrometers, Detectors and Associated Equipment*, vol. 486, pp. 663–707, 2002.

[109] R. L. Workman et al, "Review of particle physics: 95. magnetic monopoles," *PTEP*, vol. 2022, p. 083C01, 2022. Avaliable at `https://pdg.lbl.gov/2022/reviews/contents_sports.html`, last accessed 23/09/2024.

[110] J. Binney and S. Tremaine, *Galactic dynamics*. Princeton University Press, second edition ed., 2008.

[111] P. Virtanen, R. Gommers, T. E. Oliphant, M. Haberland, T. Reddy, D. Cournapeau, E. Burovski, P. Peterson, W. Weckesser, J. Bright, S. J. van der Walt, M. Brett, J. Wilson, K. J. Millman, N. Mayorov, A. R. J. Nelson, E. Jones, R. Kern, E. Larson, C. J. Carey, İ. Polat, Y. Feng, E. W. Moore, J. VanderPlas, D. Laxalde, J. Perktold, R. Cimrman, I. Henriksen, E. A. Quintero, C. R. Harris, A. M. Archibald, A. H. Ribeiro, F. Pedregosa, P. van Mulbregt, and SciPy 1.0 Contributors, "SciPy 1.0: Fundamental Algorithms for Scientific Computing in Python," *Nature Methods*, vol. 17, pp. 261–272, 2020.

[112] N. Drakos and R. Kobes, "Electrons as de broglie waves," 1999. Avaliable at `https://theory.uwinnipeg.ca/mod_tech/node149.html`, last accessed 17/01/2025.

[113] E. Merzbacher, *Quantum Mechanics*. New York: John Wiley and Sons,

2 ed., 1998.

[114] M. Jammer, *The conceptual development of quantum mechanics*. Los Angeles: Tomash, 1 ed., 1989.

[115] S. Weinberg, *Lectures on quantum mechanics*. Cambridge: Cambridge University Press, 2 ed., 2018.

[116] F. A. Buot, A. R. Elnar, G. Maglasang, and R. E. S. Otadoy, "On quantum Hall effect, Kosterlitz-Thouless phase transition, Dirac magnetic monopole, and Bohr–Sommerfeld quantization," *Journal of Physics Communications*, vol. 5, p. 025007, 2021.

[117] A. M. Ishkhanyan and V. P. Krainov, "Maslov index for power-law potentials," *JETP Letters*, vol. 105, no. 1, pp. 43–46, 2017.

[118] J. B. Keller, "Corrected Bohr-Sommerfeld quantum conditions for nonseparable systems," *Annals of Physics*, vol. 4, no. 2, pp. 180–188, 1958.

[119] H. J. W. Müller-Kirsten, *Introduction to quantum mechanics*. Singapore: World Scientific, 1 ed., 2012.

[120] R. B. Dingle, *Asymtopic Expansions: Their Derivation and Interpretation*. London/New York: Academic Press, 1 ed., 1973.

[121] H. J. W. Müller-Kirsten, *Introduction to quantum mechanics : Schrödinger equation and path integral*. World Scientific, second edition ed., 2012.

[122] R. B. White, *Asymptotic Analysis of Differential Equations*. IMPERIAL COLLEGE PRESS, 8 2010. doi:10.1142/p735.

[123] Q. Kong, T. Siauw, and A. Bayen, *Python Programming and Numerical Methods*. Academic Press, first ed., 2020.

[124] P. Zhou, *Finite Difference Method*, pp. 63–94. Springer Berlin Heidelberg, 1993.

[125] L. Pipes and L. Harvill, *Applied Mathematics for Engineers and Physicists*. Dover Publishing, third ed., 2014.

[126] E. Kreyszig, *Advanced Engineering Mathematics*. John Wiley and Sons, tenth ed., 2011.

[127] S. B. Kenneth Riley and M. Hobson, *Mathematical methods for physics and engineering : a comprehensive guide*. Cambridge University Press, 1997.

Appendix A

Methodologies

A.1 Lagrangian Mechanics

The Lagrangian is defined as [110]

$$L = T - V, \tag{A.1}$$

where T is the kinetic energy of the system and V is the potential energy of the system. Since the Lagrangian only concerns the energy of a system and is a scalar, whereas a Newtonian description would require a vector based system of equations, Lagrangian mechanics can simplify the modelling of the problem. Applying the Lagrangian to the Euler-Lagrange equation [36, 37] gives

$$\frac{\partial L}{\partial q} - \frac{\partial}{\partial t}\frac{\partial L}{\partial \dot{q}} = 0. \tag{A.2}$$

Solving the Euler-Lagrange equation for each degree of freedom will garner equations of motion for the system being investigated. For the classical analysis of an electron orbiting about a position above a magnetic monopole the solutions are a pair of coupled equations of motion. One equation de-

scribing the radial component and another describing the polar motion of the electron. Solving this was done by setting up the coupled equations and with the scipy odeint [111] function over a given time period. The initial conditions for the calculation are dependent on the choice of coordinates of the electron at the beginning of the calculation (it cannot be in a classically disallowed region of the classical potential, see Fig. 3.1) and the chosen energy of the electron. The initial coordinates and the energy dictate the electron's beginning radial and tangential velocities for the initial conditions.

A.2 Bohr-Sommerfeld Quantisation

The number of De-Broglie wavelengths, λ_{DB}, around a circular path has to be an integer value [112]

$$\oint \frac{1}{\lambda_{DB}} dq = n, \tag{A.3}$$

where $n = 1, 2, 3$ and q is the relevant coordinate. Substituting $\lambda_{DB} = h/p$, where h is Planck's constant and p is the momentum of a particle gives

$$\oint p_n dq = nh. \tag{A.4}$$

The momentum can be expressed as $p_n = \sqrt{2m(E_n - V(q))}$, with m, E_n and $V(q)$ being the mass the energy and potential energy respectively. This derivation of Bohr-Sommerfeld quantisation is in agreement with [38–41,113–115]. The system we will be focusing on is integrable and as such will have a Bohr-Sommerfeld equations for each degree of freedom. The focus of these texts is to introduce Bohr-Sommerfeld quantisation in an historical context, namely as the first attempt to evaluate the energy levels of a hydrogen atom. Focusing on circular orbit, and later refined to elliptical orbits, the Bohr-Sommerfeld quantisation condition accurately predicted the energy levels

of a hydrogen atom before quantum mechanics. Errors occur when dealing with non-circular systems such as the harmonic oscillator. The Schrödinger equation evaluates energy levels of $E_n = (n + \frac{1}{2})\hbar\omega$, Bohr-Sommerfeld quantisation gives $E_n = n\hbar\omega$. The Bohr-Sommerfeld quantisation is wrong by an additive constant of $\frac{1}{2}\hbar\omega$.

References [27, 116] give the Bohr-Sommerfeld quantisation corrected with a γ term as

$$\oint P dq = (n + \gamma)\, h. \tag{A.5}$$

There are several methods to determine γ that can be applied to Bohr-Sommerfeld quantisation. These can be complex to utilise such as Maslov indexes [42, 117] or the Keller correction [118]. The method that I will introduce here is simpler and produces the correct answer for two turning points. For a given system the correction term should be the same regardless of which method has been used to calculate it.

A.2.1 The R.B. Dingle Correction

This correction is seen in [119] and is credited to R.B. Dingle. The author gives a book [120] (chapter 13) and a lecture he attended by Dingle as a source of the correction. The book cited has no reference to this correction that I have been able to find. A secondary source, [121], also refers to R.B. Dingle where the correction was learned via lecture, but has no written source for the correction. The corrected Bohr-Sommerfeld quantisation is given as

$$\oint P_n dq = \left[n + \frac{1}{4} \times \text{the number of turning points} \right] h. \tag{A.6}$$

Here the Maslov correction, γ, is $\gamma = \frac{1}{4} \times$the number of turning points. Here the turning points are determined by the classical trajectory of the particle. So for circular orbits there are no turning points so $\gamma = 0$. For a harmonic oscillator there are two turning points so the $\gamma = \frac{1}{2}$, which is correct. This fits the needs for the problem under consideration where we are considering the polar motion about the monopole and the radial motion which will be acting like a harmonic oscillator.

A.3 WKB approximation Applied to the Quantum Problem

The derivation used here is of second order; higher orders can be chosen for more accuracy but at an increased computational cost. Using the methods described in [27,47,48] the following derivation is performed. Starting from the Schrödinger equation scaled by the factors found in Section 2.1 we get a dimensionless Schrödinger equation

$$-\frac{\partial^2 \psi(\rho)}{\partial \rho^2} + (V(\rho) - \epsilon)\,\psi(\rho) = 0. \tag{A.7}$$

Eq. (A.7) is not suitable for WKB expansion in its current form as it lacks a smallness factor, ω^2, that is required to complete the expansion of trial solutions around it (ω^2) as described by [48]. In a dimension-full Schrödinger equation the smallness factor would have been $\hbar$. The following adaptation can be made (then removed at a latter stage of the derivation returning the original equation [27,47])

$$-\omega^2 \frac{\partial^2 \psi(\rho)}{\partial \rho^2} + (V(\rho) - \epsilon)\,\psi(\rho) = 0. \tag{A.8}$$

Trying a trial solution of $\psi(\rho) = \exp\left(\frac{i}{\omega}S(\rho)\right)$ and substituting into equation Eq. (A.8) gives

$$-\omega^2\left(\frac{i}{\omega}S''(\rho) - \frac{1}{\omega^2}S'(\rho)^2\right) + (V(\rho) - \epsilon) = 0. \tag{A.9}$$

Expanding $S(\rho)$ as a power series up to the second term gives the results:

$$S(\rho) = S_0(\rho) + \omega S_1(\rho), \tag{A.10}$$

$$S'(\rho) = S_0'(\rho) + \omega S_1'(\rho), \tag{A.11}$$

$$S'(\rho)^2 = S_0'(\rho)^2 + \omega^2 S_1'(\rho)^2 + 2\omega S_0'(\rho)S_1'(\rho), \tag{A.12}$$

$$S''(\rho) = S_0''(\rho) + \omega S_1''(\rho). \tag{A.13}$$

Substituting Eqs. (A.10) to (A.13) into Eq. (A.9) and collecting the coefficients of the terms ω^0 and ω^1 gives the following equations:

$$S_0'(\rho)^2 + (V(\rho) - \epsilon) = 0, \tag{A.14}$$

$$2S_0'(\rho)S_1'(\rho) - iS_0''(\rho) = 0. \tag{A.15}$$

Evaluating the Eq. (A.14), assuming $\epsilon > V(\rho)$, gives $S_0(\rho)$

$$S_0(\rho) = \pm\int^{\rho} P(\rho')d\rho' \quad \text{where} \quad P(\rho) = \sqrt{\epsilon - V(\rho)}. \tag{A.16}$$

Substituting Eq. (A.16) into Eq. (A.15) gives the following solution

$$S_1(\rho) = \frac{i}{2}\ln(P(\rho)). \tag{A.17}$$

Putting both Eq. (A.16) and Eq. (A.17) into Eq. (A.10)

$$S(\rho) = \pm \int^{\rho} P(\rho')dx' + \frac{i\omega}{2} \ln(P(\rho)), \tag{A.18}$$

then substituting into the solution $\psi(\rho) = \exp\left(\frac{i}{\omega}S(\rho)\right)$ gives

$$\psi(\rho) = \frac{1}{\sqrt{|P(\rho)|}} \exp\left(\pm\frac{i}{\omega}\int^{\rho} P(\rho')dx'\right). \tag{A.19}$$

Which can be expressed as a general solution in the form for $\epsilon > V(\rho)$

$$\psi(\rho) = \frac{1}{\sqrt{|P(\rho)|}}\left[A\exp\left(\frac{i}{\omega}\int^{\rho} P(\rho')dx'\right) + B\exp\left(-\frac{i}{\omega}\int^{\rho} P(\rho')dx'\right)\right]. \tag{A.20}$$

Comparing Eq. (A.7) and Eq. (A.8) it is seen that $\omega = 1$. So the general solution to Eq. (A.7) for $\epsilon > V(\rho)$ is given by

$$\psi(\rho) = \frac{1}{\sqrt{|P(\rho)|}}\left[A\exp\left(i\int^{\rho} P(\rho')dx'\right) + B\exp\left(-i\int^{\rho} P(\rho')dx'\right)\right]. \tag{A.21}$$

The process can then be repeated for $\epsilon < V(\rho)$ giving the general solution of

$$\psi(\rho) = \frac{1}{\sqrt{|P(\rho)|}}\left[C\exp\left(\int^{\rho} P(\rho')dx'\right) + D\exp\left(-\int^{\rho} P(\rho')dx'\right)\right]. \tag{A.22}$$

A.3.1 Joining the Components of the Wavefunction

Here I will describe the connection formulas used to join one section of the WKB approximation to another section. At a turning point the WKB approximation breaks down, the turning points occur when classically the momentum of the particle is 0, which is where $\epsilon = v(\rho)$. When moving from a classically allowed region to a disallowed region the wave function changes

from a sinusoidal function to an exponential function. This describes the Airy A and B functions. Following the derivation from [47], assuming very near the turning point the potential is approximately linear, the time independent Schrödinger equation is

$$\left(\frac{d^2}{d\rho^2} + \omega^{-2}P^2(\rho)\right)\psi(\rho) = 0, \tag{A.23}$$

where we have expressed it in dimensionless terms as used previously. The momentum at the turning points is described by

$$P^2(\rho) \approx A(\rho - \rho_1), \tag{A.24}$$

A is a positive constant and ρ_1 is the turning point, giving values of $P^2(\rho) > 0$ for $\rho > \rho_1$ and $P^2(\rho) < 0$ for $\rho < \rho_1$.The Schrödinger equation, Eq. (A.23), can be rewritten as

$$\left(\frac{d^2}{dq^2} + q\right)\psi(q) = 0, \tag{A.25}$$

where q is a function of ρ given by $q(\rho) = \left(\omega^{-2}A\right)(\rho - \rho_1)$. This gives the solution to the Schrödinger equation near the turning points as

$$\psi(q) = CAi(-q) + DBi(-q), \tag{A.26}$$

where C and D are arbitrary constants. The approximate Airy functions solutions [47, 122] are

$$\begin{aligned} Ai(q) &\approx \pi^{-\frac{1}{2}} q^{-\frac{1}{4}} \cos\left(\frac{2}{3}q^{\frac{3}{2}} - \frac{\pi}{4}\right) && \text{for} \quad q \to \infty, \\ Ai(q) &\approx \frac{1}{2}\pi^{-\frac{1}{2}}|q|^{-\frac{1}{4}} \exp\left(\frac{2}{3}|q|^{\frac{3}{2}}\right) && \text{for} \quad q \to -\infty, \end{aligned} \tag{A.27}$$

$$
\begin{aligned}
Bi(q) &\approx -\pi^{-\frac{1}{2}} q^{-\frac{1}{4}} \sin\left(\frac{2}{3}q^{\frac{3}{2}} - \frac{\pi}{4}\right) \qquad \text{for} \quad q \to \infty, \\
Bi(q) &\approx \pi^{-\frac{1}{2}} |q|^{-\frac{1}{4}} \exp\left(-\frac{2}{3}|q|^{\frac{3}{2}}\right) \qquad \text{for} \quad q \to -\infty.
\end{aligned}
\tag{A.28}
$$

Applying the WKB approximation to the Schrödinger equation, Eq. (A.25), gives the result

$$
\psi(q) = N_{\pm} \left(|q(\rho)|\right)^{-\frac{1}{4}} \exp\left(\pm i \frac{2}{3}[q(\rho)]^{\frac{3}{2}}\right). \tag{A.29}
$$

Here $N_{\pm}$ is an arbitrary constant which varies depending on whether the exponential term is positive or negative. Comparing this solution to the solution of the Schrödinger equation Eq. (A.23)

$$
\psi(\rho) = N_{\pm} \left(|p^2(\rho)|\right)^{-\frac{1}{4}} \exp\left(\pm \int_{\rho_1}^{\rho} p(\rho')d\rho'\right), \tag{A.30}
$$

where $\omega = 1$ to remove the smallness factor giving the solution to the dimensionless equation. Comparing these equations it can be seen that

$$
\frac{2}{3}\left[q(\rho)\right]^{\frac{3}{2}} = \int_{\rho_1}^{\rho} p(\rho')d\rho'. \tag{A.31}
$$

Using this result and the approximate definitions of the Airy functions the connection formulae can be derived. In a potential well there are two turning points that mark the transition from the classically allowed region to the disallowed region. Naturally we can approach a turning point form either direction mathematically but a transition occurs moving from an exponential solution in the classically forbidden region into a sinusoidal solution for a classically allowed region and vice versa. Comparing the airy function approximations for the limits of $\rho \to \infty$ and $\rho \to -\infty$, Eq. (A.27) and Eq. (A.28), at the turning point the two components of Airy Ai must be equal to one another the same is true for Airy Bi. So, for a turning point ρ_1,

on the left hand side, we can see that the solution must make the connection across the turning point in the following manner

$$\frac{1}{\sqrt{|P(\rho)|}} \exp\left[\int_{\rho_1}^{\rho} |P(\rho')|\, d\rho'\right] \rightarrow \frac{2}{\sqrt{|P(\rho)|}} \cos\left[\int_{\rho_1}^{\rho} P(\rho') d\rho' - \frac{\pi}{4}\right], \quad \text{(A.32)}$$

$$-\frac{1}{\sqrt{|P(\rho)|}} \exp\left[-\int_{\rho_1}^{\rho} |P(\rho')|\, d\rho'\right] \leftarrow \frac{1}{\sqrt{|P(\rho)|}} \sin\left[\int_{\rho_1}^{\rho} P(\rho') d\rho' - \frac{\pi}{4}\right], \quad \text{(A.33)}$$

where on the left hand side $\rho < \rho_1$ and on the right hand side $\rho > \rho_1$. Eq. (A.32) is derived from the Airy A approximation and Eq. (A.33) is derived from the Airy B approximation. For a turning point, ρ_2, on the right hand side

$$\frac{2}{\sqrt{|P(\rho)|}} \cos\left[-\int_{\rho_2}^{\rho} P(\rho') d\rho' - \frac{\pi}{4}\right] \leftarrow \frac{1}{\sqrt{|P(\rho)|}} \exp\left[-\int_{\rho_2}^{\rho} |P(\rho')|\, d\rho'\right], \quad \text{(A.34)}$$

$$\frac{1}{\sqrt{|P(\rho)|}} \sin\left[-\int_{\rho_2}^{\rho} P(\rho') d\rho' - \frac{\pi}{4}\right] \rightarrow -\frac{1}{\sqrt{|P(\rho)|}} \exp\left[\int_{\rho_2}^{\rho} |P(\rho')|\, d\rho'\right], \quad \text{(A.35)}$$

where on the left hand side $\rho > \rho_2$ and on the right hand side $\rho < \rho_2$. Eq. (A.34) is derived from the Airy A approximation and Eq. (A.35) is derived from the Airy B approximation. It must also be noted that these connection formulae are directional and dimensionless.

A.4 Finite Difference Method

I wish to discretise an eigenvalue problem containing differential operators so that it can be solved numerically [123,124]. A trial function of $f(x)$ is what I wish to differentiate, performing a Taylor series expansion of $f(x+\Delta x)$ and

$f(x - \Delta x)$ to $O(\Delta x^2)$ gives respectively

$$f(x + \Delta x) = f(x) + \Delta x f'(x) + \frac{\Delta x^2 f''(x)}{2!}, \tag{A.36}$$

and

$$f(x - \Delta x) = f(x) - \Delta x f'(x) + \frac{\Delta x^2 f''(x)}{2!}. \tag{A.37}$$

Looking at Eq. (A.36) and Eq. (A.37), ignoring any terms with an order higher than Δx, we arrive at a forwards and backwards finite differences definitions of a first order derivative by rearranging for $f'(X)$. In the forward finite difference the functions of the numerator are between x and a forward point of $x + \Delta x$. The backwards finite difference: the difference is between a function at point x and one at point $x - \Delta x$. The forwards and backwards finite differences are respectively

$$f'(x) \approx \frac{f(x + \Delta x) - f(x)}{\Delta x}, \tag{A.38}$$

$$f'(x) \approx \frac{f(x) - f(x - \Delta x)}{\Delta x}. \tag{A.39}$$

A central finite difference regime can be obtained by evaluating $f(x + \Delta x) - f(x - \Delta x)$ and rearranging for $f'(x)$

$$f'(x) \approx \frac{f(x + \Delta x) - f(x - \Delta x)}{2\Delta x}. \tag{A.40}$$

The central finite difference is a difference in the terms of the numerator about $f(x)$ with a positional difference of $\pm\Delta x$.

To solve the Schrödinger equation the second order differential is required, this can be evaluated in finite difference form by summing Eq. (A.36) and

Eq. (A.37) and rearranging for $f''(x)$

$$f''(x) \approx \frac{f(x-\Delta x) - 2f(x) + f(x+\Delta x)}{\Delta x^2}. \tag{A.41}$$

A.5 4th Order Runge-Kutta Method

The 4th order Runge-Kutta method [125–127] can be used to solve first order differential equations of the form

$$\frac{dy}{dx} = f(x, y), \tag{A.42}$$

where f is a function of x and y. The approach is iterative with a variable step size, h. Starting from a value y_i (where the subscript i indicates the iterative step count) the subsequent value y_{i+1} can be evaluated using

$$y_{i+1} = y_i + \frac{1}{6}\left(k_1 + 2k_2 + 2k_3 + k_4\right), \tag{A.43}$$

where

$$k_1 = hf\left(x_i, y_i\right), \tag{A.44}$$

$$k_2 = hf\left(x_i + \frac{1}{2}h, y_i + \frac{1}{2}k_1\right), \tag{A.45}$$

$$k_3 = hf\left(x_i + \frac{1}{2}h, y_i + \frac{1}{2}k_2\right), \tag{A.46}$$

$$k_4 = hf\left(x_i + h, y_i + k_3\right). \tag{A.47}$$

The smaller the h that is chosen; the greater the accuracy of the results, but at the cost of computation time.

Appendix B

Changing From Cartesian to Polar Coordinates in Two Dimensions

The difference between the classical and quantum potentials is due to how the change in coordinates of the Schrödinger equation is being carried out. The first method starts with a two-dimensional Cartesian classical Hamiltonian and transforming into polar coordinates:

$$H = T + V = \frac{1}{2m}\left(P_x^2 + P_y^2\right) + V = \frac{1}{2m}\left(m\dot{x}^2 + m\dot{y}^2\right) + V. \tag{B.1}$$

Using $x = r\cos\left(\phi\right)$ and $y = r\sin\left(\phi\right)$ and differentiating with respect to time

$$\begin{aligned} \frac{dx}{dt} &= \dot{r}\cos\left(\phi\right) - r\dot{\phi}\sin\left(\phi\right), \\ \frac{dy}{dt} &= \dot{r}\sin\left(\phi\right) + r\dot{\phi}\cos\left(\phi\right), \end{aligned} \tag{B.2}$$

substituting these back into Eq. (B.1) gives:

$$H = \frac{1}{2m}\left(m\dot{r}^2 + mr^2\dot{\phi}^2\right) + V = \frac{1}{2m}\left(m\dot{r}^2 + \frac{mr^2v^2}{r^2}\right) + V. \tag{B.3}$$

where v is the tangential velocity to the radial position vector. $P_r = m\dot{r}$ and $P_\phi = mr^2v^2$ are the linear and orbital momentum these can be substituted in giving a final Hamiltonian:

$$H_{\text{polar}} = \frac{1}{2m}\left[P_r^2 + \frac{P_\phi^2}{r^2}\right] + V(r,\phi). \tag{B.4}$$

Using equation B.4 and assuming the identities $P_r = i\hbar\frac{\partial}{\partial r}$ and $P_\phi = i\hbar\frac{\partial}{\partial \phi}$ can be substituted into the classical Hamiltonian to create a quantum Hamiltonian we can form a Schrödinger equation, where ψ_c is the wave function, to obtain

$$-\frac{\hbar^2}{2m}\left[\frac{\partial^2}{\partial r^2} + \frac{1}{r^2}\frac{\partial^2}{\partial \phi^2}\right]\psi_c(r,\phi) + V(r,\phi)\psi_c(r,\phi) = E\psi_c(r,\phi). \tag{B.5}$$

The second method is to transform a Cartesian Schrödinger equation to a polar form directly, by transforming the variables in the Laplacian.

$$\begin{aligned} x &= r\cos(\phi), & y &= r\sin(\phi), \\ \frac{\partial x}{\partial r} &= \cos(\phi), & \frac{\partial y}{\partial r} &= \sin(\phi), \\ \frac{\partial x}{\partial \phi} &= -r\sin(\phi), & \frac{\partial y}{\partial \phi} &= r\cos(\phi), \end{aligned} \tag{B.6}$$

using a dummy function u we can use the chain rule to evaluate the change of u with respect to r

$$\frac{\partial u}{\partial r} = \frac{\partial u}{\partial x}\frac{\partial x}{\partial r} + \frac{\partial u}{\partial y}\frac{\partial y}{\partial r}. \tag{B.7}$$

Substituting in the relevant values from Eq. (B.6) gives:

$$\frac{\partial u}{\partial r} = \cos(\phi)\frac{\partial u}{\partial x} + \sin(\phi)\frac{\partial u}{\partial y}. \tag{B.8}$$

Now taking the second derivative of u with respect to r we get

$$
\begin{aligned}
\frac{\partial^2 u}{\partial r^2} &= \frac{\partial}{\partial r}\frac{\partial u}{\partial r}, \\
&= \frac{\partial x}{\partial r}\frac{\partial}{\partial x}\frac{\partial u}{\partial r} + \frac{\partial y}{\partial r}\frac{\partial}{\partial y}\frac{\partial u}{\partial r}, \\
&= \cos(\phi)\frac{\partial}{\partial x}\left(\cos(\phi)\frac{\partial u}{\partial x} + \sin(\phi)\frac{\partial u}{\partial y}\right) \\
&\qquad + \sin(\phi)\frac{\partial}{\partial y}\left(\cos(\phi)\frac{\partial u}{\partial x} + \sin(\phi)\frac{\partial u}{\partial y}\right), \\
&= \cos^2(\phi)\frac{\partial^2 u}{\partial x^2} + \sin^2(\phi)\frac{\partial^2 u}{\partial y^2} + 2\cos(\phi)\sin(\phi)\frac{\partial^2 u}{\partial x \partial y}. \qquad \text{(B.9)}
\end{aligned}
$$

Repeating this process but now taking the derivative of u with respect to ϕ

$$
\frac{\partial u}{\partial \phi} = \frac{\partial u}{\partial x}\frac{\partial x}{\partial \phi} + \frac{\partial u}{\partial y}\frac{\partial y}{\partial \phi}. \qquad \text{(B.10)}
$$

Once again substituting in the relevant values from Eq. (B.6) gives:

$$
\frac{\partial u}{\partial \phi} = -r\sin(\phi)\frac{\partial u}{\partial x} + r\cos(\phi)\frac{\partial u}{\partial y}. \qquad \text{(B.11)}
$$

Next taking the second derivative with respect to ϕ

$$
\begin{aligned}
\frac{\partial^2 u}{\partial \phi^2} &= \frac{\partial}{\partial \phi}\frac{\partial u}{\partial \phi}, \\
&= \frac{\partial x}{\partial \phi}\frac{\partial}{\partial x}\frac{\partial u}{\partial \phi} + \frac{\partial y}{\partial \phi}\frac{\partial}{\partial x}\frac{\partial u}{\partial \phi}, \\
&= -r\cos(\phi)\frac{\partial}{\partial x}\left(-r\sin(\phi)\frac{\partial u}{\partial x} + r\cos(\phi)\frac{\partial u}{\partial y}\right) \\
&\qquad + r\cos(\phi)\frac{\partial}{\partial y}\left(-r\sin(\phi)\frac{\partial u}{\partial x} + r\cos(\phi)\frac{\partial u}{\partial y}\right), \\
&= -r\left(\cos(\phi)\frac{\partial u}{\partial x} + \sin(\phi)\frac{\partial u}{\partial y}\right) - 2r^2\sin(\phi)\cos(\phi)\frac{\partial^2 u}{\partial x \partial y} \\
&\qquad + r^2\sin^2(\phi)\frac{\partial^2 u}{\partial x^2} + r^2\cos^2(\phi)\frac{\partial^2 u}{\partial y^2}. \qquad \text{(B.12)}
\end{aligned}
$$

Dividing $\partial^2 u/\partial\phi^2$ by r^2 and substituting in $\partial u/\partial r$

$$\frac{1}{r^2}\frac{\partial^2 u}{\partial\phi^2} = -\frac{1}{r}\frac{\partial u}{\partial r} - 2\sin(\phi)\cos(\phi)\frac{\partial^2 u}{\partial x\partial y} + \sin^2(\phi)\frac{\partial^2 u}{\partial x^2} + \cos^2(\phi)\frac{\partial^2 u}{\partial y^2}, \quad \text{(B.13)}$$

adding this to $\partial^2 u/\partial r^2$ gives:

$$\begin{aligned}\frac{\partial^2 u}{\partial r^2} + \frac{1}{r^2}\frac{\partial^2 u}{\partial\phi^2} = -\frac{1}{r}\frac{\partial u}{\partial r} + \sin^2\phi\frac{\partial^2 u}{\partial x^2} + \cos(\phi)\frac{\partial^2}{\partial y^2} \\ - 2\sin(\phi)\cos(\phi)\frac{\partial^2 u}{\partial x\partial y} + \cos^2(\phi)\frac{\partial^2 u}{\partial x^2} \\ + 2\sin(\phi)\cos(\phi)\frac{\partial^2 u}{\partial x\partial y} + \sin^2(\phi)\frac{\partial^2 u}{\partial y^2}, \quad \text{(B.14)}\end{aligned}$$

which can be rearranged as:

$$\frac{\partial^2 u}{\partial r^2} + \frac{1}{r}\frac{\partial u}{\partial r} + \frac{1}{r^2}\frac{\partial^2 u}{\partial\phi^2} = \frac{\partial^2 u}{\partial x^2} + \frac{\partial^2 u}{\partial y^2}. \quad \text{(B.15)}$$

Putting this into the Hamiltonian results in the following Schrödinger equation, where ψ_q is the wave function:

$$-\frac{\hbar^2}{2m}\left[\frac{\partial^2}{\partial r^2} + \frac{1}{r}\frac{\partial}{\partial r} + \frac{1}{r^2}\frac{\partial^2}{\partial\phi^2}\right]\psi_q(r,\phi) + V(r,\phi)\psi_q(r,\phi) = E\psi_q(r,\phi) \quad \text{(B.16)}$$

The difference between Eq. (B.5) and Eq. (B.16) is the additional term $r^{-1}\partial/\partial r$. The correct method is the second, performing the transform of variables in the Laplacian [45,46], in general an extra term will appear when performing the transformation in n dimensions with the exceptions being $n = 1$ or $n = 3$. The difference between the two methods also extends to the potential with both producing two different potentials with the correct one having a different form from its classical counterpart.

Appendix C

A Numerical Solution Utilising the Finite Differences Method

Using the finite difference method Appendix A.4, a numerical approach where the Schrödinger equation is diagonalised, [123], to solve for $\psi(\rho)$ and ϵ. The matrix version of the Schrödinger equation is

$$\left(-\frac{1}{h^2}\boldsymbol{T} + \boldsymbol{U}\right)\psi(\rho) = \epsilon\psi(\rho), \tag{C.1}$$

where $\boldsymbol{T}$ is the tridiagonal matrix corresponding to the discretization of second order derivative, $\boldsymbol{U}$ is the diagonalised $V_{\text{quantum}}(\rho)$, $\psi(\rho)$ is a vector of length N, where N is the number of discrete equal sized steps the vector is divided into. The step size, h, is given as $h = \frac{b-a}{N-1}$, where a and b are the

limits of ρ. The corresponding matrices take the form of

$$\left(\frac{1}{h^2} \begin{bmatrix} 2 & -1 & \cdots & \cdots & 0 \\ -1 & 2 & -1 & & \vdots \\ \vdots & & \ddots & & \vdots \\ \vdots & & -1 & 2 & -1 \\ 0 & \cdots & \cdots & -1 & 2 \end{bmatrix} + \begin{bmatrix} V_1 & \cdots & \cdots & \cdots & 0 \\ \vdots & V_2 & & & \vdots \\ \vdots & & \ddots & & \vdots \\ \vdots & & & V_{N-1} & \vdots \\ 0 & \cdots & \cdots & \cdots & V_N \end{bmatrix} \right) \begin{bmatrix} \psi_1 \\ \psi_2 \\ \vdots \\ \psi_{N-1} \\ \psi_N \end{bmatrix} = \epsilon \begin{bmatrix} \psi_1 \\ \psi_2 \\ \vdots \\ \psi_{N-1} \\ \psi_N \end{bmatrix}. \tag{C.2}$$

This numerical technique is arbitrarily accurate, a small step size increases the accuracy but also increases the computational power required to evaluate the solutions. The other limiting factor for this particular method is that the range of 0 to ρ that can examined. As the range is limited the potential is effectively sitting within an infinite square well with a width the range of ρ. There is a balancing act to be done here, choosing a range of ρ that is large enough to minimise any effects that the infinite well will have on the solutions. Choosing a larger range of ρ then requires reducing the step size to ensure that the solutions are accurate over the range.

The values of $N = 4000$, $a = 0$ and $b = 20$ are used to produce the wave functions and eigenvalues with this method. The limits $a = 0$ and $b = 20$ were chosen so as to allow a large enough range to avoid the infinite potential created by the limits a and b. This range ensures that the wavefunctions produced by the finite difference method are considered over the significant features of the potential. Cutting off the potential by the boundary forms a void of no eigenstates, this can be seen clearly in Fig. C.1, where the infinite potential well has cut off the potential of the monopole creating a band where there are no states. This is due to the two potentials producing a forbidden region where no quantum state can be formed. The step size, h, ideally is made as small as possible; when $\lim_{h \to 0}$ the finite difference returns

the accurate answer. Since I cannot computationally achieve an infinitesimal step size, we are hampered by zero division errors, a need to choose h to be small enough to be accurate, but large enough to be computable. Various different values of h with fixed parameters of $\lambda = 100$, $a = 0$ and $b = 20$ are explored in Table C.1. As h is decreased the energy eigenvalues begin to converge.

h	$n = 0$	$n = 1$	$n = 3$	$n = 4$	$n = 5$	$n = 6$	$n = 7$	$n = 8$
2/25	280.43	434.15	561.86	664.84	815.73	886.97	941.14	946.18
1/25	285.84	451.43	596.92	722.68	828.30	910.96	911.48	958.28
1/50	287.28	455.56	604.45	733.37	840.87	922.16	923.27	-
1/100	287.68	456.64	606.37	736.01	843.89	925.31	-	-
1/200	287.79	456.93	606.87	736.68	844.65	926.12	-	-
1/400	287.82	457.01	606.99	736.86	844.85	926.31	-	-

Table C.1: Energy eigenvalues for different step sizes, h and fixed range of $a = 0$ to $b = 20$ and $\lambda = 100$. We can see that the as step size is decreased the energy eigenvalues tend towards an accurate figure for this project. Additional eigenvalues are found for the $h = 2/25, 1/25$ and $1/50$. The additional states at $n = 7$ and $n = 8$ are due to the inaccuracy caused by the choice of step size. As step size is decreased these states no longer appear in the results.

The value of $N = 4000$ was chosen as this produced accurate results over the range and was computationally achievable. The results from this method produce a continuum of eigenstates, see Fig. C.1. This continuum of states contain all states that are quasi-bound and scattering. The scattering states have a negligible presence in the potential well, so the probability of an electron being found there is very small. The quasi-bound states have a large amplitude inside the well and a smaller amplitude outside of it. Since the wavefunction of the electron for these states is not zero outside of the well, the quasi-bound state will eventually decay in time, producing a scattering state for an infinite length ρ. Should ρ be finite in size (as I have been modelling) it can be seen over time the wavefunction bounces back inside the potential well and becomes once again quasi-bound, this is discussed in

section 6.2.

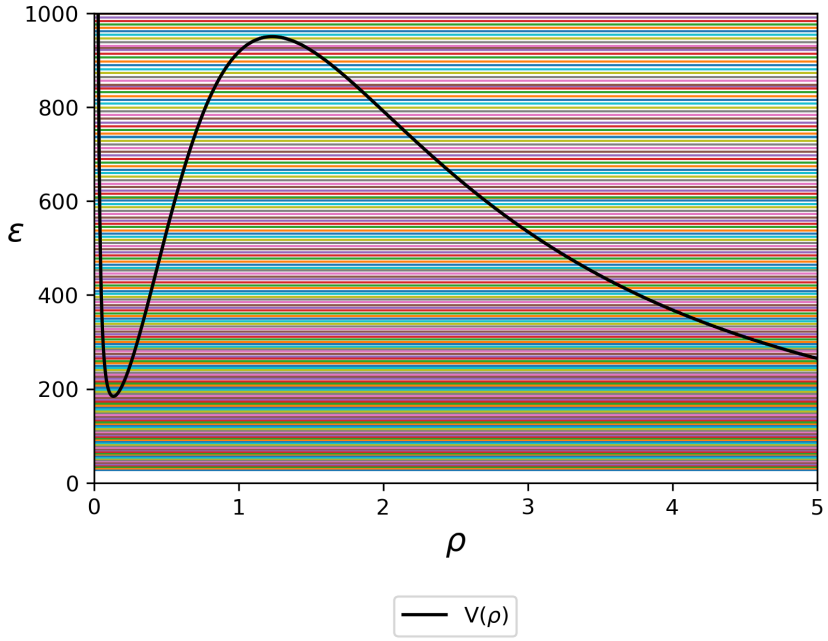

Figure C.1: The unfiltered wavefunctions for $M = 1$ and $\lambda = 100$. Filtering these wavefunctions for ones that have non-zero components inside of the potential well will reveal the quasi-bound eigenstates. The absence of wavefunctions at values of $\epsilon \approx< 30$ is due to the limitations of the computational model.

The results are filtered for eigenfunctions that have a non-zero component within the well of the potential. This reveals the quasi-bound states which can be seen in Chapter 7.

Appendix D

Exploration of the Variables in the Equations of motion

There are five different variables that affect how the flow of the electrically charged fluid behaves:

- Initial Charge Density.
- Magnetic field strength. For monopoles this can be altered by changing the distance between the monopole and the plane and also the magnetic charge of the monopole.
- Resistivity.
- Internal Pressure constant
- The width of the sensor plane.

D.1 Effect of Variables on MHD in a Uniform Magnetic Field

Using Figs. D.1a, D.2a, D.3a and D.4a as a baseline to compare what the effects of changing specific variable will do to $\tilde{\rho}$, $\tilde{V}_x$, $\tilde{V}_y$ and MHD Hall voltage.

Decreasing the mass density of the fluid from $\tilde{\rho}_0 = 100$ to $\tilde{\rho}_0 = 80$, Fig. D.1b, we can see that $\tilde{\rho}$ has more oscillations present but the peak magnitude is reduced when compared to Fig. D.1a. The increased oscillations can be seen in the $\tilde{V}_x$ of the electron fluid Fig. D.2b and also in the $\tilde{V}_{HMHD}$ Fig. D.4b , in the case of the x velocity the magnitude is less than Fig. D.2a whereas the peak in the magnetohydrodynamic Hall voltage is greater than the baseline case Fig. D.4a, the classical Hall voltage is also greater. The distribution of $\tilde{V}_y$, Fig. D.3b is the same as Fig. D.3a but the velocity is on average faster than the baseline comparisons.

The next variable we change is the magnetic field strength decreasing β from $1{\times}10^{-3}$ to $1{\times}10^{-4}$. The number of oscillations within mass density (Fig. D.1c), x velocity (Fig. D.2c) and the MHD Hall voltage (Fig. D.4c) compared to baseline case Fig. D.1a, Fig. D.2a and Fig. D.4a respectively. The peak mass density has decreased values as is expected due to the lower magnetic field producing a reduced Lorentz force. This also explains the decrease in x velocity peaks and the Hall voltages. The y velocity, Fig. D.3c, has less range between the minimum and maximum values but the distribution of the velocities is similar to Fig. D.3a.

Decreasing the fluid pressure term α from 10^{-3} to 5×10^{-4} we see that the mass density does not oscillate Fig. D.1d and the difference in the mass density across the plane in the x direction is approximately $\tilde{\rho}_0 \pm 0.05$. $\tilde{V}_x$,

Fig. D.2d, shows a shift to the left of the plane and then dissipates as we move up the y axis. There are no oscillations in the $\tilde{V}_{HMHD}$, Fig. D.4d, after the initial peak in voltage on entering the magnetic field it is quickly damped. The reduced pressure constant reduces the force applied by the internal pressure of the electron fluid, so now the electron fluid does not overshoot the equilibrium point of the forces in the x direction, that occurs when the pressure force is equal to the Lorentz force. The distribution of $\tilde{V}_y$, Fig. D.3d once again looks similar to the baseline case Fig. D.3a but with higher velocity on the left hand side and a lower velocity on the right hand side.

Changing the resistivity from $\gamma = 10^{-3}$ tp $\gamma = 5 \times 10^{-4}$ we see larger oscillations in the y direction of the mass density, Fig. D.1e, when compared with Fig. D.1a the range of mass density is also greater with a decreased resistivity. Both $\tilde{V}_x$, Fig. D.2e, and $\tilde{V}_{HMHD}$, Fig. D.4e, have larger periods of oscillation than compared with Figs. D.2a and D.4a respectively; in both cases the peak values are greater than the baseline comparison case. Interestingly here we see the only example of the distribution of $\tilde{V}_y$, Fig. D.3e, being slightly different with ripples being present along the edge of the velocity patches at either side of the plane.

Finally changing the width of the plane from 1 to 2, there is a slight oscillation in the mass density, Fig. D.1f, on entering the magnetic field but this oscillation dies out quickly when compared to Fig. D.1a; this is also the case when comparing $\tilde{V}_x$, Fig. D.2f, and $\tilde{V}_{HMHD}$, Fig. D.4f to Figs. D.2a and D.4a respectively. We see double the value of Hall voltage both for $\tilde{V}_{HC}$ and $\tilde{V}_{HMHD}$ as the Hall voltage is proportional to the width of the plane which is double that of Fig. D.4a. The reason why the oscillations decrease is that due to the width of the plane there is less build up of electron fluid at the edges

reducing the pressure that forms from the electrostatic repulsion. This in turn leads to less sloshing of the electron fluid. The y velocities, Fig. D.3f, have a greater range of values between the minimum and maximum but the same distribution as Fig. D.3a.

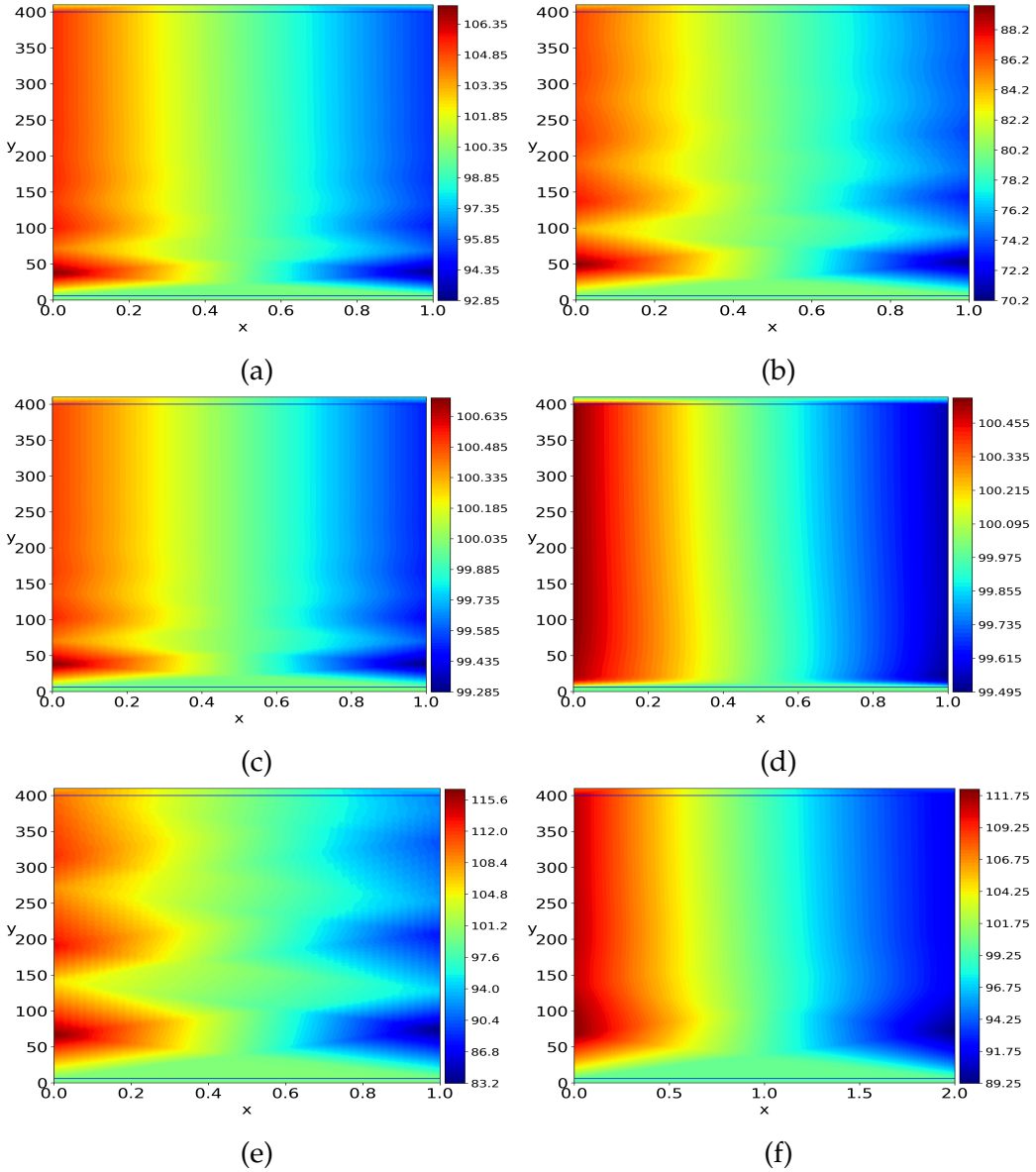

Figure D.1: Mass density plots for with a magnetic field present between $y = 6$ to 400, $\Delta\tilde{x} = 0.01$ and $\Delta\tilde{y} = 0.01$ (a) Initial comparison plot to compare against other plots $\rho_0 = 100$, $\beta = 1 \times 10^{-3}$, $\alpha = 1 \times 10^{-3}$, $\gamma = 1 \times 10^{-3}$. (b) Changing the initial mass density to $\rho_0 = 80$. (c) Changing the magnetic field to $\beta = 1 \times 10^{-4}$. (d) Changing the fluid pressure term to $\tilde{\alpha} = 1 \times 10^{-2}$. (e) Changing the resistivity to $\gamma = 5 \times 10^{-4}$. (f) Changing the plane width to 2.

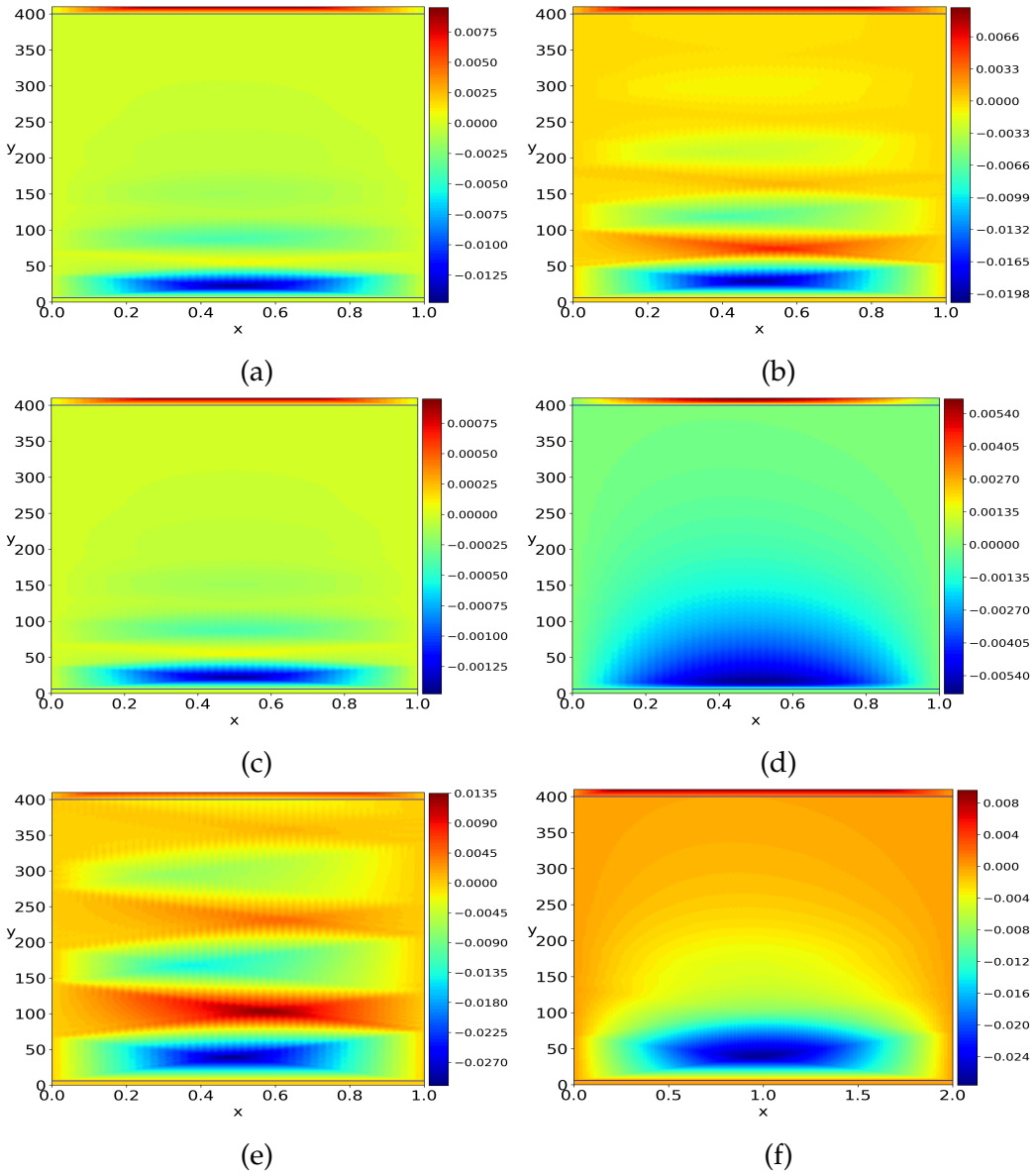

Figure D.2: x velocity plots for with a magnetic field present between y = 6 to 400, $\Delta\tilde{x} = 0.01$ and $\Delta\tilde{y} = 0.01$ (a) Initial comparison plot to compare against other plots $\rho_0 = 100$, $\beta = 1 \times 10^{-3}$, $\alpha = 1 \times 10^{-3}$, $\gamma = 1 \times 10^{-3}$. (b) Changing the initial mass density to $\rho_0 = 80$. (c) Changing the magnetic field to $\beta = 1 \times 10^{-4}$. (d) Changing the fluid pressure term to $\tilde{\alpha} = 1 \times 10^{-2}$. (e) Changing the resistivity to $\gamma = 5 \times 10^{-4}$. (f) Changing the plane width to 2.

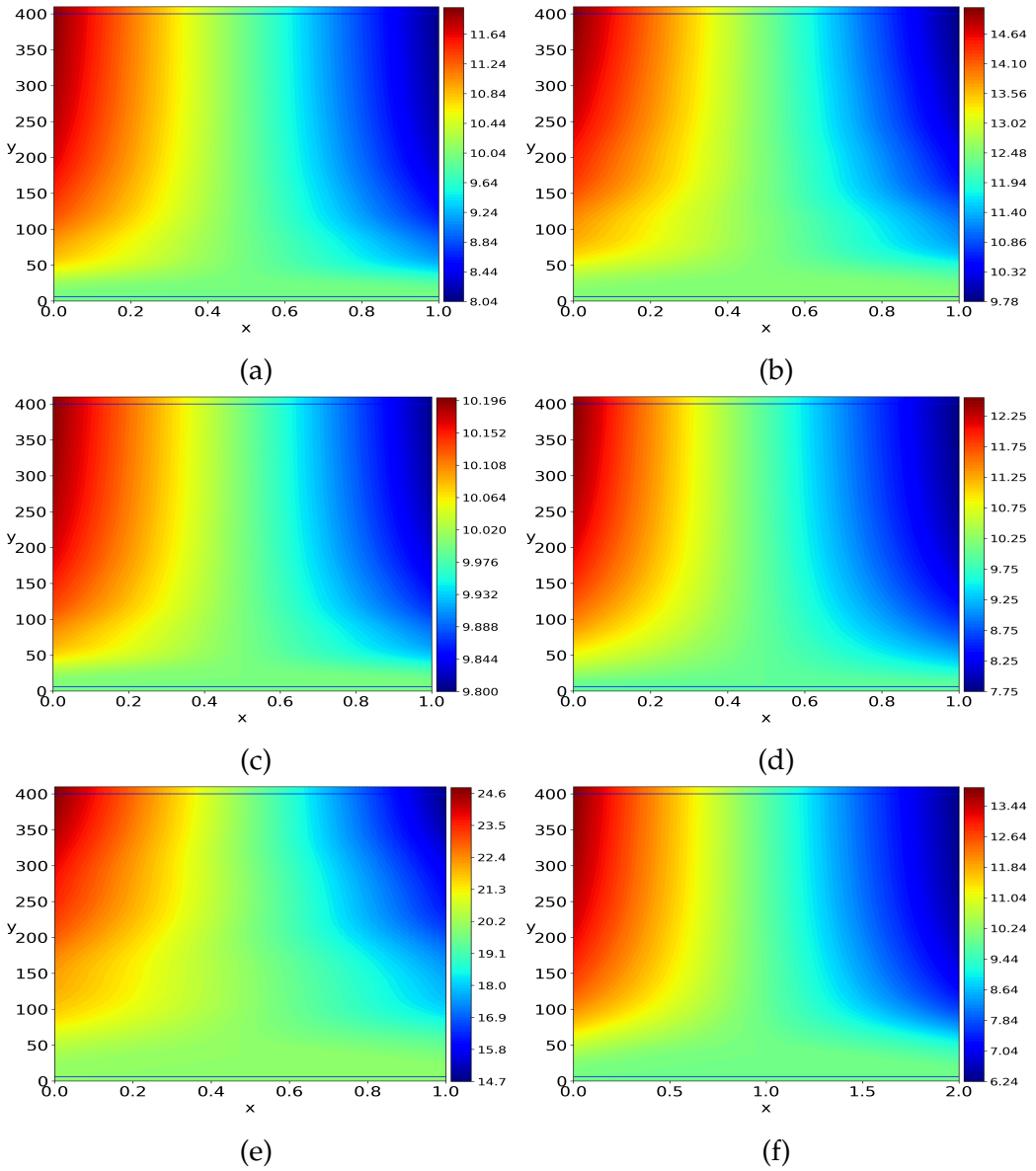

Figure D.3: y velocity plots for with a magnetic field present between $y = 6$ to 400, $\Delta\tilde{x} = 0.01$ and $\Delta\tilde{y} = 0.01$ (a) Initial comparison plot to compare against other plots $\rho_0 = 100$, $\beta = 1 \times 10^{-3}$, $\alpha = 1 \times 10^{-3}$, $\gamma = 1 \times 10^{-3}$. (b) Changing the initial mass density to $\rho_0 = 80$. (c) Changing the magnetic field to $\beta = 1 \times 10^{-4}$. (d) Changing the fluid pressure term to $\tilde{\alpha} = 1 \times 10^{-2}$. (e) Changing the resistivity to $\gamma = 5 \times 10^{-4}$. (f) Changing the plane width to 2.

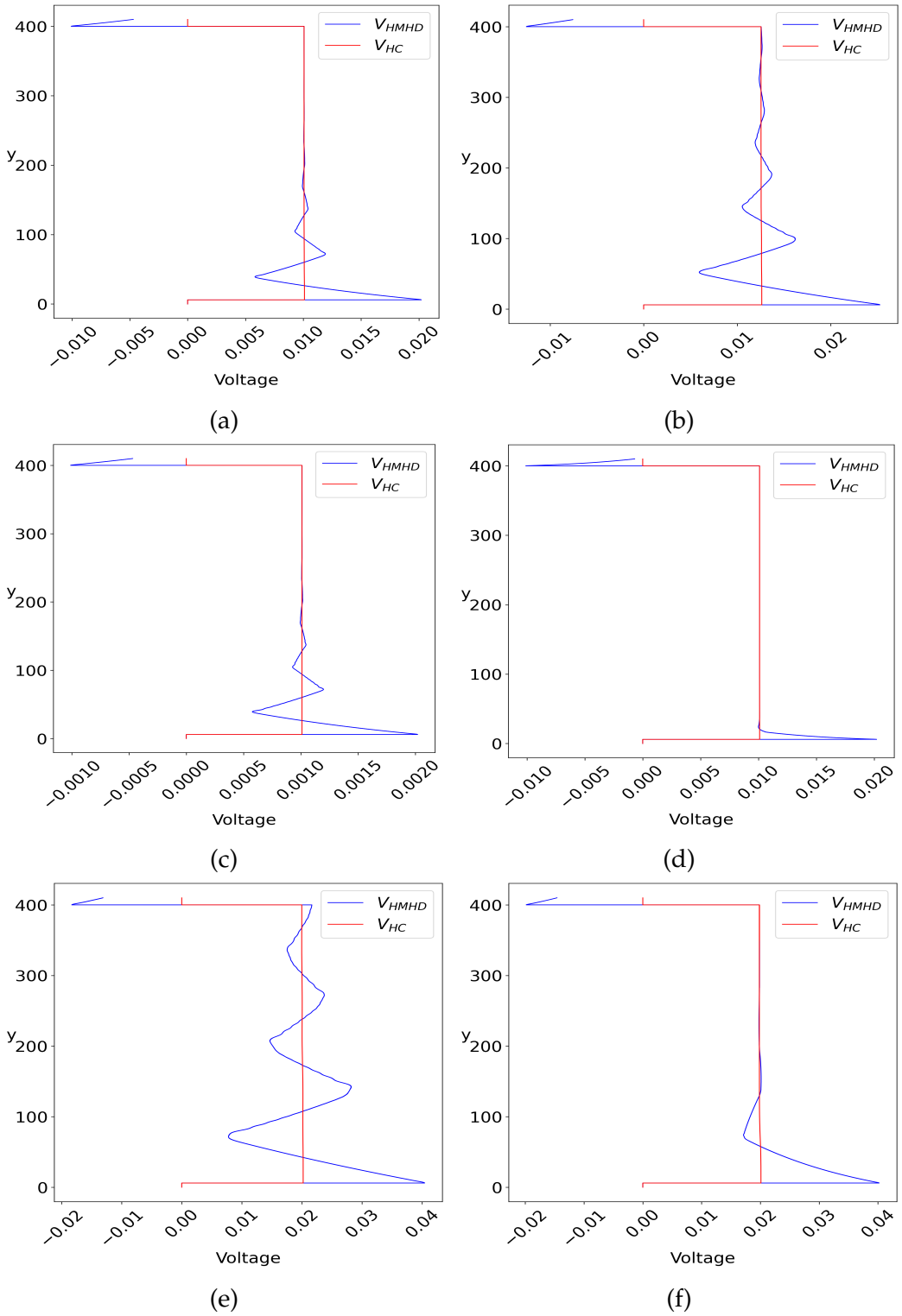

Figure D.4: Hall voltage plots for with a magnetic field present between $y = 6$ to 400, $\Delta\tilde{x} = 0.01$ and $\Delta\tilde{y} = 0.01$ (a) Initial comparison plot to compare against other plots $\rho_0 = 100$, $\beta = 1 \times 10^{-3}$, $\alpha = 1 \times 10^{-3}$, $\gamma = 1 \times 10^{-3}$. (b) Changing the initial mass density to $\rho_0 = 80$. (c) Changing the magnetic field to $\beta = 1 \times 10^{-4}$. (d) Changing the fluid pressure term to $\tilde{\alpha} = 1 \times 10^{-2}$. (e) Changing the resistivity to $\gamma = 5 \times 10^{-4}$. (f) Changing the plane width to 2.

D.2 Effect of Variables on MHD in a Non-Uniform Magnetic Field

In this section we look at the effects of changing the variables has with a single magnetic monopole, using Figs. D.5a, D.6a, D.7a and D.8a as a baseline to compare what the effects of changing specific variable will do to $\tilde{\rho}$, $\tilde{V}_x$, $\tilde{V}_y$ and MHD Hall voltage. In these series of plots we are concentrating on the area nearest the magnetic monopole as this is where any changes will be seen.

On decreasing the initial mass density we consider the distribution of mass, Fig. D.5b. We see two larger jets being formed which bounce of the sides of the plane. The angular separation of the two jets is also decreased compared to Fig. D.5a. The peak x velocity is higher in Fig. D.6b and the distribution is more conical before tapering off, whereas Fig. D.6a has a more rounded distribution when the electron fluid nears the monopole.$\tilde{V}_y$ have the same range of values between Fig. D.7b and Fig. D.7a but decreasing the mass density the velocity is slower to accelerate nearer the sides of the Hall sensor plane. The Hall voltage achieved (both MHD and classical), Fig. D.8b, is a magnitude larger than the baseline case, Fig. D.8a, which is to be expected as Hall voltage is proportional to the Hall coefficient. We see that the sloshing in the MHD Hall voltage occurs at a point further up the plane than for the baseline case.

The next item to look at is increasing the charge of the magnetic monopole. We see that for ρ, $\tilde{V}_x$, and $\tilde{V}_y$ (Figs. D.5c, D.6c and D.7c) the relative distribution of mass density, $\tilde{V}_x$ and $\tilde{V}_y$ is the same across the plane but are increased by an order of two over the baseline case Figs. D.5a, D.6a and D.7a respectively. The peaks in both types of Hall voltage, Fig. D.8c, occur at the same

position as Fig. D.8a but their value is two orders of magnitude larger; the sloshing effect happens at the same point in both examples. The Hall voltage is proportional to the magnetic field so an increase of two orders of magnitude of monopole charge increase the Hall voltage proportionally.

Decreasing α, Fig. D.5d, to 10^{-3} we see two larger jets of mass density form with a smaller angle of separation between them than Fig. D.5a with a higher difference in peak magnitude between them. As with the lower mass density we see a conical like distribution of $\tilde{V}_x$, Fig. D.6d, the range of values of velocity in the x direction is the same as for the decreased mass density case Fig. D.6b. The y velocities, Fig. D.7d, are more narrow than the baseline case, Fig. D.7a, and take much more of the length of the Hall sensor to start interacting with the edges. Comparing Fig. D.8d against the base line case, Fig. D.8a we see that the peak in the voltage occurs at the same place and that the magnitude of this peak is the same, the difference is in the sloshing after the monopole where the reduced pressure term has decreased its magnitude.

Reducing the resistivity term, γ, to 5×10^{-4} Fig. D.5e we see two jets of mass density that taper off slowly opposed to Fig. D.5a the range of difference in the values of mass density is greater. Fig. D.6e shows a higher peak velocity near the monopole compared to Fig. D.6a.$\tilde{V}_y$, Fig. D.7e, reaches its peak velocity closer to the monopole than the baseline case, Fig. D.7a. The Hall voltage peak, Fig. D.8e is double that of the baseline case, Fig. D.8a.

Increasing the width of the Hall sensor from 1 to 2 we see that the mass density, Fig. D.5f, has two smaller jets that have less interaction with the side of the Hall sensor compared with Fig. D.5a, the range of magnitude of mass density remains the same. The x velocity tapers of sooner in the baseline case, Fig. D.6a, compared to the case with a wider Hall sensor Fig. D.6f. $\tilde{V}_y$,

Fig. D.7f, has less interaction with the edge of the plane and the highest and lowest velocities are concentrated towards the centre of the plane. The peak value of the Hall voltages is the same between the increased width case, Fig. D.8f, and the base line case, Fig. D.8a. The sloshing in the Hall voltage is greatly reduced with the increased width reducing the number density of charge particles in any given region reducing the force from the pressure term pushing the electron fluid in the opposite x direction.

The distance from the plane to the monopole is an extra variable that can be altered in the monopole case, increasing the distance form 0.1 to 1, the mass distribution, Fig. D.5g looks more like that seen in a uniform magnetic field, where the mass is decreased on one side and increased on the other. The x velocity, Fig. D.6g, is spread broadly across the plane tapering off as we travel up it. The change from the initial y velocity, Fig. D.7g, is concentrated towards the edges of the Hall sensor. The Hall voltage, Fig. D.8g, produces a peak in the same place as Fig. D.8a but the magnitude of the peaks in the Hall voltages is approximately an order below the baseline case. The Hall voltage is much more broadly spread now with voltage being produced earlier and sustaining further up the plane.

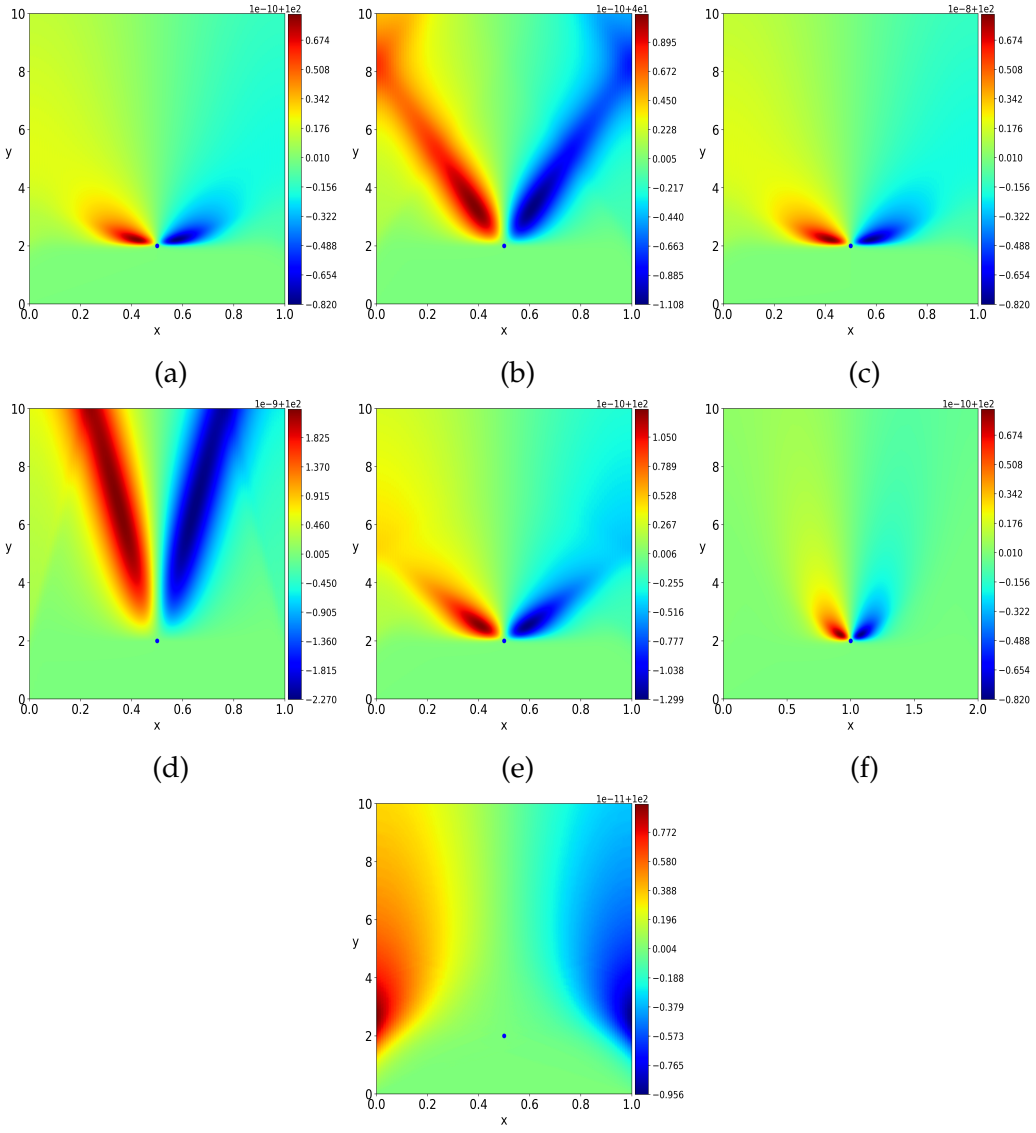

Figure D.5: Mass density plots for with a magnetic monopole (a) Initial comparison plot to compare against other plots $\tilde{\rho}_0 = 100$, $\tilde{Q}_m = 1 \times 10^{-12}$, $\alpha = 1 \times 10^{-1}$, $\gamma = 1 \times 10^{-3}$, distance of monopole to plane = 1×10^{-1}. (b) Changing the initial mass density to $\tilde{\rho}_0 = 40$. (c) Changing the monopole charge to $\tilde{Q}_m = 1{\times}10^{-10}$. (d) Changing the fluid pressure term to $\alpha = 1{\times}10^{-3}$. (e) Changing the resistivity to $\gamma = 5 \times 10^{-4}$. (f) Changing the dimensionless plane width to 2. (h) Changing the dimensionless monopole distance to the plane to 1.

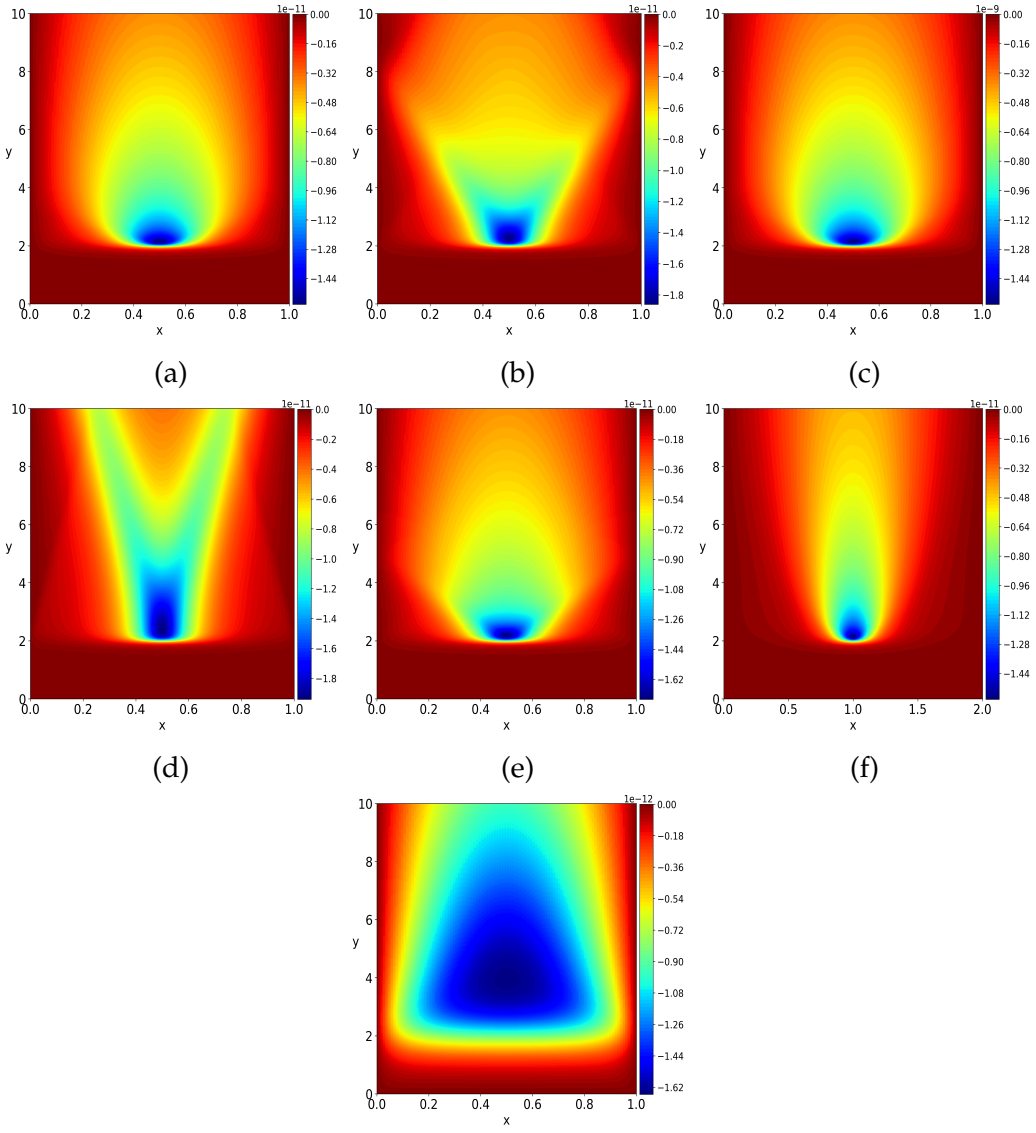

Figure D.6: x velocity plots for with a magnetic monopole (a) Initial comparison plot to compare against other plots $\tilde{\rho}_0 = 100$, $\tilde{Q}_m = 1 \times 10^{-12}$, $\alpha = 1 \times 10^{-1}$, $\gamma = 1 \times 10^{-3}$, distance of monopole to plane = 1×10^{-1}. (b) Changing the initial mass density to $\tilde{\rho}_0 = 40$. (c) Changing the monopole charge to $\tilde{Q}_m = 1{\times}10^{-10}$. (d) Changing the fluid pressure term to $\alpha = 1{\times}10^{-3}$. (e) Changing the resistivity to $\gamma = 5 \times 10^{-4}$. (f) Changing the dimensionless plane width to 2. (h) Changing the dimensionless monopole distance to the plane to 1.

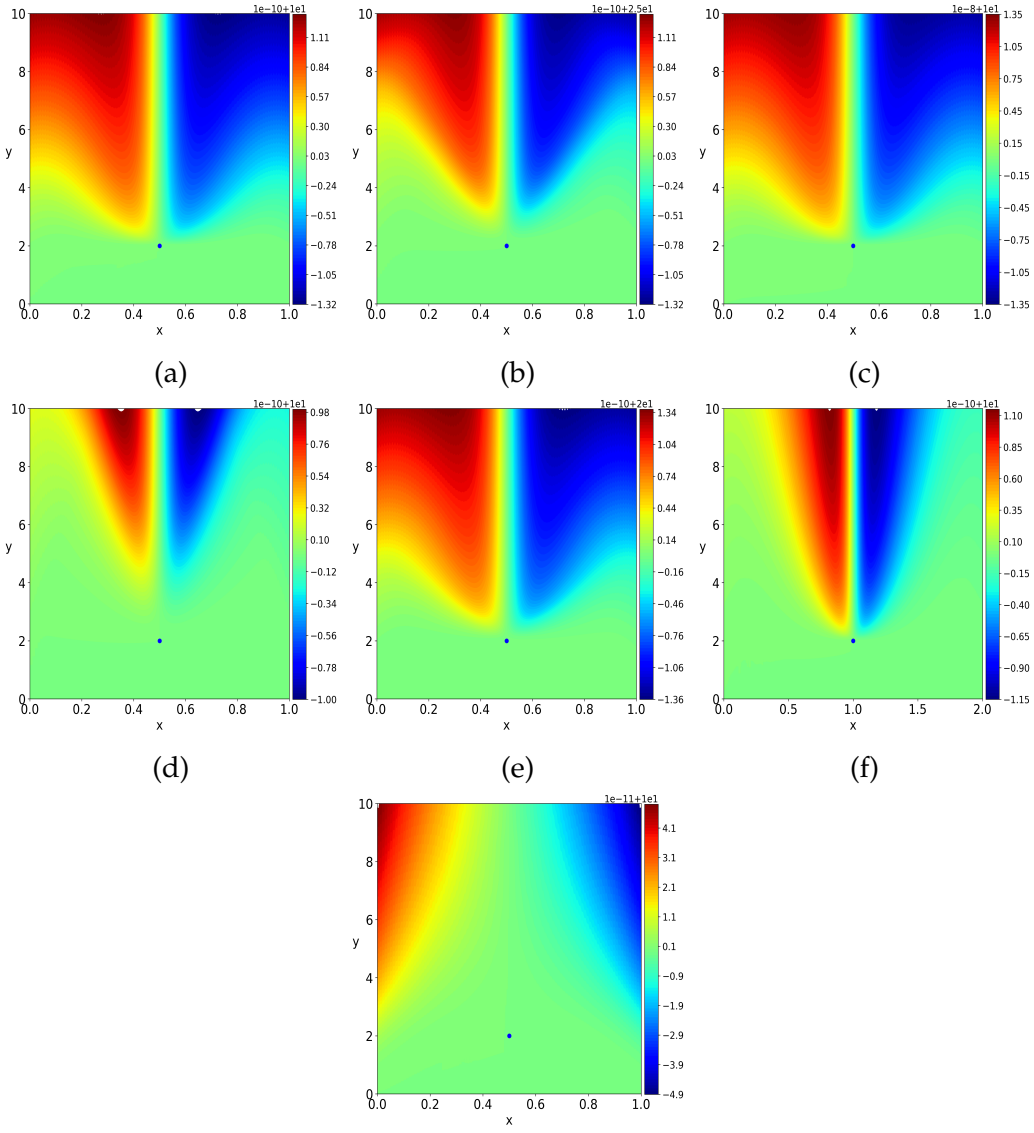

Figure D.7: y velocity plots for with a magnetic monopole (a) Initial comparison plot to compare against other plots $\tilde{\rho}_0 = 100$, $\tilde{Q}_m = 1 \times 10^{-12}$, $\alpha = 1 \times 10^{-1}$, $\gamma = 1 \times 10^{-3}$, distance of monopole to plane = 1×10^{-1}. (b) Changing the initial mass density to $\tilde{\rho}_0 = 40$. (c) Changing the monopole charge to $\tilde{Q}_m = 1{\times}10^{-10}$. (d) Changing the fluid pressure term to $\alpha = 1{\times}10^{-3}$. (e) Changing the resistivity to $\gamma = 5 \times 10^{-4}$. (f) Changing the dimensionless plane width to 2. (h) Changing the dimensionless monopole distance to the plane to 1.

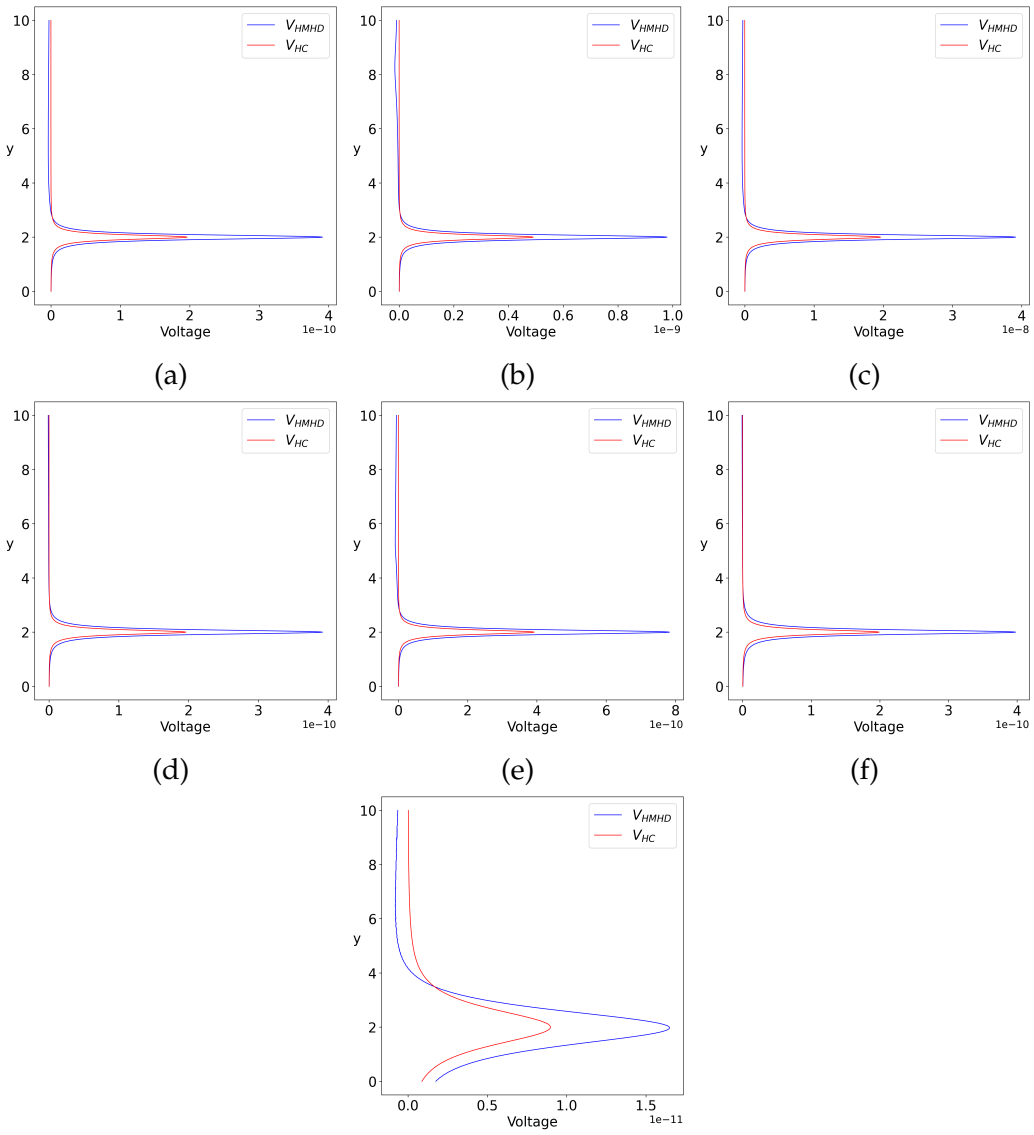

Figure D.8: Hall voltage plots for with a magnetic monopole (a) Initial comparison plot to compare against other plots $\tilde{\rho}_0 = 100$, $\tilde{Q}_m = 1 \times 10^{-12}$, $\alpha = 1 \times 10^{-1}$, $\gamma = 1 \times 10^{-3}$, distance of monopole to plane = 1×10^{-1}. (b) Changing the initial mass density to $\tilde{\rho}_0 = 40$. (c) Changing the monopole charge to $\tilde{Q}_m = 1{\times}10^{-10}$. (d) Changing the fluid pressure term to $\alpha = 1{\times}10^{-3}$. (e) Changing the resistivity to $\gamma = 5 \times 10^{-4}$. (f) Changing the dimensionless plane width to 2. (h) Changing the dimensionless monopole distance to the plane to 1.